NUMERICAL MODELING OF PLASMA CUTTING TORCHES

A THESIS
SUBMITTED TO THE FACULTY OF THE GRADUATE SCHOOL
OF THE UNIVERSITY OF MINNESOTA
BY

Madhura Shashikumar Mahajan

IN PARTIAL FULFILLMENT OF THE REQUIREMENTS
FOR THE DEGREE OF
MASTER OF SCIENCE IN MECHANICAL ENGINEERING

Adviser: Dr. Joachim V R Heberlein

January 2010

ACKNOWLEDGEMENTS

My sincere thanks go to Dr. Joachim V R Heberlein for his valuable supervision, advice and guidance throughout the project. I am most grateful of Dr. Srikumar Ghorui, Dr. He Ping Li and Dr. Juan Pablo Trelles for laying the foundation of this work for me. I would like to thank Dr. Jon Lindsay, Dr. John Peters, Mr. Steve Liebold and Mr. Aaron Brandt from Hypertherm Inc., the generous sponsor of the project, for their help in this research through meaningful conversations.

I am indebted to all of my teachers at the University of Minnesota for their thoughtful guidance throughout my coursework. I gratefully acknowledge my thesis defense committee members Dr. John Bischof and Dr. Mahesh Krishnan for their helpful supervision. I thank my colleagues from the HTPL group, University of Minnesota for making the research work enjoyable. I would also like to acknowledge the help of all my dear friends, especially Soumya for his persistent confidence in me.

Finally, I would like to express my gratitude towards my family for their unflinching encouragement and support in various ways.

DEDICATION

This thesis is dedicated to my beloved grandparents.

ABSTRACT

In this thesis, a study of numerical modeling technique is performed for various plasma cutting torches. The plasma cutting process model uses a finite volume method based on the SIMPLEC algorithm along with the solver "FAST-2D (Flow Analysis Simulation Tool-2D)." The source code available is a general code and does not include any finite volume grid generator. Part of this work includes development of a generalized finite volume grid generator dedicated for the new generation plasma torches. This modified version of the grid generator offers users a great flexibility in grid and geometry choice, and offers the advantage of easy variations in boundary conditions. The work presented also includes a detailed study of the effect of the radiation model and the cathode current density boundary condition on the distribution of the plasma field quantities. Finally the modified version of the grid generator along with the appropriate radiation model and current density boundary condition at the cathode are employed to simulate selected plasma cutting torches from Hypertherm Inc.

TABLE OF CONTENTS

LIST OF TABLES

LIST OF FIGURES

1. INTRODUCTION

Electrical arcs and, more generally thermal plasma torches, owing to their ability to cut a broad range of metals with very high productivity, are widely used in industry. The plasma-arc-cutting process is characterized by a transferred electric arc that is established between an electrode (the cathode) that is part of the cutting torch another electrode that is the metallic work-piece and (the anode) to be cut.

In order to obtain a high-quality cut and a high productivity, the plasma jet must be, among other things, as collimated as possible and must have high power density. With this regard, modeling and numerical simulation may be very useful tools for the investigation of the characteristics of the plasma discharge generated in these kinds of devices, as well as for the optimization of industrial cutting torches.

Initial work in this field was done by Hsu *et al* with two-temperature modeling of free burning arcs with proper boundary conditions (Hsu & Pfender, 1983). For an oxygen arc, Freton *et al* used a 2-D turbulence model using the commercial code FLUENT and performed associated spectroscopic studies for plasma characteristics (Freton, Gonzalez, Gleizes, Peyret, Caillibotte, & Delzenne, 2002). It was also shown how experimental and theoretical approaches are complimentary to each other for full characterization of a plasma torch (Freton, Gonzalez, Peyret, & Gleizes, 2006). A full 3-D model of an argon inductively coupled plasma torch has been applied to commercial torch geometry (Colombo, Ghedini, & Mostaghimi, 2008). Recently an equilibrium model was developed by Colombo *et al* to investigate the behavior of various transferred arc plasma cutting torches (Colombo, Concetti, Ghedini, Dallavalle, & Vancini, 2008).

The numerical modeling of physical systems helps the designer make the design process efficient by allowing an earlier optimization analysis (i.e. through parametric design), and saving experimentation time. The mathematical/numerical modeling becomes especially important in thermal plasma torch design due to the inherent difficulty in accessing the inside torch regions for evaluation of parameters like temperature, pressure or flow patterns. As this region is inaccessible to most diagnostics, simulations are one of the few means to find out the relative importance of the underlying physical phenomena and their effects.

This thesis presents a study of two-temperature, axi-symmetric and non-equilibrium model developed for Hypertherm plasma cutting torches (Ghorui, Heberlein, & Pfender, 2007). The non-equilibrium properties required for fluid dynamic simulations are obtained from a non-equilibrium property code that takes chemical non-equilibrium into account (Ghorui, Heberlein, & Pfender, 2007). The thesis includes development of a generalized finite volume grid generator for Hypertherm plasma torches, and analysis of the radiation and cathode current density effects on the torch performance.

This thesis has three main parts: (1) Study of the existing plasma torch model along with the generalization of the grid generator, (2) analysis of the effects of the radiation model and (3) the cathode current density on the distribution of plasma field quantities and application of this model to the Hypertherm plasma cutting torches.

The thesis is organized as follows:

In chapter two, the basics of the plasma cutting process and its mathematical modeling are described; particular emphasis is given on the base approach of this modeling work which consists of a finite volume method. This SIMPLEC algorithm based solver FAST-2D (Flow Analysis Simulation Tool- 2D) developed by Zhu is described in detail along with the underlying governing equations (Zhu, 1991). Emphasis is given to the non-equilibrium nature of the modeling which is different from the most commonly used thermal equilibrium approximation for the modeling of plasma. This chapter describes an approach to obtain the non-equilibrium thermodynamic and transport properties of oxygen-nitrogen plasma which is an essential to the non-equilibrium simulation of a plasma cutting torch. This chapter ends with a brief description of the solution procedure employed in the code.

Chapter three is devoted to the development of a finite volume grid generation subroutine. It comprises of identification of the torch geometry control points, mapping of radial and axial solid and fluid zones, and development of the boundaries separating the aforementioned zones. The chapter then describes the geometric limitations of the old grid generator along with the development of the modified grid generator. This new grid generator becomes especially useful for simulation of recent plasma torch designs due to its flexibility and robustness.

Chapter four is the description of the radiation model used in the plasma torch simulation. It describes the energy transport in the thermal plasmas along with the concept of the “net volumetric radiation loss” and “effective radius of radiation”. This

chapter concludes with the preliminary results for the radiation model of a sample torch studied.

Chapter five presents a discussion of the cathode current density boundary condition used in the simulation. Its importance was realized while researching the effects of the cathode conditions imposed in the simulation on the overall distribution of plasma field quantities. This chapter presents the results of simulations with different cathode current density profiles used as boundary condition at the cathode.

The thesis ends with the presentation of various results of the simulations of plasma torches with the working currents of 200A, 300A and 400A along with their interpretation, analysis and concluding remarks.

Regardless of the inherent complexity of the phenomena under study, the material presented is expected to be application-oriented, and to offer adequate and detailed analyses of a wide range of possible scenarios in plasma torch modeling.

1.1 Objective

The objective of this thesis is to study a previously developed numerical technique for the modeling of the plasma flow inside a plasma cutting torch system, with emphasis on its application to newer generation plasma cutting torches by enhancing the flexibility of the previously developed model through development of more adaptive grid generator, along with the study of the effects of the variation in the radiation model and the cathode current density boundary condition on the simulation.

2. MODELING OF PLASMA CUTTING PROCESS

2.1 The plasma cutting process

The plasma cutting process utilizes electrically conductive plasma gas to transfer energy from an electrical power source through a plasma cutting torch to the material being cut. The basic plasma arc cutting system consists of a power supply, an arc starting circuit and a torch. These system components provide the electrical energy, ionization capability and process control that is necessary to produce high quality, highly productive cuts on a variety of conductive materials.

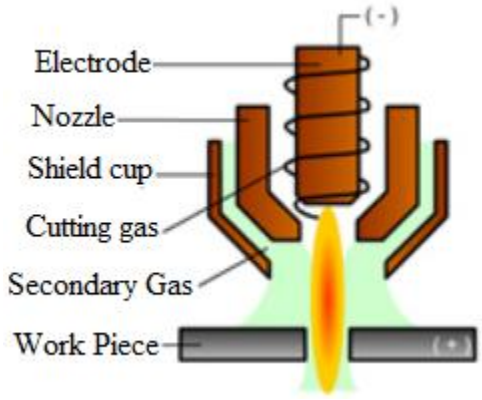

Figure 2.1: A typical plasma torch (www.hypertherm.com, 2009)

The power supply is a constant current DC power source. The open circuit voltage is typically in the range of 240 to 400V DC. The output current (amperage) of the power supply determines the speed and cut thickness capability of the system. The main function of the power supply is to provide the energy required to maintain the plasma arc after ionization.

The arc starting circuit is a high frequency generator circuit that produces an AC voltage of 5,000 to 10,000 V at approximately 2 MHz. This voltage is used to create a high intensity arc inside the torch to ionize the gas, thereby producing the plasma.

The torch serves as the holder for the consumable nozzle and electrode, and provides cooling (either gas or water) to these parts. The nozzle and the electrode constrict and maintain the plasma jet. Plasma torches could be classified based on the direction of the plasma working gas. Along with the azimuthal (swirl) component, the plasma working gas has either an axial or a radial component to the total velocity and the torch may be classified as axial or radial injection torch based on this component. Another classification would be vented and non-vented torches. A vent in the plasma torch could be described as a bypass channel, formed between the inner and outer nozzle pieces, that directs the bypass flow to atmosphere (Couch Jr., Sanders, Luo, Sobr, & Backander, 1994). The final result obtained by means of a vented torch is that the gas flow in the plasma chamber is highly uniform and very steady as compared to a non-vented torch (Colombo, Concetti, Ghedini, Dallavalle, & Vancini, 2008).

2.2 Modeling approach

Due to the inherent complexity of the plasma cutting process, which involves diverse multi-physics and multi-scale phenomena (viz. plasma flow physics, plasma-surface interactions, phase change processes, interfacial phenomena, material removal and transport, etc.), a de-coupling based on the characteristic time scales of each aspect of the complete cutting process is proposed. The first de-coupling separates the plasma arc

generation process from the material melting and removal process. Plasma generation is the subject of this work and is described in detail beginning in section 2.3.

The material melting and removal portion of the cutting process is briefly described in the rest of this section. One possible approach to modeling this portion of the process would be a further de-coupling based on characteristic time scales. Initially the de-coupling could be based on the characteristics time scales for: torch movement, material melting, and material removal (namely τ_1, τ_2, and τ_3, respectively). Modeling approach usually relies on: $\tau_1 >> \tau_2 >> \tau_3$; i.e. the movement of the torch is significantly slower than the rate at which material is being melted, which is significantly slower than the rate at which the molten material is being removed from the cutting front. Thus a complete model would have three phases as follows.

2.2.1 Torch movement

Considering that the torch moves with a cutting speed V_c, a natural time scale τ_1 of this aspect of the cutting process is:

$$\tau_1 = \frac{\delta_1}{V_c} \tag{2.1}$$

where τ_1 is a characteristic cutting distance, typically of the order of the thickness of the work-piece L_p (i.e. τ_1 is of the order of 1 cm); therefore τ_1 is directly proportional to the thickness of the work-piece.

This part of the analysis would model the advancement of the torch and the interaction of the plasma flow with the surface of the work-piece. The analysis of this phase would provide the heat fluxes q_n and the stresses τ_{tn} (the sub-index n indicates

normal, and t tangent to the cutting front) over the cutting front to be used in the next two aspects of the model; particularly q_n drives the material melting, whereas τ_{tn} the material removal. The other aspects of the modeling would provide the shape and properties of the cutting front. The characteristics of the cutting front can then be used as inputs to the plasma flow model to study, i.e. the movement of the arc root through the cut.

2.2.2 Material melting

Stefan's theory of phase change processes (particularly melting-solidification) gives us an estimate of the time τ_2 required to advance the molten front by a thickness τ_2 due to the imposition of a constant heat flux q_n:

$$\tau_2 = \lambda_S \delta_2 \tag{2.2}$$

where the constant λ_S is an implicit function of q_n, the diffusivities of the liquid and solid phases, the melting temperature and the latent heat of fusion of the material. That is $\lambda_S \approx \lambda_S(\frac{H_m}{q_n}, \frac{\alpha_s}{\alpha_l}, \frac{\kappa_s}{\kappa_l})$, with H_m as the volumetric latent heat of fusion, α_s and α_l as the solid- and liquid-phase thermal diffusivities respectively, and κ_s and κ_l thermal conductivities).

The numerical modeling of the phase change processes of the work-piece would be based on the enthalpy method based on either a finite-volume or a finite-element formulation. The current thickness of the molten front and the temperature distribution through it would be inputs to the next modeling phase.

2.2.3 Material removal

Performing a momentum balance over a thin layer of molten material subject to a surface stress τ_{tn}, and neglecting the surface tension and friction within the molten material, a characteristic time for material removal τ_3 is:

$$\tau_3 = (\rho_l/\tau_{tn})^{\frac{1}{2}}\,\delta_3 \tag{2.3}$$

where ρ_l is the density of the molten material, and δ_3 is the thickness of the layer, i.e. δ_3 is of the order of 1 μm (therefore, $\delta_3 \ll \delta_2$). From the above expression, it can be deduced that the stronger the plasma jet (and therefore the larger the τ_{tn}), the faster the material is removed.

The modeling of this phase of the cutting process would be based on the volume-of-fluid (VOF) approach, a technique that allows the tracking of moving boundaries in fluid flow problems.

2.3 Plasma generation model

Thermal plasma gas discharges (electric arcs) are characterized by three different discharge regions: the two electrode sheaths and the arc column (see Figure 2.2). A simple way to describe the arc column is to assume local thermodynamic equilibrium (LTE); this allows description of all thermodynamic and transport properties of the fluid as functions of temperature, pressure and the molar fractions of the gases. In reality, the partially ionized gas will deviate from the LTE state significantly especially near the electrodes and fringes of the arc column. Under such a condition called the Non-LTE, the electron temperature will be much higher than the heavy-particle temperature. The physics of the arc column is described by a magneto-hydrodynamic (MHD) model.

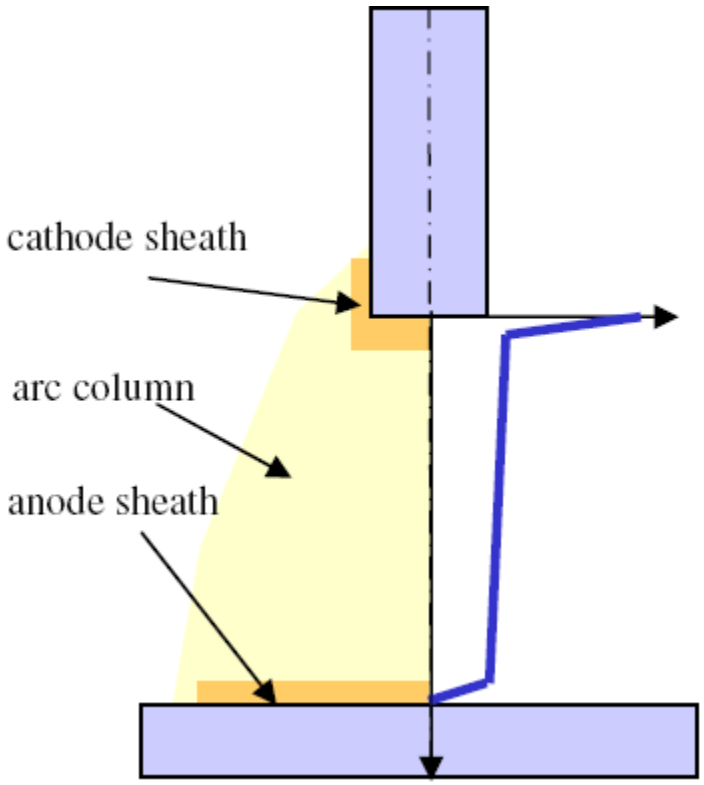

Figure 2.2: A thermal plasma discharge (Schnick, Füssel, & Zschetzsche, 2006)

The idea of MHD is that magnetic fields can induce currents in a moving conductive fluid, which create forces on the fluid, and also change the magnetic field itself. The set of equations which describe MHD are a combination of the Navier-Stokes equations of fluid dynamics and Maxwell's equations of electromagnetism (see Figure 2.3). The electromagnetic equations are solved for fluids as well as solids. In the present work, the sheath layers were not modeled.

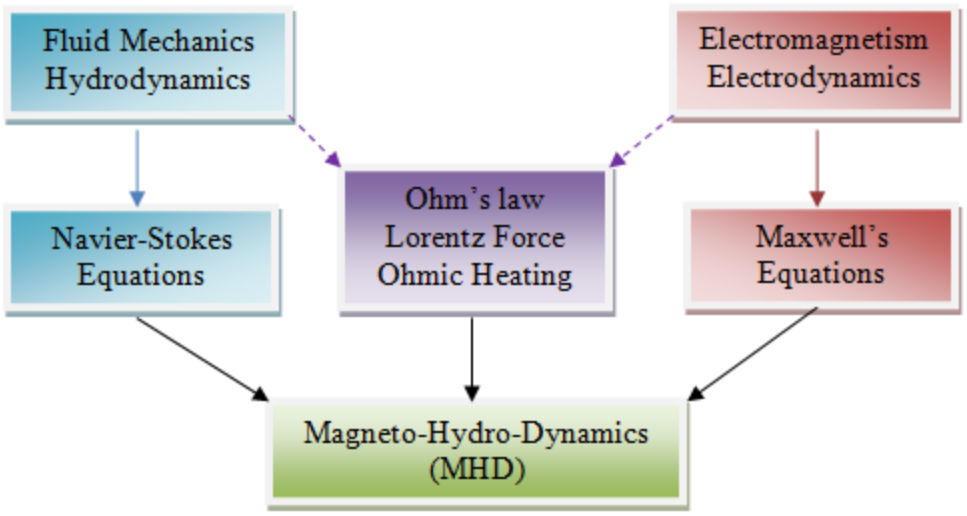

Figure 2.3 Basics of MHD (Schnick, Füssel, & Zschetzsche, 2006)

As shown in Figure 2.4, the plasma jet expands and mixes with the shield gas at the downstream of the nozzle exit and becomes supersonic. In actual cases, the flow of the high temperature, partially ionized gas inside/outside of the nozzle is compressible and deviates from local thermodynamic equilibrium (LTE) state.

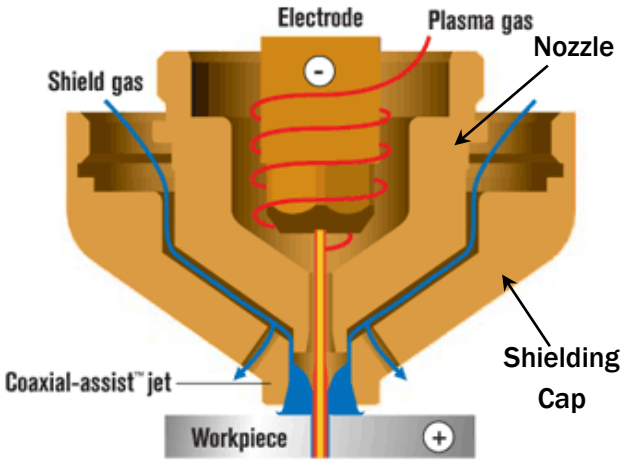

Figure 2.4: Schematic diagram for HT 2000 oxygen plasma cutting torch (www.hypertherm.com, 2009)

A 2D Non LTE simulation of the heat transfer and flow patterns inside the nozzle was carried out with a non-commercial computer code which could predict the compressible effects of the thermal plasmas. The shield was not part of this simulation.

A non-uniform, body-fitted mesh was used for the 2-D modeling. A suitable version of a non-commercial computer code FAST-2D (Flow Analysis Simulation Tool of Two Dimensions) was employed to solve the set of partial differential equations with the appropriate boundaries.

2.4 Governing equations

The governing equations along with the underlying assumptions are presented in this section. As mentioned earlier a non-commercial computer code FAST-2D (Flow Analysis Simulation Tool of Two Dimensions) by (Zhu, 1991) is used to solve this set of governing equations for plasma modeling.

2.4.1 Basic assumptions

a. The plasma working gas used is either pure oxygen or a combination of oxygen and nitrogen in the ratios 50:50, 20:80 or 80:20.
b. The plasma is in kinetic and chemical non-equilibrium state and separate Maxwellian distributions of electrons and heavy particles exist.
c. Charge neutrality is sustained in the system provided that the plasma sheath near the cold wall is ignored.
d. The viscous dissipation and pressure work terms in the energy equation are neglected.

2.4.2 Continuity equation for species 's'

$$\frac{\partial n_s}{\partial t} + \nabla.(n_s\bar{v}) = -\nabla.\bar{\psi}_s + \dot{n}_s \tag{2.4}$$

where $\bar{v}$ is the mass-averaged velocity of the gas, $n_s$and $\bar{\psi}_s$ are the number density and number flux of species s, respectively, with the relationship (Li & Chen, 2001)

$$\bar{\psi}_s = n_s\bar{V}_s \tag{2.5}$$

and

$$\bar{V}_s = \frac{n}{\rho p_s}\sum_j \frac{T_s}{T_j} m_j(D^a_{sj}\nabla p_j - en_jZ_jD_{sj}\bar{E}^e) \tag{2.6}$$

where p_s, T_s, m_s and Z_s are the partial pressure, temperature, mass and electric charge number of species s, respectively. $\bar{E}^e$ is the externally applied electric field. D_{sj} and D^a_{sj} are the ordinary and ambipolar diffusion coefficients for a multi-component gas, respectively, with the following relationship (Li & Chen, 2001)

$$D^a_{sj} = D_{sj} + \frac{\alpha_s}{\beta}\sum_k Z_kD_{kj} \tag{2.7}$$

where

$$\alpha_s = \sum_k m_kn_kZ_kD_{sk}/T_k \ \ and\ \beta = -\sum_j\sum_k Z_jZ_km_kn_kD_{jk}/T_k \tag{2.8}$$

$\dot{n}_s$ is the net production term of species s. For instance, consider O_2, O^{++} and e as the independent species undergoing following reactions.

$$O_2 \leftrightarrow 2O \tag{a}$$

$$O \leftrightarrow O^+ + e \tag{b}$$

$$O^+ \leftrightarrow O^{++} + e \tag{c}$$

The corresponding expressions for $\dot{n}_s$ can be expressed as follows (Vincenti & Kruger, 1965)

$$\dot{n}_{o_2} = k_{b1} n_{o_2} [\frac{n_o^2}{n_{o_2}} - \left(\frac{n_o^2}{n_{o_2}}\right)^*] \tag{2.9}$$

$$\dot{n}_{o^{++}} = k_{b3} n_{o^+} [\left(\frac{n_{o^{++}} n_e}{n_{o^+}}\right)^* - \left(\frac{n_{o^{++}} n_e}{n_{o^+}}\right)] \tag{2.10}$$

$$\dot{n}_e = k_{b2} n_0 \left[\left(\frac{n_{o^+} n_e}{n_o}\right)^* - \frac{n_{o^+} n_e}{n_o}\right] + k_{b3} n_{o^+} \left[\left(\frac{n_{o^{++}} n_e}{n_{o^+}}\right)^* - \frac{n_{o^{++}} n_e}{n_{o^+}}\right] = \dot{n}_e^{(b)} + \dot{n}_e^{(c)} \tag{2.11}$$

where k_{br} is the coefficient appropriate to the backward reaction r (reactions (a)-(c)). The superscript "*" indicates the values of number densities at chemical equilibrium state. $\dot{n}_e^{(b)}$ and $\dot{n}_e^{(c)}$ represent the production rates of electrons in reaction (b) and (c), respectively.

Then, the number densities of O and O^+ can be calculated with the auxiliary relationship

$$p = \sum_j p_j = p_e + p_{O_2} + p_O + p_{O^+} + p_{O^{++}}$$

$$= n_e k_B T_e + (n_{O_2} + n_O + n_{O^+} + n_{O^{++}}) k_B T_h$$

$$n_e = n_{o^+} + 2 n_{o^{++}} \tag{2.12}$$

2.4.3 Momentum equation

$$\frac{\partial(\rho \bar{v})}{\partial t} + \nabla.(\rho \bar{v} \bar{v}) = -\nabla p + \nabla.\overleftrightarrow{\tau} + \vec{j} \times \vec{B} \tag{2.13}$$

where ρ, p and $\overleftrightarrow{\tau}$ are the mass density, scalar pressure and viscous stress of the gas, respectively. $\vec{j}$ and $\vec{B}$ are the current density and the self-induced magnetic field, respectively.

2.4.4 Electron energy equation

$$\frac{\partial(\rho_e h_e)}{\partial t} + \nabla.(\rho_e h_e \vec{v}) = \nabla.(k_e \nabla T_e) + \vec{j}.\vec{E}' - \nabla.\left(\rho_e h_e \vec{V_e}\right) + \dot{Q}_{eh}^{el} - \dot{S}_R \tag{2.14}$$

where ρ_e, h_e, k_e and T_e are the mass density, specific enthalpy, thermal conductivity and temperature of electrons, respectively. $\overrightarrow{E}$ is the total electric field. $\dot{S}_R$ is the net radiation power per unit volume. $\dot{Q}_{eh}^{el}$ is the rate of total energy change of electrons resulting from elastic collisions with all heavy particles, which can be expressed as

$$\dot{Q}_{eh}^{el} \approx \sum_{j=h} -(3m_e n_e \bar{\nu}_{ej}/m_j)\, k_B(T_e - T_h) \tag{2.15}$$

where $\bar{\nu}_{ej}$ is the average collision frequency between electrons and heavy particles, which can be expressed as (Mitchner & Kruger, 1992).

$$\bar{\nu}_{ej} = n_j \bar{g}_{ej} \bar{Q}_{ej} \tag{2.16}$$

where $\bar{Q}_{ej}$ is the average momentum transfer cross section, $\bar{g}_{ej}$ is the mean relative speed for particles with Maxwellian velocity distributions, which can be calculated by (Mitchner & Kruger, 1992)

$$\bar{g}_{ej} = \sqrt{\frac{8k_B T_e}{\pi m_e}} \tag{2.17}$$

In this approach, the average thermal energy change term is included in the gas heating (enthalpy) term. Another approach could be to include, the average thermal energy change accompanied by the electron production, $\dot{Q}_{ch}$, in equation (2.14). This term is expressed as:

$$\dot{Q}_{ch} = -\left[\dot{n}_e^{(b)}(E_{O^+} - E_O) + \dot{n}_e^{(c)}(E_{O^{++}} - E_{O^+})\right] \quad (2.18)$$

where $(E_{O^+} - E_O)$ and $(E_{O^{++}} - E_{O^+})$ represent the ionization energies (including the lowering of the ionization energies because of the interactions between the charged particles) for O and O^+, respectively.

2.4.5 Heavy-particle energy equation

$$\frac{\partial(\rho_h h_h)}{\partial t} + \nabla.(\rho_h h_h \vec{v}) = \nabla.(k_h \nabla T_h) - \nabla.\left(\rho_h h_h \vec{V}_h\right) - \dot{Q}_{eh}^{el} \quad (2.19)$$

ρ_h, h_h, k_h and T_h are the mass density, specific enthalpy, thermal conductivity and temperature of heavy particles, respectively. If the average thermal energy change $\dot{Q}_{ch}$ is included in the electron energy equation separately, then it is subtracted from the right hand side of equation (2.19).

2.4.6 Electric potential equation

$$\nabla.\left(\sigma \nabla \phi_{eff}\right) = 0 \quad (2.20)$$

where σ is the electric conductivity of the gas, ϕ_{eff} is the effective electric potential, which has the relationship with current density $\vec{j}$ as follows

$$\vec{j} = -\sigma \nabla \phi_{eff} = \sigma \vec{E}_{eff} = \sigma(\vec{E} + \frac{\nabla p_e}{e n_e}) \quad (2.21)$$

2.4.7 Magnetic potential equation

$$\nabla^2 \vec{A} = -\mu_0 \vec{j} \tag{2.22}$$

where μ_0 is the permeability in vacuum, $\vec{A}$ is the magnetic vector potential defined using the magnetic field $\vec{B}$ as,

$$\vec{B} = \nabla \times \vec{A} \tag{2.23}$$

2.4.8 Terms in conservation equations

The explicit forms of various conservation equations are given in (Ghorui, Heberlein, & Pfender, 2007). All the associated conservation equations have the generic form as follows:

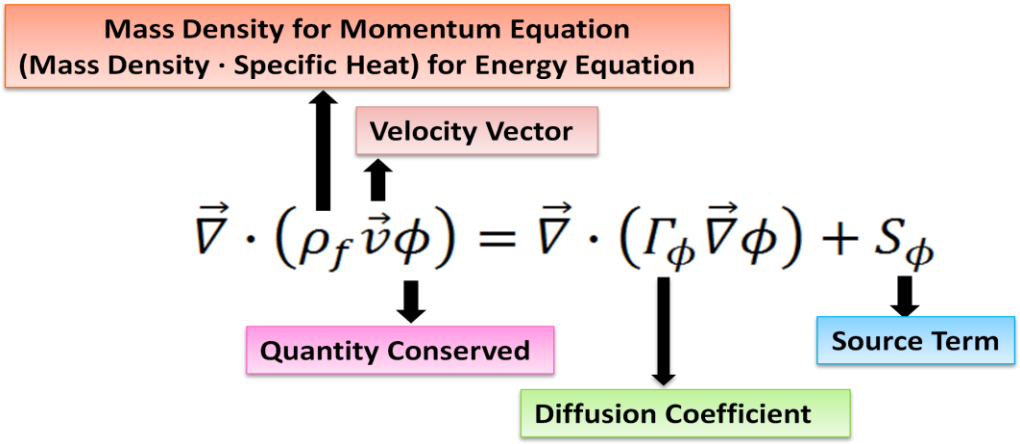

Figure 2.5: Generic form of conservation equations (Ghorui, Heberlein, & Pfender, 2007)

Table 2.1 describes the explicit forms of various conservation equations (Ghorui, Heberlein, & Pfender, 2007). Some of the source terms involving

V_r and V_θ contribute negligibly in the present simulation. Φ is the electric potential, p is the pressure. j_r and j_z are the radial and axial components of current density. ν, σ and c_{ph} are, respectively, viscosity, electrical conductivity and specific heat of heavy particles.

Table 2.1: Terms in conservation equations

Conservation of	$\emptyset$	$\boldsymbol{\Gamma_\emptyset}$	$\boldsymbol{S_\emptyset}$
Mass	1	0	0
Axial momentum	V_z	ν_{eff}	$-\frac{\partial p}{\partial z}+\frac{1}{r}\frac{\partial\left[r\nu_{eff}\left(\frac{\partial v_r}{\partial z}\right)\right]}{\partial r}+\frac{\partial\left(\nu_{eff}\frac{\partial v_z}{\partial z}\right)}{\partial z}$ $-\frac{2}{3}\nu_{eff}\frac{\partial(\nabla\cdot\vec{v})}{\partial z}+j_rB_\theta$
Radial momentum	V_r	ν_{eff}	$-\frac{\partial p}{\partial r}+\frac{1}{r}\frac{\partial\left[r\mu\left(\frac{\partial v_r}{\partial r}\right)\right]}{\partial r}+\frac{\partial\left(\nu_{eff}\frac{\partial v_z}{\partial r}\right)}{\partial z}-2\nu_{eff}\frac{v_r}{r^2}$ $-\frac{2}{3}\nu_{eff}\frac{\partial(\nabla\cdot\vec{v})}{\partial r}+\rho\frac{v_\theta^2}{r}+j_zB_\theta$
Azimuthal momentum	V_θ	ν_{eff}	$-\rho\frac{v_rv_\theta}{r}-\nu_{eff}\frac{v_\theta}{r^2}$
Potential	Φ	σ	0
Heavy-particle temperature	T_h	$k_h+c_{ph}\cdot k_{th}$	$-2\nu_{eff}\left[\left(\frac{\partial v_r}{\partial r}\right)^2+\left(\frac{\partial v_z}{\partial z}\right)^2+\frac{v_r^2}{r^2}\right]$ $+\left[\left(\frac{\partial v_r}{\partial z}+\frac{\partial v_z}{\partial r}\right)^2\right.$ $\left.+\left(\frac{\partial v_\theta}{\partial r}-\frac{v_\theta}{r}\right)^2+\left(\frac{\partial v_\theta}{\partial z}\right)^2\right]$ $-\frac{2}{3}\nu_{eff}(\nabla\cdot\vec{v})^2-p(\nabla\cdot\vec{v})+\dot{E}_{eh}$
Electron temperature	T_e	k_e	$\frac{j_r^2+j_z^2}{\sigma}+\frac{5}{2}\frac{k_B}{e}\left(j_z\frac{\partial T_e}{\partial z}+j_r\frac{\partial T_e}{\partial r}\right)-4\pi U_r$ $-\dot{E}_{eh}$

The self-induced magnetic field B_θ at radial location r is computed integrating j_z as $B_\theta(r) = \frac{\mu_0}{r}\int_0^r j_z y\, dy$, where μ_0 is the permeability of vacuum.

$\dot{E}_{eh}$ represents the energy transfer from electrons to heavy particles given by:

$\dot{E}_{eh} = \sum_h \frac{2}{3} k_B (T_e - T_h) n_e (\frac{2m_e}{m_h}) \bar{\nu}_{eh}$ and $\bar{\nu}_{eh} = \bar{C}_e n_h Q_{eh}$.

where, n_e and n_h are, respectively, number density of electrons and heavy particles. m_e and m_h are their respective masses. $\bar{\nu}_{eh}$ is the average volumetric collision frequency between electrons and heavy particles. $\bar{C}_e$ is the average thermal speed of electrons and Q_{eh} is the collision cross-section between electrons and heavy particles.

2.5 Boundary conditions

To specify the boundary conditions for pressure, velocity and other variables, consider a typical computational domain like the one shown in Figure 2.5. It has boundary conditions of the types: inlet, outlet, wall and symmetry.

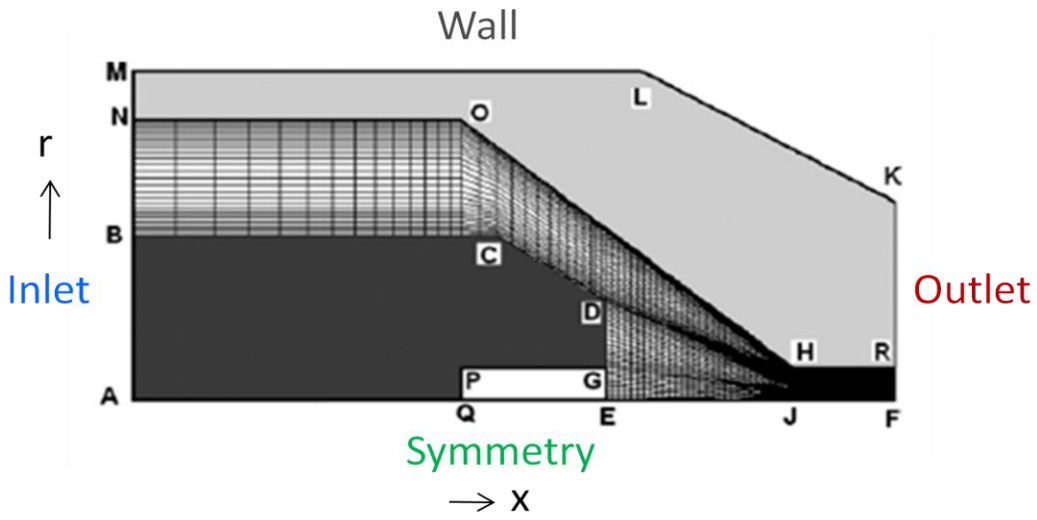

Figure 2.6: A typical computational domain with boundary conditions (Li, Heberlein, & Pfender, 2004)

A set of boundary conditions based on the Figure 2.5 for a typical torch with axial injection is given in Table 2.1.

Table 2.2: A typical set of boundary conditions

Boundaries	**P (atm)**	**u (m/s)**	**v (m/s)**	**w (m/s)**	**T (K)** ($\mathbf{T_e}$ **and** $\mathbf{T_h}$)	**Φ (V)**
BN	$Inlet\ Pressure$	-	0	$-u\tan\theta$	300	$\frac{d\phi}{dx}=0$
BCDG	-	0	0	0	1000	0
GE	-	0	0	0	3000	$\phi=\phi_j$
RF	-	$\frac{du}{dx}=0$	0	$\frac{dw}{dx}=0$	$\frac{dT}{dx}=0$	0
NOHR	-	0	0	0	$\frac{dT_e}{dr}=0$ $T_h=600$	-
EF	-	$\frac{du}{dr}=0$	0	$\frac{dw}{dr}=0$	$\frac{dT}{dr}=0$	$\frac{d\phi}{dr}=0$
MLKR	-	-	-	-	-	$\frac{d\phi}{dn}=0$

where, $\theta = Swirl\ injection\ angle,\ \phi_j$ is derived from current density boundary conditions and *n* represents the normal direction.

2.6 Property data

For the compressible flow and heat transfer simulations with oxygen-nitrogen as the plasma working gas, tabulated pressure-temperature-dependent thermodynamic and transport properties of oxygen plasmas in wide pressure and temperature ranges were calculated with formerly developed computer code (Ghorui, Heberlein, & Pfender, 2007) for the calculation of composition, thermodynamic and transport properties of equilibrium/non-equilibrium oxygen-nitrogen plasmas.

Thermodynamic and transport properties were computed for a 17 species model of nitrogen-oxygen plasma under different degrees of thermal non-equilibrium, pressures and volume ratio of component gases. In the computation electron temperature ranged from 300 to 45000K, mole fraction ranged from 0.8 to 0.2, pressure ranged from 0.1 atm to 5 atm and thermal non-equilibrium parameter (T_e/T_h) ranged from 1 to 20. It was assumed that all the electrons followed a temperature T_e and the rest of the species in the plasma followed a temperature T_h. Compositions were calculated using the two temperature Saha equation with appropriate energy level data and recently developed collision integrals were used to obtain thermodynamic and transport properties. The results were compared with published data under LTE conditions and an overall good agreement was observed (Ghorui, Heberlein, & Pfender, 2006).

Linear interpolation was employed for computing the physical properties at different gas pressures and temperatures. The radiation loss rate of oxygen plasmas (W/ m^3) in the temperature range of 9000 K to 30000 K at atmospheric pressure was obtained from experimental work (Gleizes & Cressault, 2007) and appropriate extrapolations were applied along with suitable pressure dependence relations.

2.7 Features of FAST-2D

The governing equations described in earlier sections are solved by using the FAST-2D solver with the following features.

Table 2.3: FAST-2D at a glance

	Features	Description
1	FAST-2D	**F**low **A**nalysis **S**imulation **T**ool of **2-D**imension developed by Zhu (1991) based on program by S. Majumdar (1986), Institute of Hydromechanics, University of Karlsruhe, Germany.
2	Discretization technique	Finite volume
3	Grid type	Non-orthogonal
4	Variable arrangement	Non-staggered
5	Pressure velocity coupling algorithm	SIMPLEC (Van Doormal and Raithby, 1984)
6	Scheme to avoid oscillation faced with non-staggered grid arrangement	Rhie and Chow (1983) momentum interpolation scheme
7	Convection differencing schemes	(a) hybrid /central/upwind (Spalding, 1972) (b) QUICK (Leonard, 1979) (c) SMART (Gaskell and Lau, 1988) (d) SOUCUP (Zhu and Rodi, 1991) (e) HLPA (Zhu,1991)
8	Solution scheme	(a) TDMA (alternate direction) of Thomas (Flecher, 1988). (b) Strongly implicit procedure (Stone, 1968)
9	Turbulence	k-epsilon (Launder and Spalding, 1974)

The general steps in FAST-2D for solving the governing equations with the appropriate boundary conditions discussed in the former sections are given below. The non-equilibrium thermodynamic and transport properties of oxygen-nitrogen plasma, required to solve the governing equations are derived by (Ghorui, Heberlein, & Pfender, 2007).

1) Initialize all fields (p*, u*, v* etc.). "*" represents the initial/guessed value of any variable.
2) Solve the u (axial) and v (radial) momentum equations using guessed pressure field p*.
3) Solve the pressure correction equation (from the continuity equation) to get p' (pressure correction) field.
4) $p = p^* + p'$; With the corrected pressure, correct the velocities and fluxes at the cell centers and faces.
5) Solve the w.r (azimuthal) momentum equation for the swirling flows.
6) Solve the turbulence equations (optional)
7) Solve the enthalpy equation.
8) Solve the electron energy equation.
9) Solve the electric potential equation.
10) Solve the diffusion equation for electrons.
11) Solve the diffusion equation for ions.
12) Solve the heavy-particle energy equation.

2.8 Solution procedure

The flow chart of the program is given in Figure 2.6. The complete program FAST-2D has three main parts: the pre-processor which is problem dependent, the solver and the post processor which are problem independent. The post processing is taken care of by graphics software TECPLOT; however, the pre-processing which includes the generation of the grid for the simulation needs to be addressed by means of a suitable mesh generator. It should also be considered that although the solver is problem independent, the pre-processor depends heavily on the geometry of the torch used.

The modifications of FAST-2D, to allow the simulation of different cases, rely on a USER routine, which should include all the user-specified parameters for the solution, and the MAKEGRID routine, which specifies the geometry of the torch to be simulated. Any parameter not specified in either USER.f or MAKEGRID.f needs to be modified manually in the source code. The initial conditions along with the current density boundary condition at the cathode are specified in various subroutines under the "preliminaries" block in the flow chart. The boundary conditions, source terms and the oxygen-nitrogen property data are specified / obtained before calling the solver (FAST-2D). The output files (for distribution of the plasma field quantities) are generated by the solver which are then post-processed using various graphic / analysis software. The program stops when the convergence criterion (total number of iterations or RMS residual $\leq$ allowed error ε) is satisfied.

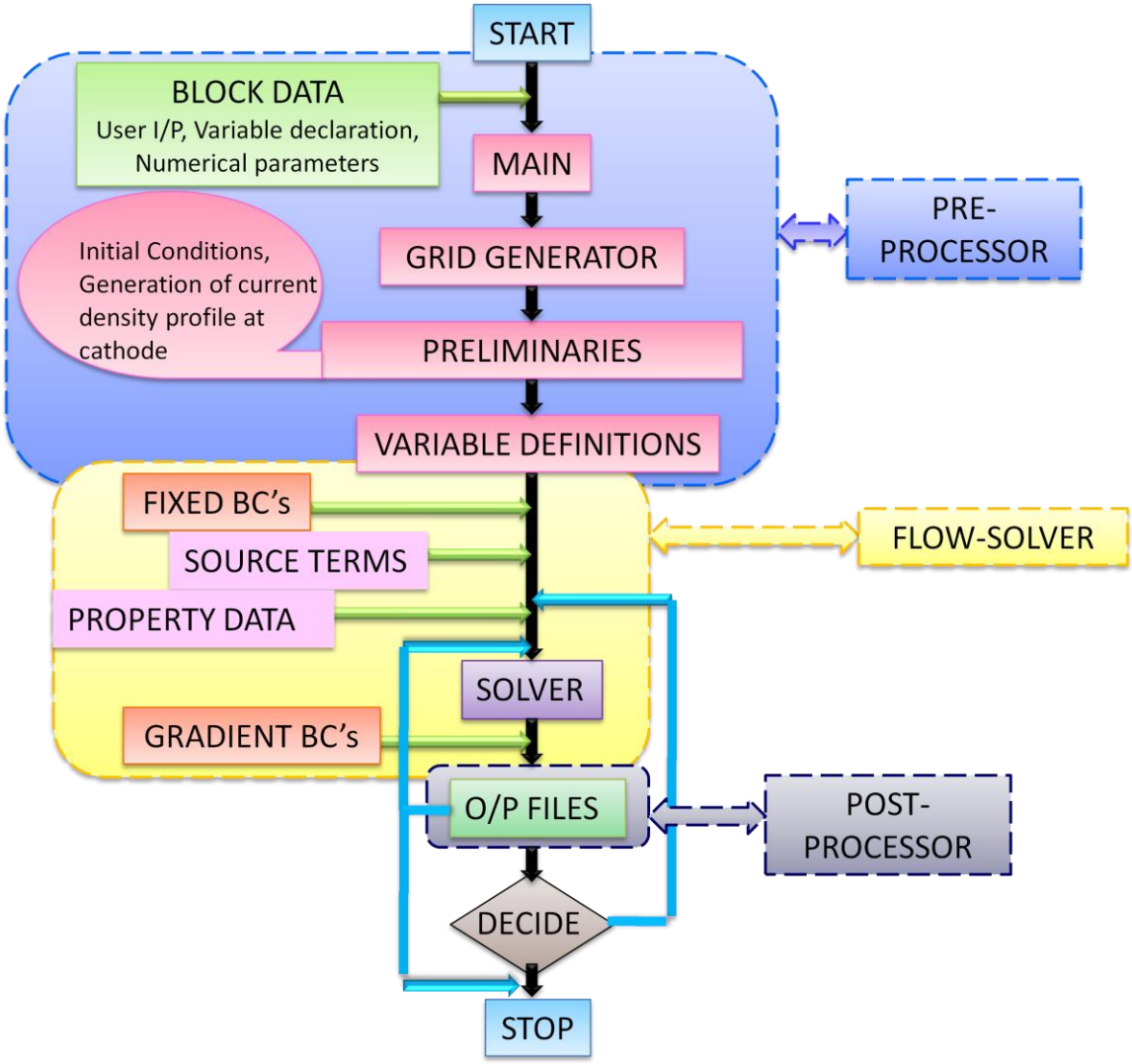

Figure 2.7: Flow chart for NEQ code

The variables used in FAST-2D and the subroutines in the non-equilibrium plasma code along with their purpose, are listed in appendices A and B.

3. GRID GENERATION

3.1 Introduction

The original pre-processor of the FAST-2D solver did not have an inbuilt finite volume grid generator fitting the torch geometry. Since the grid plays the most important role in getting a converged solution, a flexible grid generator is extremely necessary. This section describes a general routine developed to serve this purpose, its limitations and the improvements made to overcome these limitations.

The older version of the grid generator program required 23 measured dimensions of the plasma torch as an input whereas the new version requires 28 of those. These dimensions are usually readily available from the engineering drawings of the plasma cutting torches. Once the dimension data are entered, the geometry is specified and the program then divides the torch geometry into various computational zones as described in the subsequent sections. The number of grid points in each zone and the choice of grid spacing distribution style are specified by the user. With these inputs taken from the user, the code generates a complete grid with the help of the zone boundary equation subroutines and the grid generator functions GRD, GRDC and GRDR described later in this chapter.

The torch geometry and computational mesh used to describe the fields in it are specified in the routine MAKEGRID.f. This routine allows the specification of the torch geometry based on the use of “control nodes” and “zones”, as depicted in figures given later in this chapter. The geometry generated by MAKEGRID.f includes, apart from the

fluid region inside the torch, the solid regions (i.e. cathode, nozzle, etc.) and a part of the outside of the torch.

3.2 Old grid generator

3.2.1 Control points of the plasma torch geometry

The older version of the grid generator required 23 dimensions needed to be measured for the considered torch as illustrated in Figure 3.1. Bars associated with each w_n and h_n dimensions indicate the lengths to be measured.

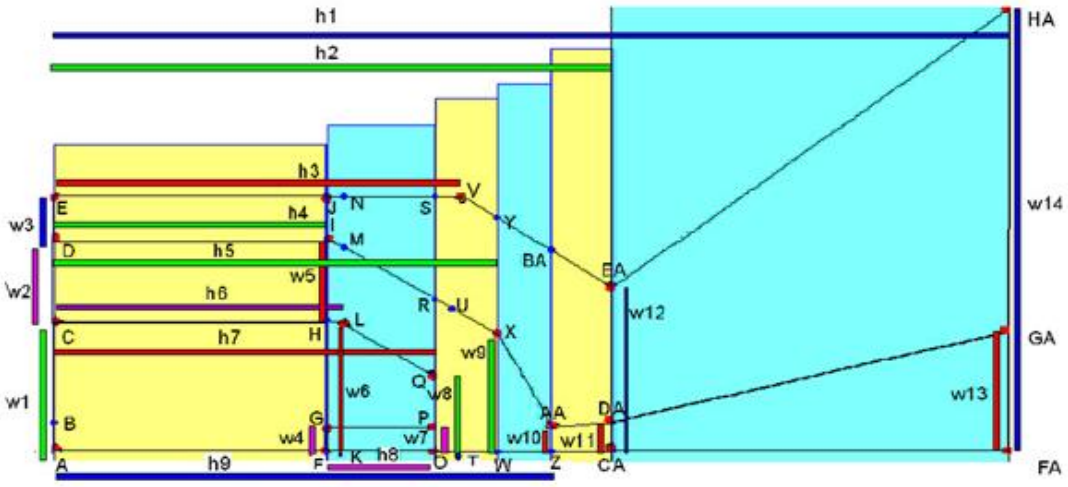

Figure 3.1: Control points and dimensions of plasma torch geometry in older version of grid generator (Ghorui, Heberlein, & Pfender, 2007)

3.2.2 Coordinates extracted from the dimensions

The derived coordinates for the chosen example are:

Table 3.1: Control points'co-ordinates

Control Point	X-Coordinate	Y-Coordinate
A	$X_A = 0$	$Y_A = 0$
B	$X_B = 0$	$Y_B = W4$
C	$X_C = 0$	$Y_C = W1$
D	$X_D = 0$	$Y_D = W1+W2$
E	$X_E = 0$	$Y_E = W1+W2+W3$
F	$X_F = (H7-H8)$	$Y_F = 0$
G	$X_G = XF$	$Y_G = W4$
H	$X_H = H4$	$Y_H = W6$
I	$X_I = H4$	$Y_I = W6+W5$
J	$X_J = H4$	$Y_J = YE$
K	$X_K = H6$	$Y_K = 0$
L	$X_L = H6$	$Y_L = W6$
M	$X_M = H6$	Y_M = DERIVED POINT*
N	$X_N = H6$	Y_N = DERIVED POINT
O	$X_O = H7$	$Y_O = 0$
P	$X_P = H7$	$Y_P = W7$
Q	$X_Q = H7$	$Y_Q = W8$
R	$X_R = H7$	Y_R = DERIVED POINT
S	$X_S = H7$	Y_S = DERIVED POINT
T	$X_T = H3$	$Y_T = 0$
U	$X_U = H3$	Y_U = DERIVED POINT
V	$X_V = H3$	$Y_V = W1+W2+W3/2.$
W	$X_W = H5$	$Y_W = 0$
X	$X_X = H5$	$Y_X = W9$
Y	$X_Y = H5$	Y_Y = DERIVED POINT
Z	$X_Z = H9$	$Y_Z = 0$
AA	$X_{AA} = H9$	$Y_{AA} = W10$
BA	$X_{BA} = H9$	Y_{BA} = DERIVED POINT
CA	$X_{CA} = H2$	$Y_{CA} = 0$
DA	$X_{DA} = H2$	$Y_{DA} = W11$
EA	$X_{EA} = H2$	$Y_{EA} = W12$
FA	$X_{FA} = H1$	$Y_{FA} = 0$
GA	$X_{GA} = H1$	$Y_{GA} = W13$
HA	$X_{HA} = H1$	$Y_{HA} = W14$

*Note: "Derived Points" are obtained using the zone boundary functions

After extracting the control points from the torch drawing, the solid and fluid zone boundaries are derived from the defined boundary functions. The resulting frame for grid generation is shown in Figure 3.2.

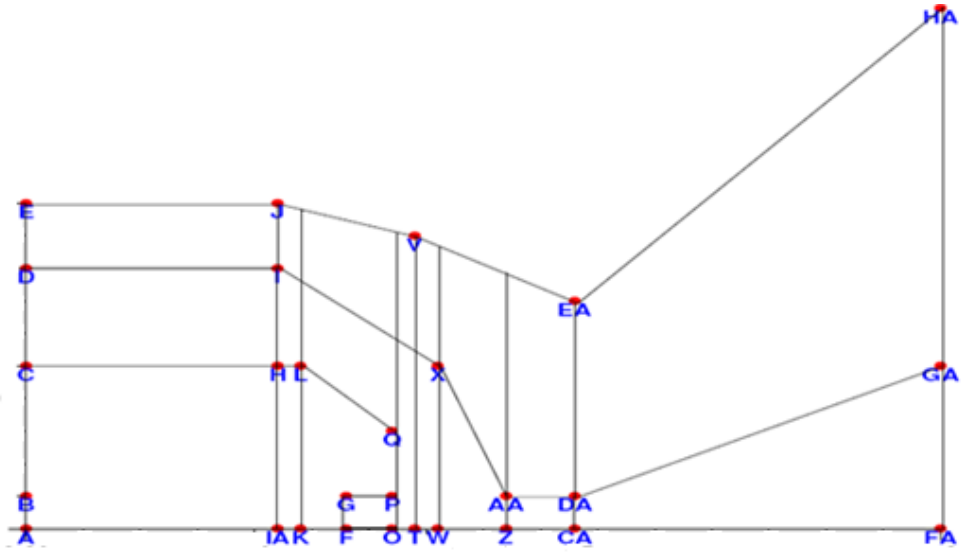

Figure 3.2: Frame for grid generation with zone boundaries (Ghorui, Heberlein, & Pfender, 2007)

3.2.3 Zones in radial direction (X-zones)

The zones created are dependent on the geometric features of the torch and are chosen to ease the setting of the boundary conditions. In the older version of the geometry subroutine, zone-2 was shaped to handle the hafnium insert in the cathode. Zone-3 handled the surface condition of the cathode tip; zone-4 modeled the nozzle exit and zone-5 handled the outflow zone. Also, five different grid distributions could be chosen in five different zones described above. These X-zones are shown in Figure 3.3.

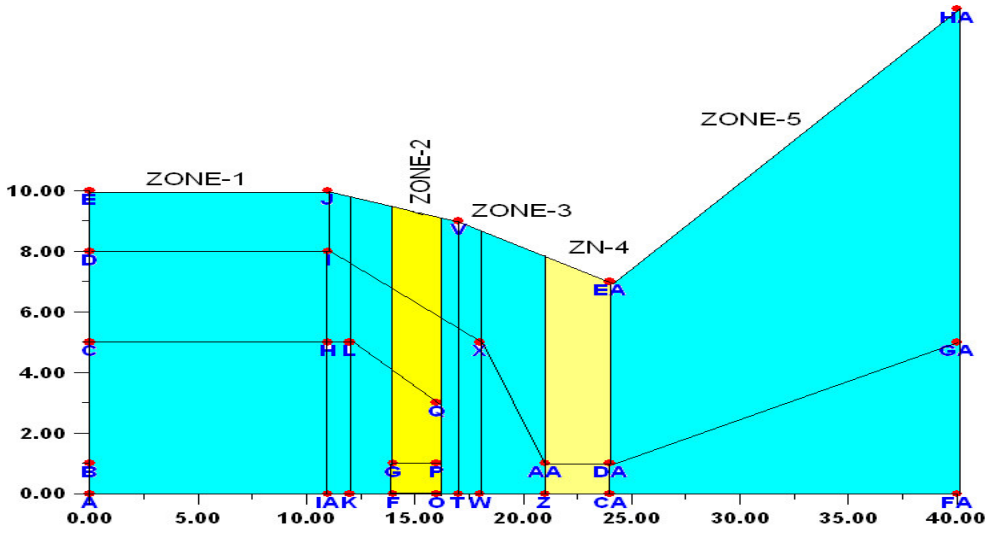

Figure 3.3: Zones in radial direction (X-zones) (Ghorui, Heberlein, & Pfender, 2007)

3.2.4 Zones in axial direction (Y-zones)

Similar to the case of X-zones, the Y-zones were chosen to specify the boundary conditions easily. Zone-1 handled the hafnium insert, zone-2 handled the cathode surface, zone-3 consisted of gas flow region, and zone-4 handled the nozzle wall. Zone-5 was the plasma formation and expansion zone. Zone-6 covered part of the nozzle wall and outflow zone. Zone-5 and zone-6 did not require grid number and style specifications as they were dependent on the specifications set in zone-1 to zone-4.

Four different grid distribution types were chosen for four different zones up to the cathode tip and then only two different types of grid distributions were chosen for the domain downstream as shown in Figure 3.4.

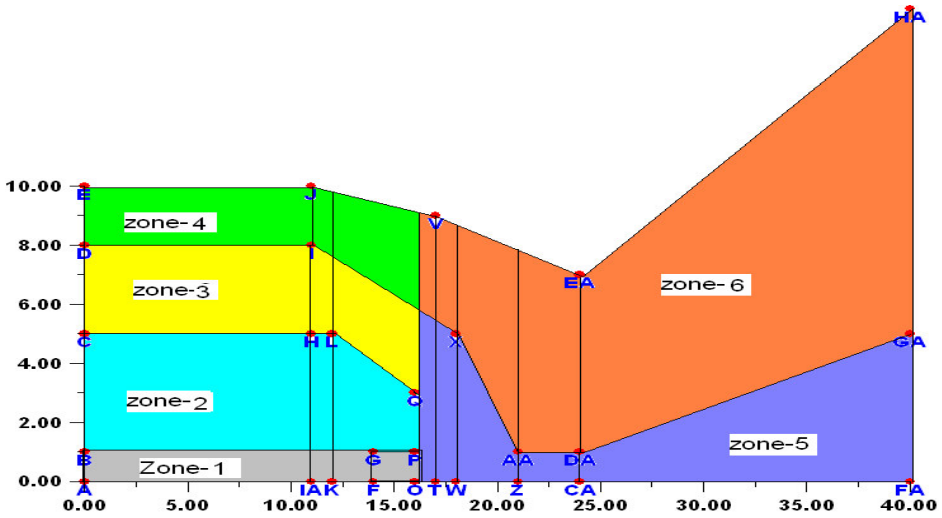

Figure 3.4: Zones in axial direction (Y-zones) (Ghorui, Heberlein, & Pfender, 2007)

3.2.5 Zone boundary functions

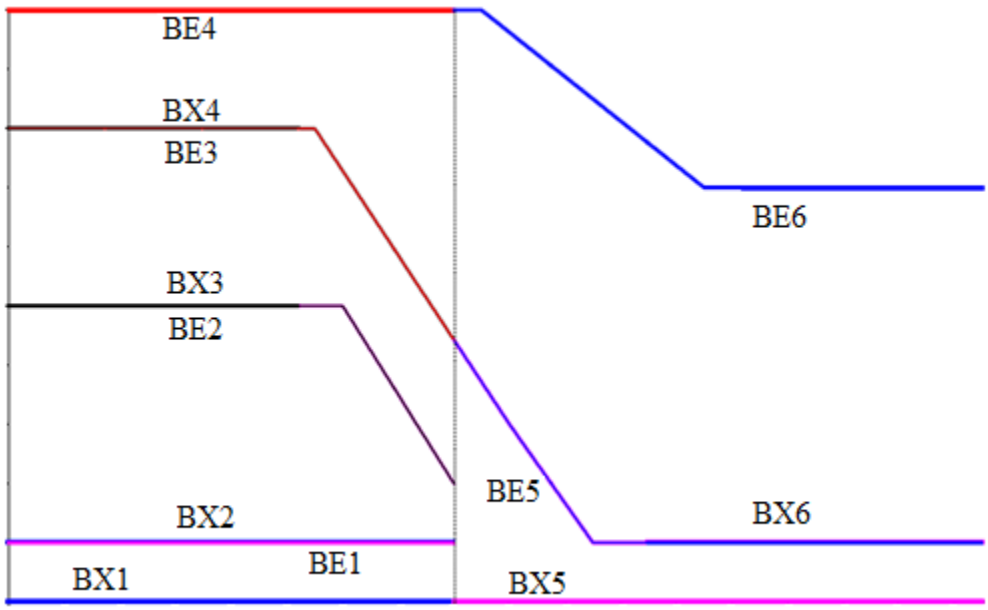

Figure 3.5: Zone boundary functions (Ghorui, Heberlein, & Pfender, 2007)

Functions were developed to extract equations for boundaries of every zone. These functions, as shown in Figure 3.5, computed the equations for the zone boundaries. For a given x-coordinate, boundary functions gave the y-coordinate at a particular zone boundary. Once all the boundaries were obtained, the next step was to discretize the lengths with optimum grid density at associated regions.

3.2.6 Functions employed for generating grids of varying densities

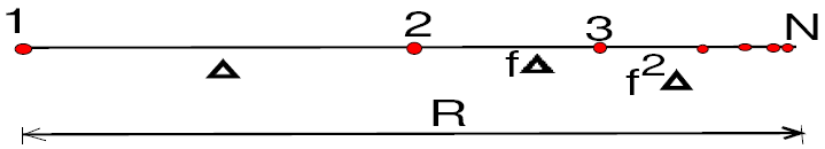

Figure 3.6: Example of varying density grid (Ghorui, Heberlein, & Pfender, 2007)

In the above example, a range 'R' is discretized by 'N' grid points such that the distance between consecutive nodes is a factor 'f' of the distance between the previous set of consecutive nodes.

Therefore,

$$\Delta + f.\Delta + f^2.\Delta + \cdots \ldots \ldots \ldots + f^{N-2}.\Delta = R$$

That is $\Delta = R.\frac{f-1}{f^{N-2}-1}$

For f<1 we have an outward contracting grid and for f>1, we have an outward diverging grid. A few examples of varying-density grids are presented below. For f=1, the function needs special care due to 0/0 form.

Function **GRD(f,r,n)** generates grid points of following types:

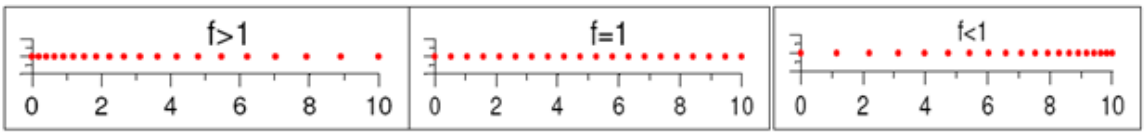

Figure 3.7: Varying density grid asymetric about the center (Ghorui, Heberlein, & Pfender, 2007)

Function **GRDC(f,r,n)** generates grid points of following types:

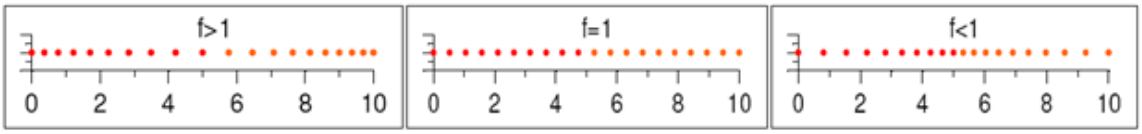

Figure 3.8: Varying density grid symmetric about the center (Ghorui, Heberlein, & Pfender, 2007)

Function **GRDC(f,r,n)** uses the Function **GRD(f,r,n)** in the first and the second half of the points in an order opposite to each other. Function **GRDR(r,n)** generates grid points when the ratio of the interval between consecutive grid points and the range is given. This is particularly advantageous in the zone where a number of zones of different styles merge into a single zone. This function has been used in the zone following the cathode tip.

The x-coordinates and the y-coordinates are derived using the functions discussed above as shown in Figures 3.9 and 3.10 respectively

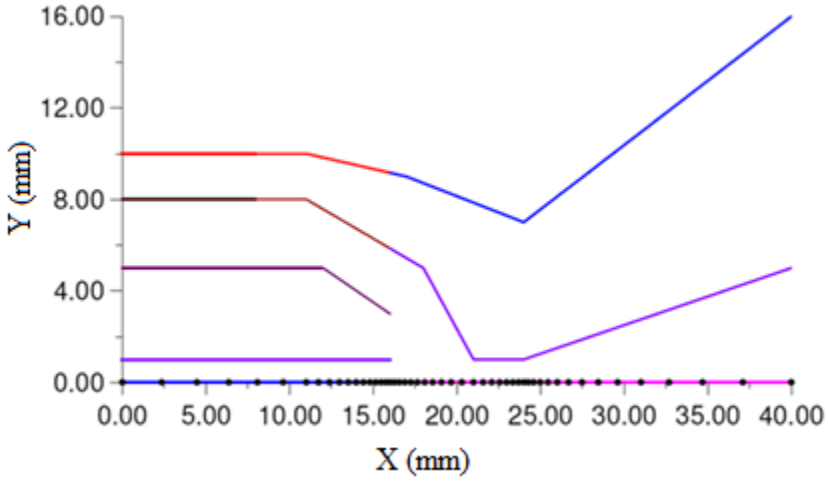

Figure 3.9: Assigning x-coordinates using the grid density functions (Ghorui, Heberlein, & Pfender, 2007)

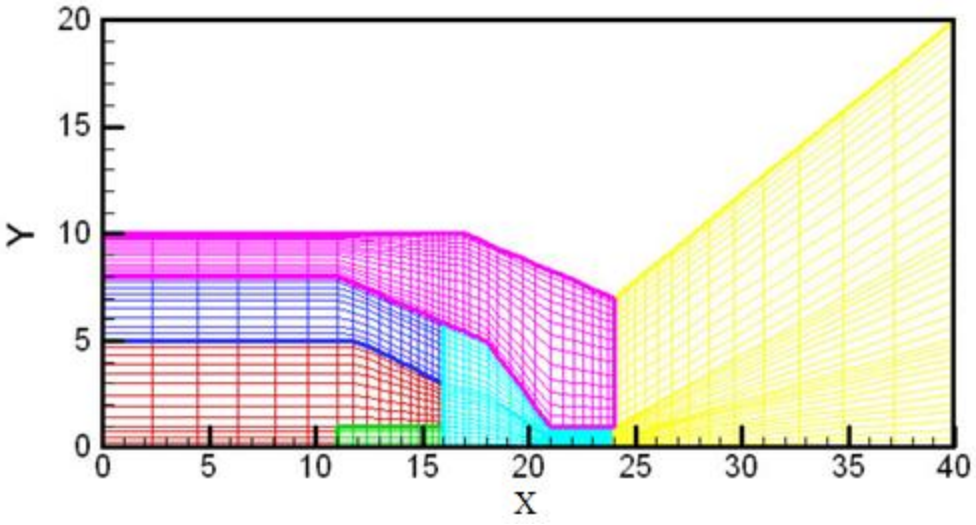

Figure 3.10: Assigning y coordinates using the grid density functions (Ghorui, Heberlein, & Pfender, 2007)

3.2.7 Geometric limitations in FAST-2D and MAKEGRID

The complete geometry of all Hypertherm torches could not be modeled using the earlier version of the MAKEGRID.f file, because this file only allowed the specification of a geometry using 23 control dimensions. Furthermore, it did not allow the specification of the nozzle counter-bore, the cone at the torch exit and the vent flow. Also, the parameters specified in MAKEGRID are "hard-wired" into the rest of the FAST-2D solver. The swirl injection radius could not be specified in the USER routine, nor was it specified explicitly in the MAKEGRID routine. The approach used previously for considering the location of the swirl gas injection, consisted of assigning it to a given node in the mesh, describing the inlet of the flow injection point – this is done in the BOUNDS.f file (the file where part of the boundary conditions are specified). This approach made the swirl injection radius mesh-dependent; therefore non-flexible and unreliable. Moreover, the size of the gas injection holes could not be specified in the MAKEGRID.f file. This section addresses the work done towards improving these aspects of the user-specified part of the FAST-2D code.

3.2.8 Current geometry/mesh-generation routine

The above limitations of the MAKEGRID.f routine arise from the fact that the generated mesh is structured, having the axis of the torch as the driven direction, and uses a fixed amount of control points.

Apart from the above limitations, an even more important issue for the use of FAST-2D for the modeling of the Hypertherm HT4400And vented 400A process plasma torches is that the MAKEGRID.f file is tightly coupled to several routines in FAST-2D. These files are not only the files used for the definition of the boundaries of the domain and boundary conditions, but also to the routines in the "problem-independent" part of the code. Therefore, any modification of the MAKEGRID.f file needs to be consistent with not only the boundary specification and boundary conditions files, but also with all the routines in FAST-2D that rely on the specific form of MAKEGRID.f.

Therefore, in order to use FAST-2D to simulate the new generation cutting torches by Hypertherm Inc., the file MAKEGRID.f needed to be modified/rewritten, as well as all the routines in FAST2D that rely on the parameters used in MAKEGRID (e.g. for the NEQ code, the routines MAIN.f, BOUNDS.f, FILES_SPEBND.f, INITIA_CURRENT.f, OVACON.f, SETJ.f, SOURCE.f).

3.3 New geometry/mesh-generation routine

To simulate the HT4400 400A O_2 and vented 400A process cutting torches, the file MAKEGRID.f was missing the following features:

1. Location and size of the swirl injection.
2. Counter-bore or conical expansion at the nozzle outlet.
3. Vent flow channel.

The new MAKEGRID routine was based on the geometrical specifications depicted in Figure 3.11 According to Figure 3.11, each boundary of the computational domain (cathode, nozzle inside, etc.) is determined by a set of control points. The torch geometry is given by 4 profiles: the insert (i), cathode (c), nozzle inside (n), and nozzle outside (t). Each one of these profiles is specified by a set of "control points" (i.e. for the cathode profile, the points 1c, 2c, and 3c).

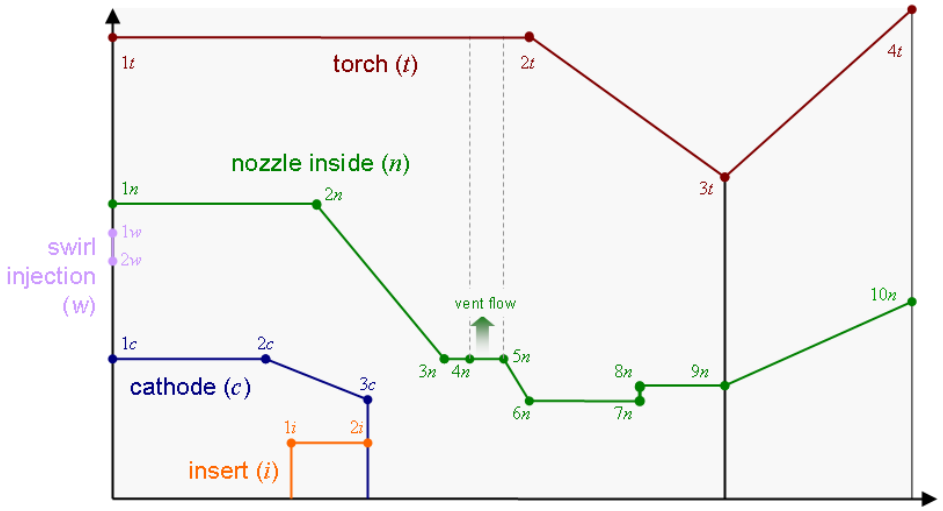

Figure 3.11: New geometry/mesh-generation specification for the file MAKEGRID.f

One disadvantage of the geometry specification given in Figure 3.11 is that the vent flow channel has to be modeled as vertical. This is due to the structured nature of the

mesh generation routine, consistent with the capabilities of FAST-2D. Furthermore, the shield flow channel cannot be included. Addition of the shield gas flow will require further modification of the MAKEGRID routine. Table 3.2 shows a summary of the current and new number of control points used in MAKEGRID.f for the specification of the torch geometry.

Table 3.2: Comparison between old and proposed geometry/mesh-generation routine

	Number of "control-points"	
	Old	New
Insert	2	2
Cathode	3	3
Swirl injection	0	2
Nozzle inside	6	10
Torch	4	4
TOTAL:	**15**	**21**

3.4 Summary of features of new mesh generation routine

1. The new MAKEGRID.f routine allows the specification of axial, radial, and tangential gas injection, and/or combinations of these.
2. The new routine is able to describe the geometry of the vent channel. (The old MAKEGRID.f routine lacked an extra "control point" to allow the specification of the vent channel design).
3. The new routine allows the correct specification of the geometry of the nozzle exit, e.g. counter-bore and/or conical expansion.

4. The new MAKEGRID.f routine has the option, available in the original routine, to allow the simulation of the domain outside the torch (plasma jet) and the work piece.
5. The new routine is in a modular and user-friendly manner. This modularity makes the modification of the geometry specification (i.e. addition/removal of control points) straightforward and intuitive in order to accommodate future torch designs.

The new MAKEGRID routine is developed with "modularity" as the main goal. The new routine divides the spatial domain of the torch in "characteristic zones" along the X and Y axes. The X- and Y-zones currently considered in the new MAKEGRID.f routine are depicted in Figure 3.12. Each zone encompasses several "control points" along a given axis; i.e. in the X-zones plot in Figure 3.12, zone 4 contains 5 "control points": points 11 to 15. Therefore, the definition of "zones" along the X-axis is somewhat arbitrary, as they are specified to allow identification of particular regions of the domain for imposition of the boundary conditions. As an example, X-zone 2 is included to specify the boundary conditions for the radial gas injection, whereas X-zone 6 allows the specification of the vent channel.

3.5 New X- and Y- zones

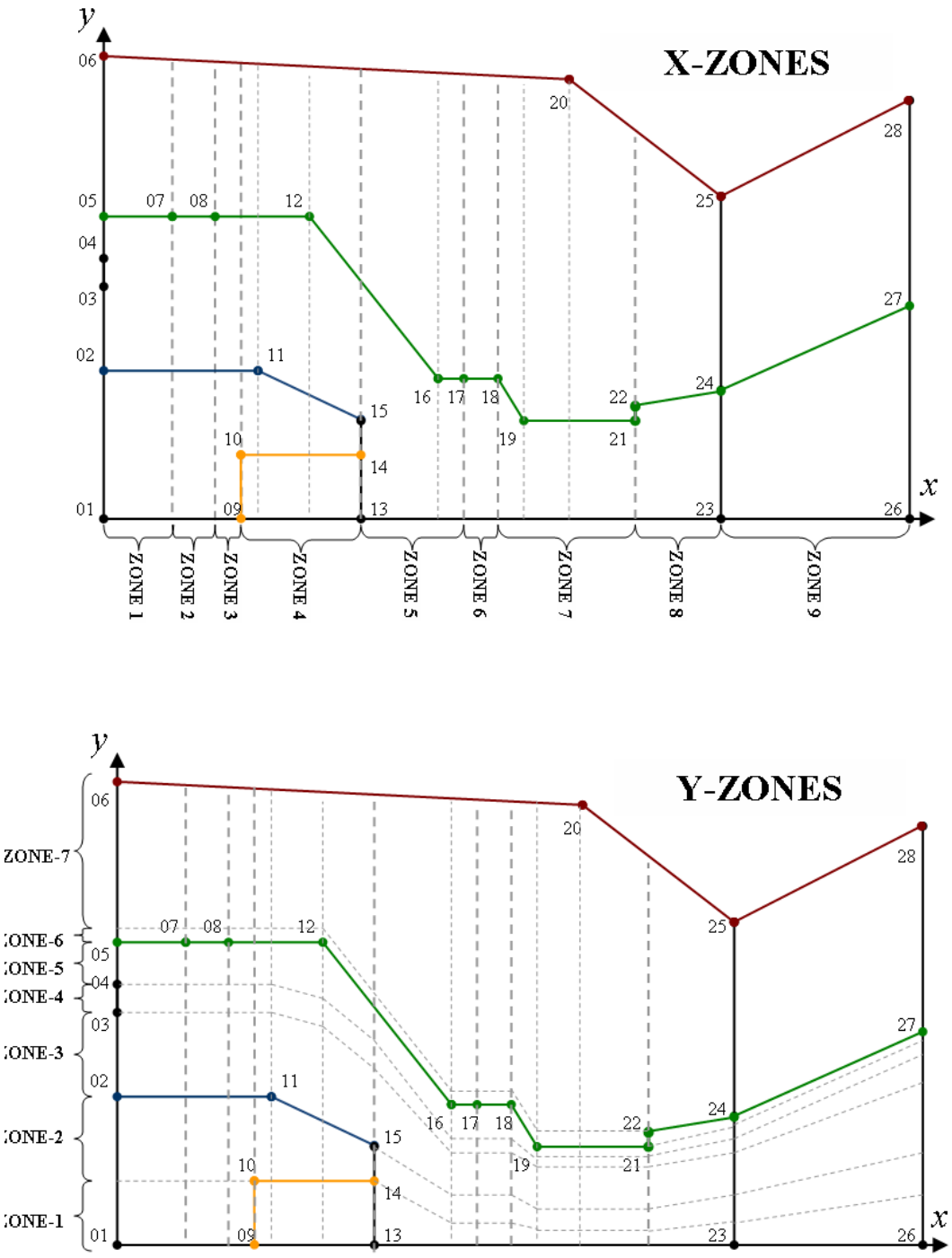

Figure 3.12: Zones along the x (*top*) and y (*bottom*) coordinates used to characterize general plasma torch geometries

The mesh generation routine consists of creating a quasi-orthogonal sub-mesh in each quadrilateral region delineated by the dashed lines in the Y-zones plot. The main objective of the new MAKEGRID.f routine is to create a sub-discretization of each quadrilateral sub-region given by the intersection of the sets of dashed lines in the Y-zones plot in Figure 3.12. That is, every quadrilateral region in this plot will be further divided into a user-specified number of grid nodes along the X- and Y-axis. The modularity of the new MAKEGRID.f routine will allow the addition or removal of any number of "control points" in a consistent manner, such that the domain will still be divided into quadrilateral sub-regions, which are subsequently discretized. The flow chart for grid generation subroutine is given in Figure 3.13. The factors FX_1 to FX_9 and FY_1 to FY_7 are the factors deciding the variations in grid densities.

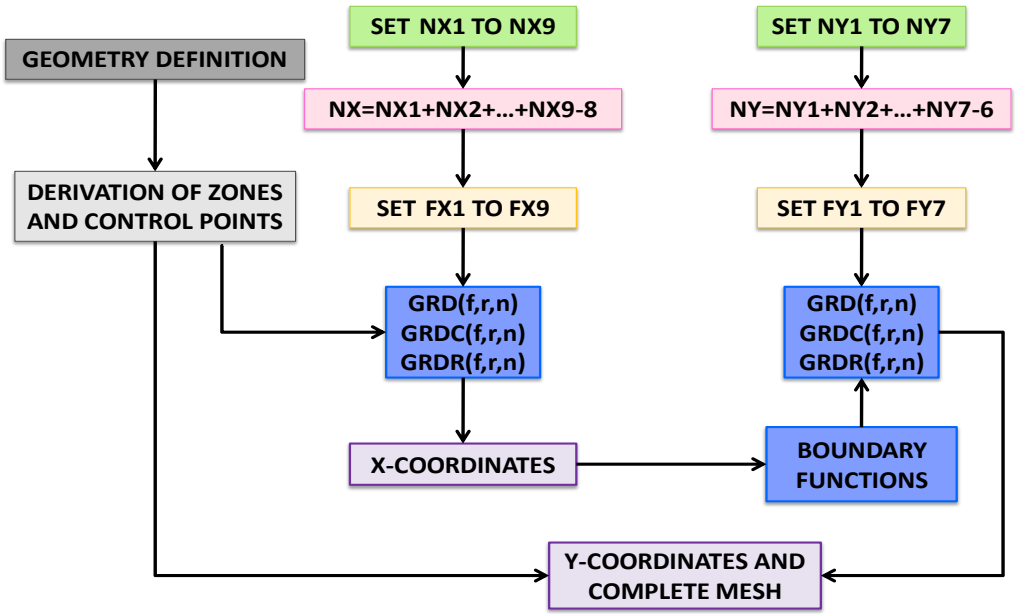

Figure 3.13: Flow chart for grid generation subroutine

3.6 Sample grids generated by the grid generation subroutine:

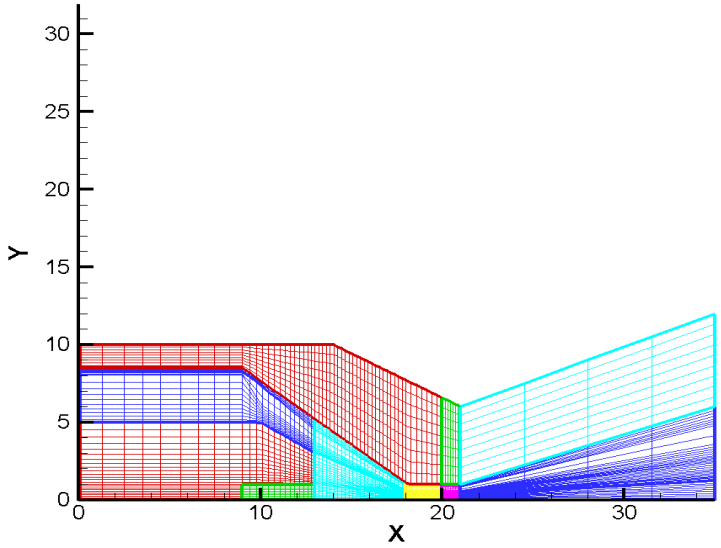

Figure 3.14: Grid for HT2000 (200A O_2/air process)

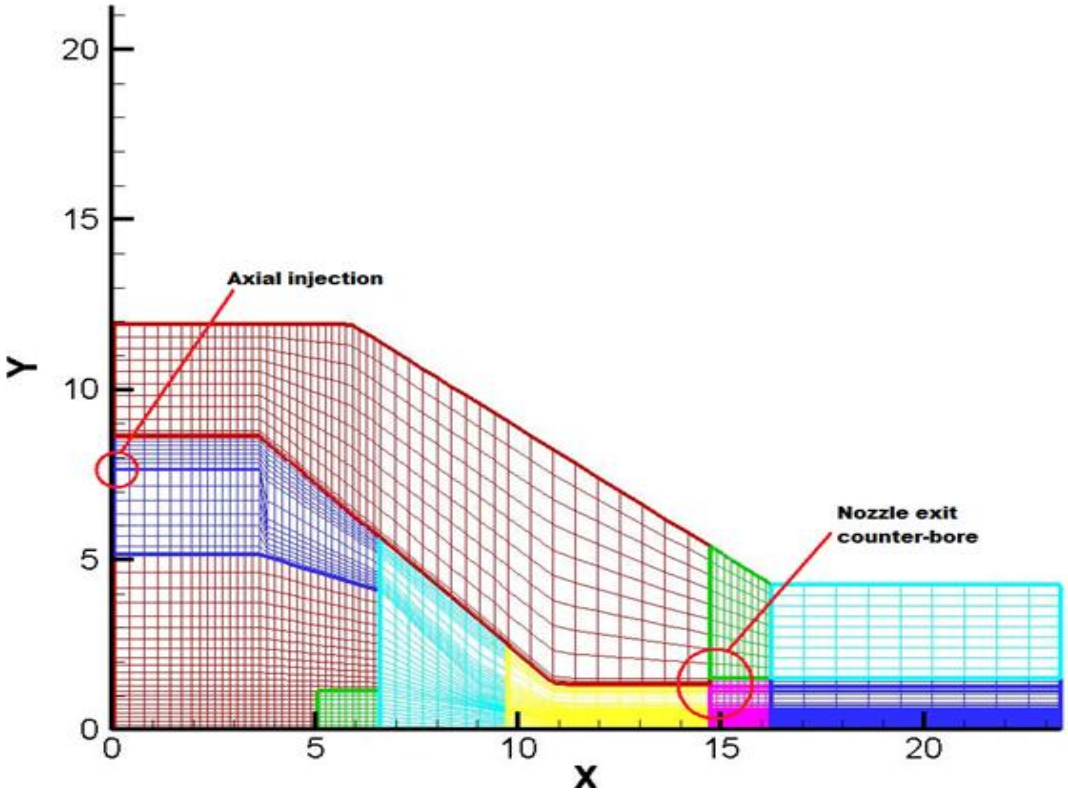

Figure 3.15: Grid for HT4400 (400A O_2/air process)

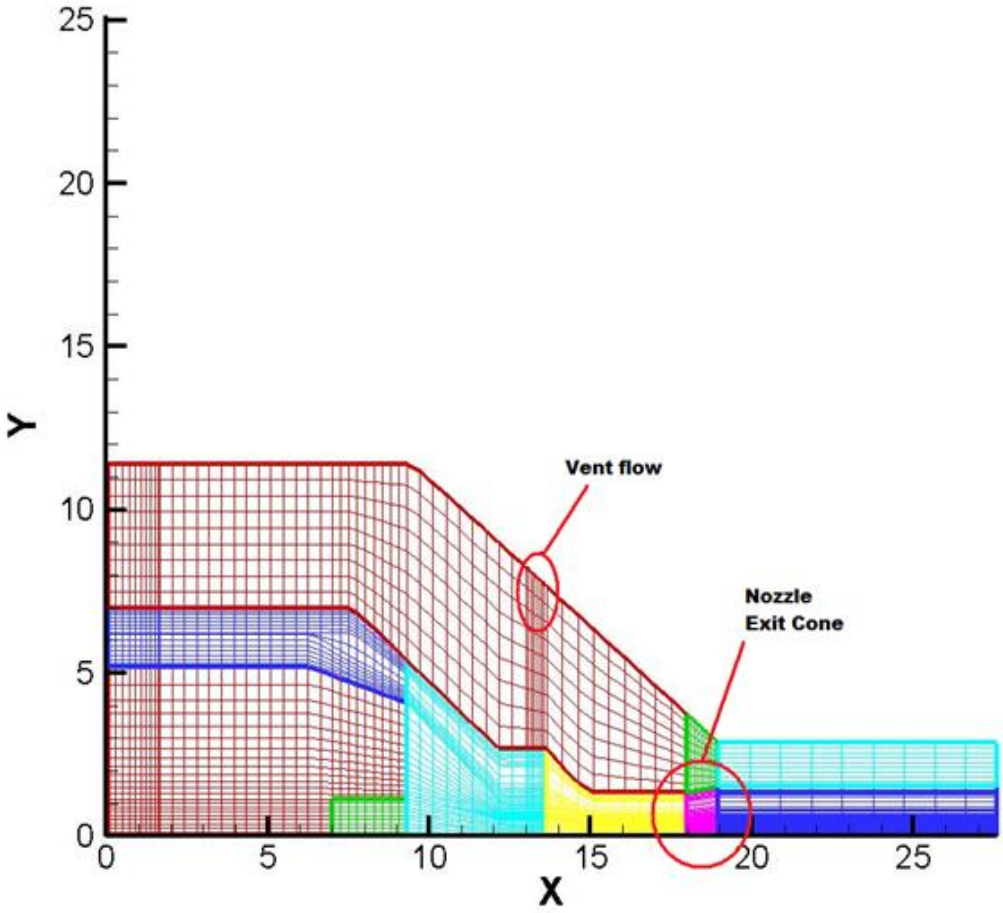

Figure 3.16: Grid for vented torch (400A O_2/air process)

The sample grids generated by the modified grid generation subroutine are shown in Figures 3.14 (for HT2000 torch), 3.15 (for HT4400 torch) and 3.16 (for 9427 O_2 Rev 1 torch). Various solid/fluid zones are shown in different colors. As emphasized by the diagrams, the modified grid generator features the ability to input axial injection zone, vent flow zone and nozzle exit counter bore or cone.

4. MODELING OF RADIATION LOSSES

4.1 Introduction

It has been observed that the radiation model has a significant effect on the distribution of plasma field quantities and therefore it is required to select an adequate radiation model in order to produce reasonable results. In the code, the radiation losses are modeled by the total effective volumetric radiation loss term. Such an approximation is widely employed in the thermal plasma community.

In this concept, self-absorption by the plasma is taken into account by assuming a plasma-geometry and solving the radiation transport for this assumed geometry. The geometry dependence is expressed in the terms of an effective radius of the radiating volume. If the effective radius $R_{eff} = 0.0\ mm$, there is no self-absorption and all radiation escapes. For increasing values of R_{eff}, some of the radiation is absorbed in the arc itself.

4.2 Energy transport in thermal plasmas

The thermal non-equilibrium feature expresses the transport of thermal energy by the two-temperature model. Two-temperature models do not assume that the electrons and the heavy-species in the plasma equilibrate instantaneously; therefore they allow partial kinetic equilibration and hence model the energy transport processes within the plasma flow more accurately than a single temperature model. The energy conservation equations solved in FAST-2D are of the form (Boulos, Fauchais, & Pfender, 1994):

$$Transient + Advection - Diffusion - Reaction = 0 \tag{4.1}$$

The terms composing these equations are displayed in Table 4.1.

Table 4.1: Terms in the thermal energy conservation equations

Variable	Transient	Advection	Diffusion	Reaction
T_h	$\frac{\partial \rho h_h}{\partial t}$	$\nabla \cdot \rho \vec{u} h_h$	$-\nabla \cdot \vec{q}'_h$	Q_{eh}
T_e	$\frac{\partial \rho h_e}{\partial t}$	$\nabla \cdot \rho \vec{u} h_e$	$-\nabla \cdot \vec{q}'_e$	$-Q_{eh} + Q_J - Q_r$

In Table 4.1, T_h = Heavy-species temperature

T_e = Electron temperature

h_h = Heavy-species enthalpy

h_e = Electron enthalpy

ρ = Mass density

u = Velocity

q' = Total effective heat flux (due to the transport of translational energy and species enthalpy by diffusion)

Q_{eh} = Net energy exchange term (explicit coupling between the energy equations)

Q_J = Joule heating

Q_r = Net volumetric radiation loss term

4.3 Net volumetric radiation loss

It is crucial to model the transport of radiative energy in a thermal plasma flow adequately in order to describe the plasma flow dynamics correctly. This term can especially dominate the energy transport at very high temperatures (i.e. temperatures greater than ~ 30000 K). Fundamentally, the net volumetric radiation density, which is the net energy emitted per unit volume and time, can be expressed by:

$$Q_r = -\nabla . \vec{q}_r$$

$$= \int_{4\pi} \int_0^{\infty} \left[I_\nu^{Bb}(\vec{x}) k_\nu(\vec{x}) - k_\nu(\vec{x}) \int_0^{\vec{x}} I_\nu^{Bb}(\vec{\xi}) k_\nu(\vec{\xi})\, e^{-\int_{\vec{\xi}}^{\vec{x}} k_\xi(\eta)\, d\eta}\, d\vec{\xi} \right] d\nu\, d\omega \tag{4.2}$$

where $\vec{q}_r$ = radiative flux

$\vec{x}$ = vector of spatial coordinates

k_ν = spectral absorption coefficient

I_ν^{Bb} = Planck function for a black body

$$I_\nu^{Bb} = \frac{8\pi h}{c^3} \frac{\nu^3}{e^{h\nu/k_B T} - 1} \tag{4.3}$$

where c = speed of light

h = Planck constant

k_B = Boltzmann constant.

The integration for Q_r in (4.2) is over all frequencies ν, all directions ω and over all sources ξ on the ray from the domain boundary ($\xi = 0$) to the point x under consideration. Expressions (4.2) and (4.3) indicate that Q_r is a complex function of the geometry containing the plasma flow and the local properties of the plasma.

4.4 The effective volumetric radiation loss approximation

In plasma flow simulations, the modeling of the radiative transfer given by (4.2) represents an exceedingly large effort (i.e. the number of calculations needed scales with the cube of *N*, the number of grid nodes (N^3)). The dominant approach used in the thermal plasma community to approximate the radiative energy exchange consists of the radiative transport model developed by (Lowke, 1974). Lowke's approach consists of modeling all radiation as being emitted in the center of an isothermal sphere with a characteristic *effective radiation radius* R_{eff}. Radiation can be reabsorbed only within this sphere. Therefore, radiation emitted in the arc has to pass through a certain distance of (not optically thin) plasma before escaping to the walls. By assuming that the sphere is isothermal and by assigning it a radius, three independent variables in equation (4.2) are removed, giving a total volumetric radiation term that depends only on the local temperature.

Lowke's model has some weaknesses, especially when considering that the arc must be given a characteristic radiation radius. Also, a plasma flow can have areas in the outer part where the absorption of radiation from the inner parts is higher than the emitted radiation, effectively giving a negative radiation loss. On the other hand, Lowke's model

provides a consistent and practical way of determining the radiation loss from thermal plasma, suitable for numerical simulation.

By assuming the spectral absorption k_ν and Planck function I_ν^{Bb} to be constants and integrating from $r = 0$ to R_{eff} over all angles in equation (4.2), the net volumetric radiation loss is given by:

$$Q_r = 4\pi \int_0^\infty I_\nu^{Bb} k_\nu e^{-R_{eff} k_\nu} d\nu = 4\pi \varepsilon_r(T, R_{eff}) \tag{4.4}$$

Here, ε_r is the net emission coefficient, which is a function of the plasma gas, the local temperature and the effective absorption radius R_{eff} (a model parameter). It is this net emission coefficient ε_r which approximates locally the radiative energy transfer from the plasma to its surroundings.

Lowke's model was originally derived for thermal plasmas in thermal equilibrium (i.e.$T_h = T_e = T$). For a thermal non-equilibrium plasma model, and considering that radiation depends mostly on the population of excited species and these, in turn depend primarily on the electron temperature, the expression given by (4.4) is evaluated as a function of the electron temperature T_e (i.e.$\epsilon_r = \epsilon_r(T_e)$).

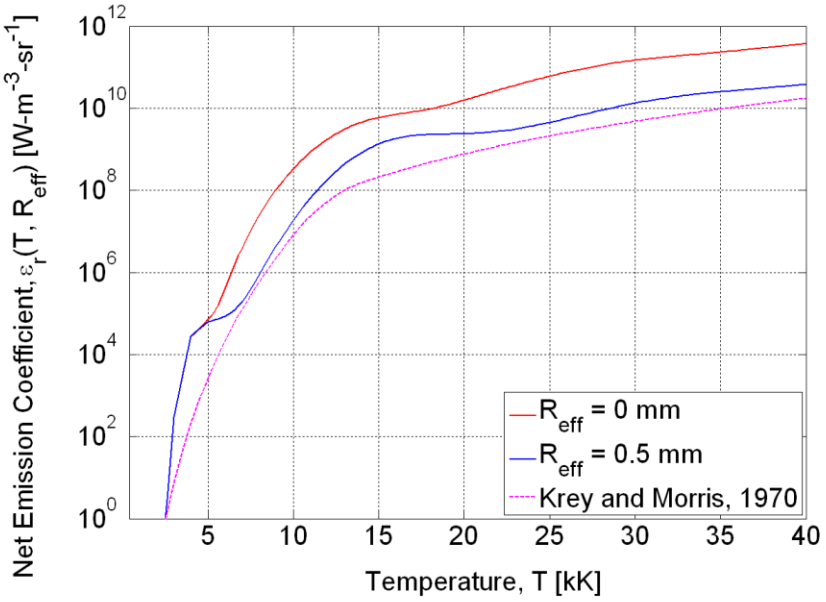

Figure 4.1: Effective net radiative emission coefficient for oxygen as a function of temperature: data previously used in FAST-2D (Krey & Morris, 1970), and new radiation data by (Gleizes & Cressault, 2007) for two effective absorption radii (R_{eff} = 0.0 & 0.5 mm)

The radiation model employed earlier used radiation data for oxygen plasma obtained by (Krey & Morris, 1970). The experimental data as reported by Krey and Morris span over temperatures in the range between 9000 and 14000 K. This data was curve-fitted and extrapolated and specified in the file O2RAD.DAT.

Figure 4.1 shows the radiation data previously used in FAST-2D (extrapolations of the data from Krey and Morris) and the radiation data calculated by (Gleizes & Cressault, 2007) for oxygen plasma for two representative effective radii: $R_{eff} = 0.0\ mm$ (optically thin) and $R_{eff} = 0.5\ mm$.

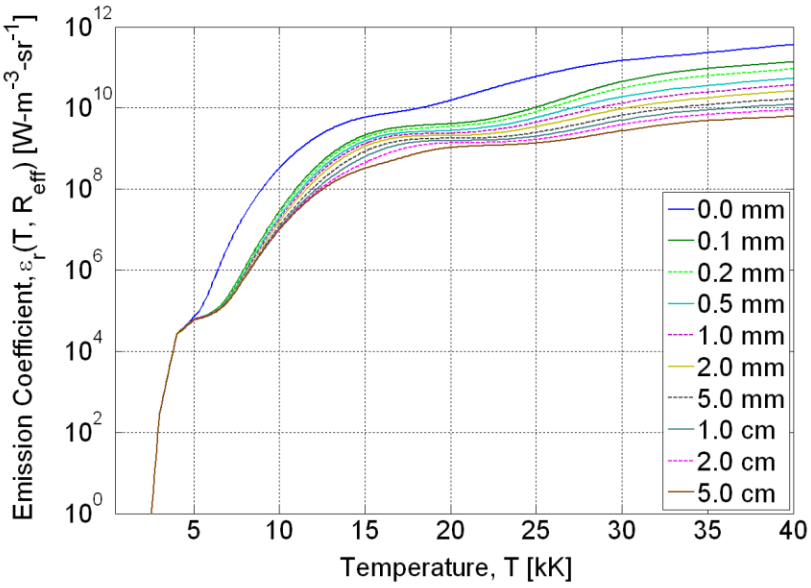

Figure 4.2: Effective net radiative emission coefficient for oxygen as a function of temperature (T) and effective absorption radius (R_{eff}) for 1 atm (Gleizes & Cressault, 2007)

Figure 4.2 shows the net emission coefficient R_{eff} for oxygen plasma as a function of temperature for different effective absorption radii. The data was provided by A. Gleizes and Y. Cressault from the Université Paul Sabatier, France. The "optically thin" assumption corresponds to $R_{eff} = 0.0\ mm$.

Due to the small volume in which the plasma is contained inside a cutting torch, it is reasonable to assume that all emitted radiation leaves the plasma without further re-absorption (i.e. the optically thin assumption). Nevertheless, the two values of the net emission coefficient ($R_{eff} = 0.0\ mm$ (optically thin) and $R_{eff} = 0.5\ mm$) have been used in simulations of the plasma torches to observe the sensitivity of the flow characteristics to the radiation transfer model, as discussed in the next sections.

It also needs to be considered that the calculation of the net emission coefficient depends on the plasma composition, which is not only a function of temperature, but also of pressure. It is reasonable to assume that radiation losses typically increase approximately linearly with pressure. The radiation data provided by Gleizes and Cressault have been calculated for a pressure of 1 atm. The fact that the pressure inside the cutting torch changes drastically (i.e. from 4 atm to 1 atm), the radiation correction is applied in the following manner (Hsu & Pfender, 1983):

$$\frac{Q_1}{Q_2} = \frac{P_1}{P_2} \tag{4.5}$$

Here, Q_1 and Q_2 (W/m^2) are radiation loss terms and P_1 and P_2 are the corresponding pressures.

4.5 Cutting torch energy balance

The total amount of energy lost by radiation per unit time P_r can be calculated according to:

$$P_r = \int_V Q_r \, dV = \int_V 4\pi\varepsilon_r(T_e)dV \tag{4.6}$$

Here, V represents the volume of the spatial domain. The relative importance of the radiation loss with respect to the net energy balance is given by the fraction of energy η_r lost by radiation:

$$\eta_r = \frac{P_r}{P_{in}} = \frac{P_r}{I.\Delta\emptyset} \tag{4.7}$$

where, P_{in} is the input power, I the total current, and $\Delta\Phi$ the total voltage drop across the torch. The values of the quantities P_r, P_{in} and η_r for the two simulations of one

of the 400A torches of Hypertherm (HT4400) are presented in Table 4.2. The radiation loss term in the case of optically thin plasma assumption is greater than that in the case of the plasma with R_{eff} = 0.5 mm assumption owing to the higher emission coefficients in the former case.

The net power loss by radiation represents a very small fraction of the total power input as shown by the results in Table 4.2. In reality, it is observed that the plasma flow fields are heavily dependent on the radiation model used in spite of seemingly contradicting results in the table. There is indeed no contradiction: the precise form of the energy transfer affects drastically the characteristics of the plasma flow. However, due to the small volume of the plasma, the integration of the net emission coefficient over the plasma volume sums up to a very small quantity of power loss when compared with the net amount of power that goes into the plasma. Furthermore, the net energy balance depends on the global conservation of energy, which is not very sensitive to the precise configuration of the plasma flow field (i.e. for the global energy balance what matters are not the profiles of the plasma characteristics, but their integral value).

Table 4.2: Energy balance in a plasma torch

	Effective Absorption Radius	
	R_{eff} = 0.0 mm (optically thin)	**R_{eff} = 0.5 mm**
Total Volumetric Radiation Loss: P_r	$1.41\ kW$	$1.16\ kW$
Power input: P_{in}	$400\ A \times 115\ V = 46.0\ kW$	$400\ A \times 95\ V = 38.0\ kW$
Fraction of power lost by radiation: $\eta_r = P_r/P_{in}$	3.07%	3.05%

Figure 4.3 presents the electron temperature distributions inside the torch as well as the distribution of the net emission coefficient for one of the torches studied (results displayed in later chapters). The net emission coefficient has a marked dependence on the electron temperature. This dependence causes the distribution of net emission coefficient to be highly localized, which limits the extent of the volume V in the expression for total energy lost by radiation given by equation (4.6).

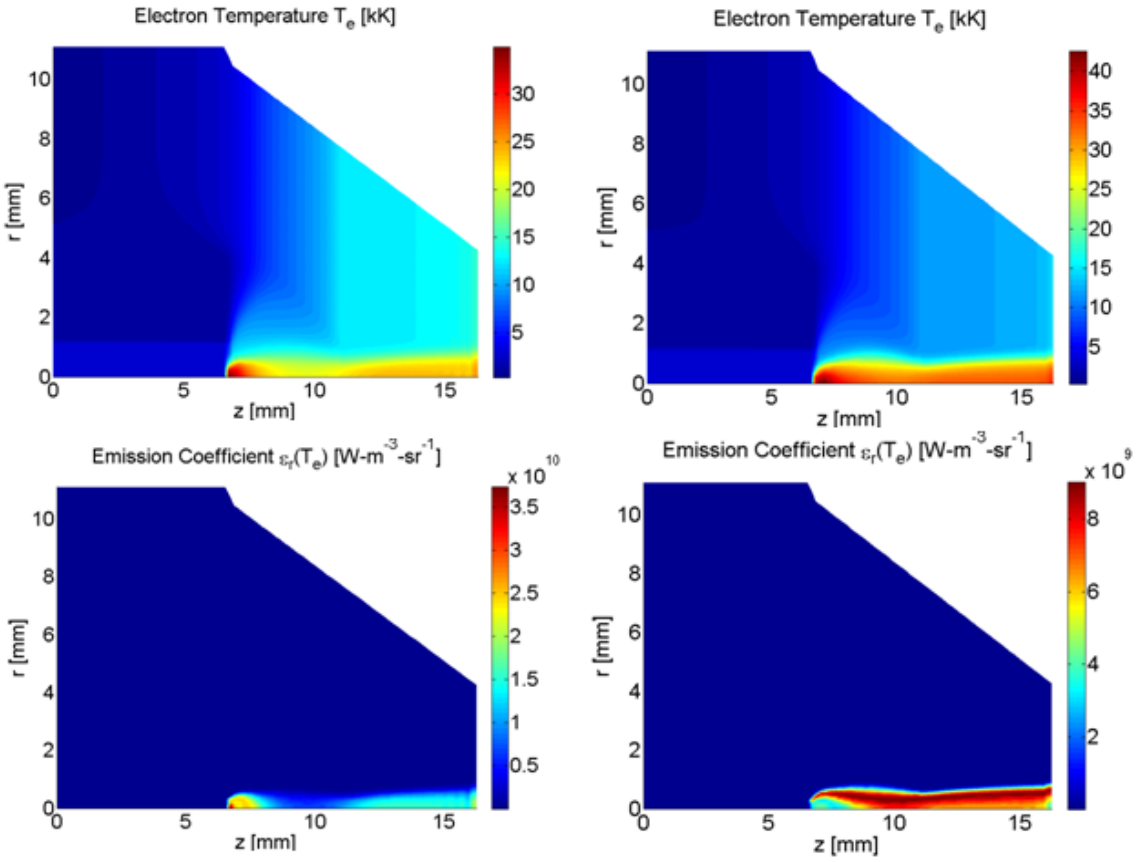

Figure 4.3: Temperature and emission coefficient distribution in the HT4400 torch. *Top row*: electron temperature distributions (*left*, R_{eff} = 0 mm; *right* R_{eff} = 0.5 mm). *Bottom row*: net emission coefficient (*left*, R_{eff} = 0 mm; *right* R_{eff} = 0.5 mm) (Trelles, Heberlein, & Pfender, 2007)

5. EFFECT OF CATHODE CURRENT DENSITY BOUNDARY CONDITION

5.1 Introduction

The model requires a current density profile as one of the boundary conditions. The emitting part of the cathode is a hafnium rod inserted in a copper support. There are different options for determining current density at the cathode surface. One of the alternatives is to use an experimentally measured temperature profile along with the Richardson-Dushman equation (Boulos, Fauchais, & Pfender, 1994).

When a cathode is heated to a sufficiently high temperature, electrons are emitted with a current density j given by the Richardson-Dushman equation:

$$j = AT^2 \exp\left(-\frac{\emptyset_e}{k_B}\frac{e}{T}\right) \tag{5.1}$$

where A is a constant having a value of about $6.0 \times 10^5\ A/m^2K^2$ for most metals, T the surface temperature in Kelvin, ϕ_e the thermionic work function of cathode surface, e the electron charge and k_B Boltzmann's constant. As known from the equation (5.1), the current density of thermionic emission is highly sensitive to the cathode surface temperature. Unless the temperature is increased to a sufficiently high value, it is not possible to reach the current densities which are encountered in the plasma arcs.

This can be clearly seen when the Richardson-Dushman equation is plotted to express the relationship between the electrode surface temperature and the current density emitted from the electrode for various thermionic work functions of the electrode material as shown in Figure 5.1.

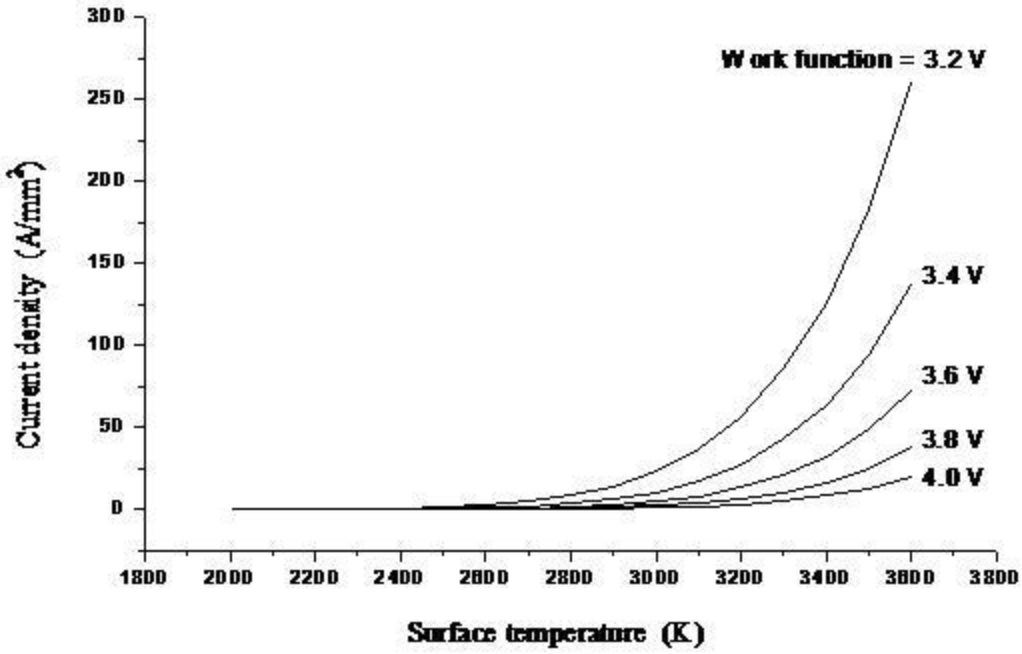

Figure 5.1: Cathode current density vs. electrode temperature for various work functions (Zhou & Heberlein, 1998)

For the high temperature zone, the current density goes up rapidly as the thermionic work function increases. On the contrary, for lower temperatures the curves for different thermionic work functions merge together. For a particular thermionic work function, the current density has the peak value at the maximum electrode temperature and then decays exponentially as the temperature decreases.

5.2 Initial profile used for the simulation

It is not straight forward to evaluate the current density distribution from the Richardson- Dushman equation directly because the thermionic work function of cathode material and the temperature distribution of the electrode surface may not be specified clearly. Hence, another option of using an experimentally determined current density profile seems more convenient.

The initial approach was to assume that the current density distribution on the hafnium insert surface was uniform (Li, Heberlein, & Pfender, 2004):

$$j_0 = \frac{I}{A_c} \tag{5.2}$$

where, I is the arc current and A_c is the area of the hafnium insert frontal surface. Based on experimental measurements, a more realistic profile was used in the modified versions of the code as described in the following sections.

Another approach involving conservation of current is to employ an experimentally observed profile shape in front of the cathode and to adjust its parameters in order to conserve the total current. Current density in the method using Richardson-Dushman equation depends on the assumed temperature over the cathode surface in which computational difficulty in reaching appropriate temperatures may result in inappropriate current densities affecting the ultimate distributions of temperature and other plasma quantities. In the current version of the code, the shape of the current density profile over the cathode surface is derived from a spectroscopic measurement of the temperature in front of the cathode for an arc current of 200A.

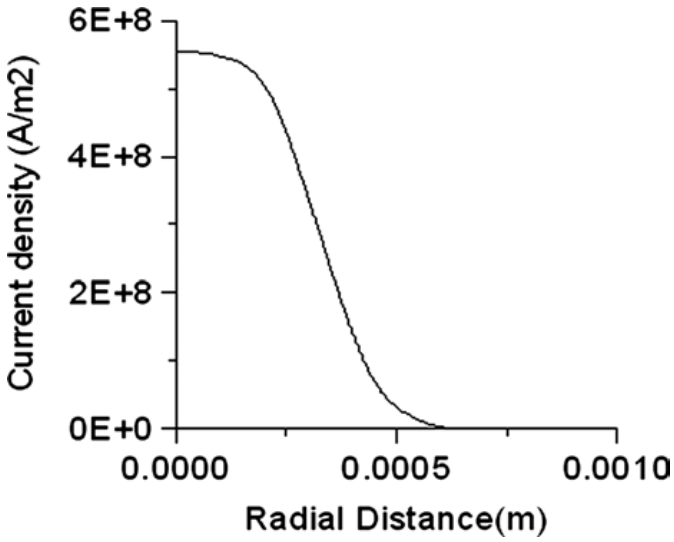

Figure 5.2: Axial current density profile with conservation of total current

(Ghorui, Heberlein, & Pfender, 2007)

An example of current density profile for a 200A arc is shown in Figure 5.2. The radial component of the current density over the cathode surface is assumed to be zero. The profile given in Figure 5.2 is derived from an experimentally determined profile (Zhou & Heberlein, 1998) for tungsten cathode with argon-hydrogen plasma. For our case, the experimentally observed profiles were approximated by an algebraic expression which when integrated over the hafnium radius conserved the total current.

5.3 Effect of current density boundary condition at cathode

The current density distribution plays a huge role in the realized temperature distribution. In practice, a converged solution could be obtained for any current density by specifying an appropriate grid distribution. Improper grid density in the nozzle section makes the code diverge as the $j \times B$ constriction tears apart the flow.

This problem becomes severe with higher j which is the case for 400A torches. Due to the scarcity of available experimental data related to current density profiles at the cathode for 400A torches, different profiles were tried as boundary conditions in the simulation. The axial current density profiles were obtained conserving the total current of 400A while maintaining a similar profile shape as that for a 200A torch. The radial component of the current density over the cathode surface is assumed to be zero. The results are presented later.

The current density profile over the cathode as described above is given by the equation $J = J_0 e^{-\left(\frac{cr}{R}\right)^3}$, where c is a constant which determines the width of the profile (Ghorui, Heberlein, & Pfender, 2007). J_0 and R are the maximum current density at the center and the radius of the hafnium insert respectively. The value of c used for HT2000 torch simulation was 2.8. Figure 5.3 is a plot of a range of profiles used in the simulation.

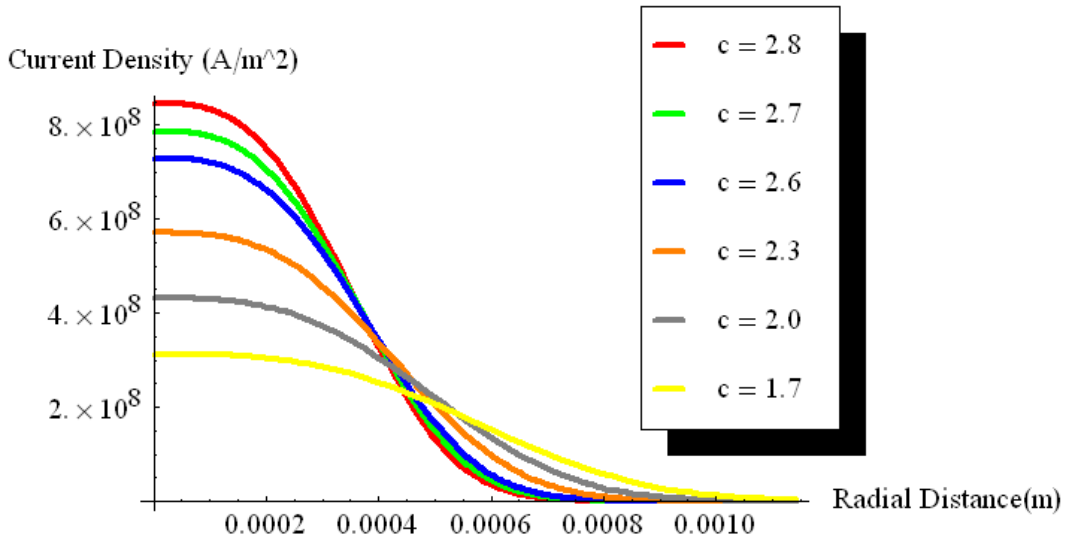

Figure 5.3: Various axial current density profiles used as boundary condition at cathode

where c is constant in equation for profiles given by $J = J_0 e^{-\left(\frac{cr}{R}\right)^3}$

5.4 Simulation results with various current densities for R_{eff} = 0.5 mm

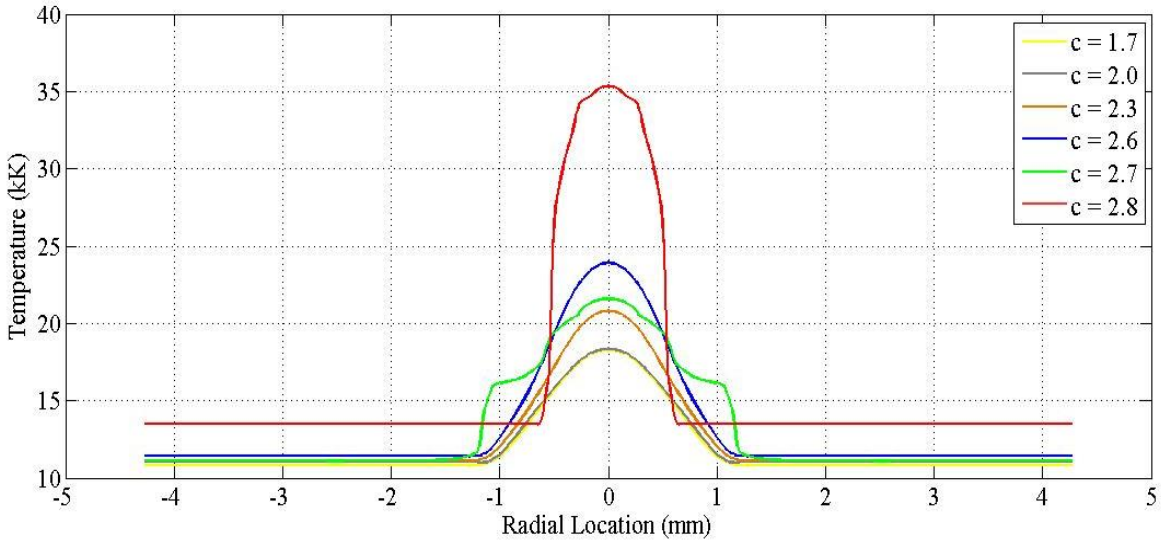

Figure 5.4: Temperature profiles at the nozzle exit in HT4400 torch for the current density profiles given in Figure 5.3

Figure 5.4 shows the corresponding nozzle exit temperatures for the profiles given in Figure 5.3. As expected, the peak temperatures are higher for narrower current density profiles at the cathode. Although a converged solution was obtained for the narrowest profile (c = 2.8), the maximum temperatures inside the torch are unrealistically high. Such high temperatures would imply strong radiation that could not be sustained by the power input to the torch. These exceedingly high temperatures indicate the necessity of using $R_{eff} = 0.0\ mm$ (optically thin plasma assumption) for this profile.

Simulation of HT4400 torch with different current density profiles at the cathode suggests that this boundary condition plays an important role in determining the plasma solution fields. This also emphasizes the need for experimental data to validate the used current density boundary condition specified at the cathode for a 400A cutting torch.

Table 5.1 summarizes the simulation results for various combinations of current density profiles and effective radii of radiation in the HT2000 and HT4400 torches.

Figure 5.4 and Table 5.1 indicate a discrepancy in the results for $c = 2.7$ which might be because of the grid sensitivity of the code. In Table 5.1, as the value of c in the equation for the cathode current density profile increases, that is the current density profile becomes narrower, higher peak temperatures at the cathode and the nozzle exit are observed. The disagreement with the stated observation, of the results for $c = 2.7$ could be explained as follows. The NEQ plasma code is highly grid sensitive. Every simulation of the code needs an optimized grid in order to get converged results. The simulations with different current density boundary conditions required different grids optimized for every current density profile used. It was observed that the flat zones in the exit temperature profile for $c = 2.7$ in Figure 5.4 were due to changed grid density in that

zone. Nevertheless, any attempt to correct this fact resulted in diverging solution for the particular current density profile.

Table 5.1: Peak temperatures with various cathode current densities and radiation models

Torch	**Effective Absorption Radius (mm)**	**Constant "c" in Current Density Profile Equation Given by $J = J_0 e^{-\left(\frac{cr}{R}\right)^3}$**	**Peak Temperature at Cathode (K)**	**Peak Temperature at Nozzle Exit (K)**
HT2000 (200A)	**0.5**	**2.8**	**28000**	**27500**
	0.0	**2.8**	**24000**	**22900**
HT4400 (400A)	**0.5**	**1.7**	**22000**	**18300**
		2.0	**24000**	**18400**
		2.3	**28000**	**20800**
		2.6	**32000**	**23900**
		2.7	**30000**	**21600**
		2.8	**60000**	**35300**
	0.0	**2.8**	**36000**	**22900**

The temperature distributions for the set [c = 2.8, R_{eff} = *0.0 mm*] and [c = 2.6, R_{eff} = *0.5 mm*] are comparable and hence it is worth checking the simulation results with an intermediate effective absorption radius. This might give the most accurate radiation energy loss model to obtain physically sound results of the non-equilibrium modeling of thermal plasma flows in plasma cutting torches.

6. RESULTS AND DISCUSSION

6.1 Simulation of HT2000 200A O_2/Air cutting torch

6.1.1 About the torch (www.hypertherm.com, 2009)

A section of HT2000 torch along its axis is shown in Figure 6.1. The dimensions and other parameters for the grid generation are obtained on the basis of this drawing.

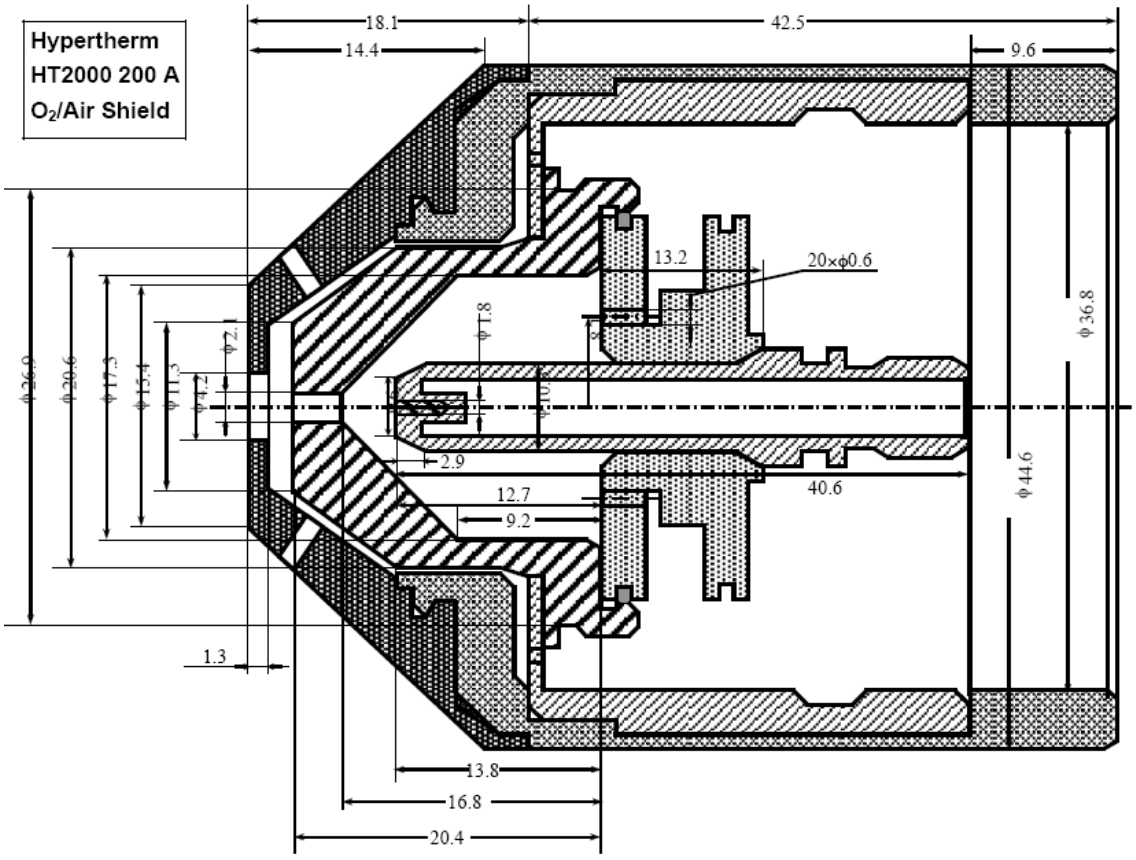

Figure 6.1: Schematic of HT2000 torch (dimensions in mm) (Li, Heberlein, & Pfender, 2005)

In the schematic diagram of the Hypertherm HT2000 200A O_2/Air plasma cutting torch shown in Figure 6.1, the geometrical sizes are based on the drawings of the product and the object measurements. The emitting part of the cathode is hafnium, while the supporting part is copper. The nozzle and the shielding part are also made of copper.

6.1.2 Process parameters

The actual simulation domain used for the modeling is shown in Figure 6.2. The shaded portions represent the solid parts whereas the un-shaded ones correspond to the fluid domain.

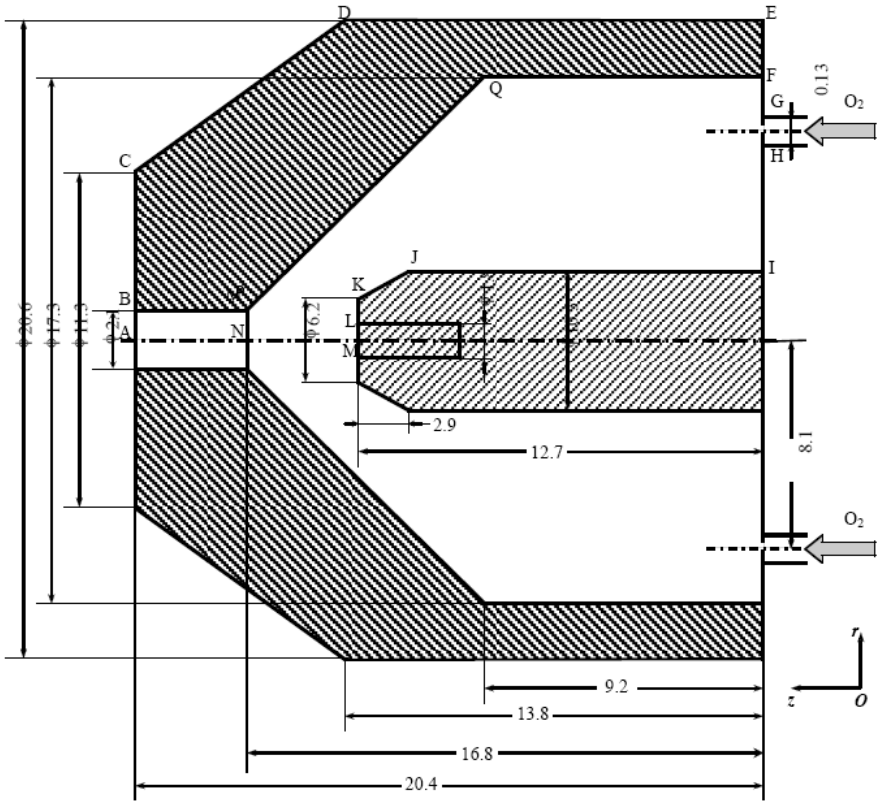

Figure 6.2: Simulation domain (dimensions in mm) (Li, Heberlein, & Pfender, 2005)

Table 6.1: Steady state process parameters and torch specifications (200A torch)

Flow rate of O_2	$1.43179 \times 10^{-4}\ m^3/s$ **(**79.6 scfh)
Plasma plenum pressure	480280.5 Pa (54.96 psig)
Torch current	200A
Swirl injection type	Axial
Swirl angle	20°
Number of swirl injection holes	20
Diameter of swirl injection holes	0.635 mm (0.025")

Table 6.1 illustrates a few important process parameters and specifications of the HT2000 torch. Corresponding code parameters are given in Table 6.2. These parameters are specified in the USER.f file.

Table 6.2: Steady state parameters converted to code parameters (200A torch)

TCRN	200 (A)
TAND	600 (K)
TIN	300 (K)
UIN	21.2416 (m/s)
WIN	7.7313 (m/s)
PRSIN	480280.5 (Pa)

In Table 6.2, TCRN denotes the total torch current, TAND is the nozzle wall temperature, and TIN, UIN, WIN and PRSIN denote the inlet- temperature, axial velocity, tangential velocity and pressure respectively. The velocities are calculated from the flow rate as described in the following section.

6.1.3 Input velocity calculations from inlet flow rate

The inlet velocity components to be specified in USER.f subroutine are calculated from the flow rate specification as follows. The flow rate in $scfh$ (standard cubic feet per hour) is first converted to a flow rate in m^3/s using the inlet pressure and temperature using the ideal gas law. The velocity (m/s) is calculated from the flow rate in m^3/s by division by the area of inlet.

$$Flow\ rate = 79.6\ scfh$$

$$Inlet\ pressure = 54.96\ psig = 480280.5\ Pa$$

$$Inlet\ temperature = 300\ K$$

Converting standard flow rate for inlet conditions using ideal gas law:

$$\frac{p_1 \dot{v}_1}{T_1} = \frac{p_2 \dot{v}_2}{T_2}$$

$$\frac{100000 \times 79.6}{273.15} = \frac{480280.5 \times \dot{v}_2}{300}$$

$$\dot{v}_2 = 18.20279\ ft^3/hr = 1.43179 \times 10^{-4}\ m^3/s$$

Area of inlet:

$$A = 20 \times \left(\pi/4\right) \times (0.025 \times 0.0254)^2 = 6.334 \times 10^{-6}\ m^2$$

$$Total\ velocity = \frac{1.43179 \times 10^{-4}}{6.334 \times 10^{-6}}$$

$$= 22.6048\ m/s$$

$$UIN = 21.2416\ m/s$$

$$WIN = 7.7313\ m/s$$

Now, the dimension of the inlet zone needs to be calculated in order to be specified in the grid generation subroutine. This dimension is the width of the annulus with its area equal to the total area of the swirl injection holes.

Dimensions of inlet zone:

$$A_a = \frac{A_c}{\cos 20} = \frac{6.334 \times 10^{-6}}{0.9396926}$$

$$A_a = 2\pi r d_A = 2\pi \times 0.245 \times d_A$$

$$d_A = 0.00638"$$

6.1.4 Generated Grid

The grid generated by the modified grid generator is shown in Figure 6.3.

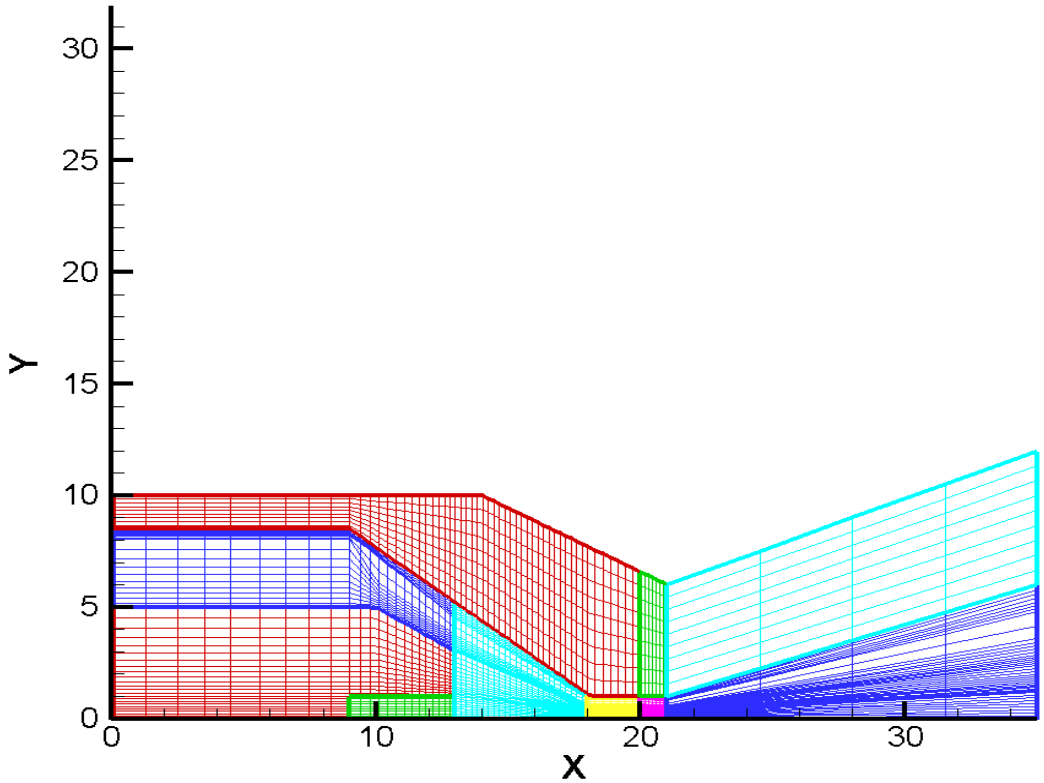

Figure 6.3: Mesh for HT2000 torch

6.1.5 Initial simulation results

The validity of the results of FAST-2D when compiled with the modified version of the grid generator and radiation model based on the data by Gleizes *et al* with optically thin assumption; using Intel Fortran Compiler version 10 has been tested by re-running the simulation of the cutting torch HT2000 operating with pure oxygen and a total current 200A (HT2000 200A O_2). Figure 6.3 shows the computational mesh used to discretize the solid and fluid domains of the inside of the torch HT2000.

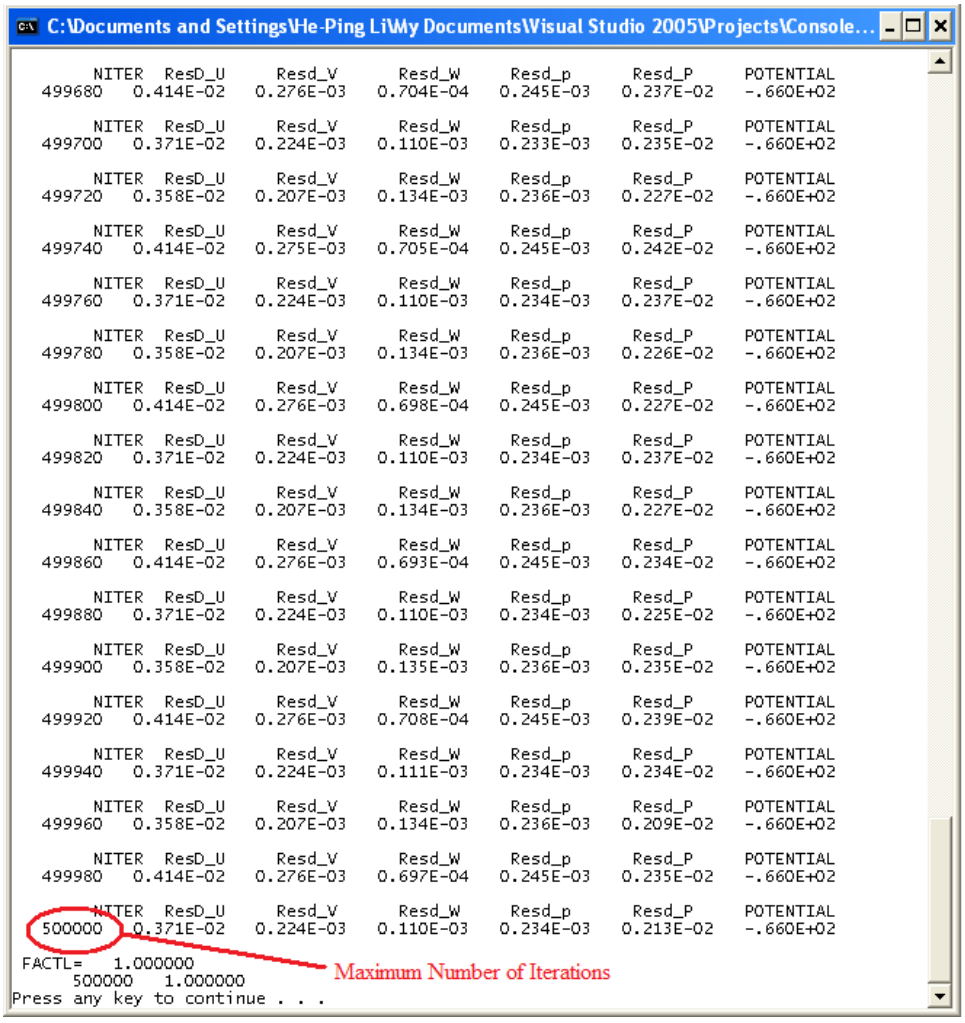

Figure 6.4 Command window showing convergence of FAST-2D for simulation of HT2000 200A O_2/Air cutting plasma torch

Figure 6.4 shows a part of the output from the command window from the NEQ (Non-Equilibrium) simulation displaying the completion of the total number of iterations set by the user. Convergence of the solution was tracked from the residuals displayed in the command window and from animations of the results. The residuals shown in Figure 6.4 are calculated according to the procedures described in the FAST-2D report (Zhu, 1991). These residuals when plotted against iteration number are shown in Figure 6.5. This plot shows that the residuals become steady after about 365000 iterations and hence the simulation could be said to be converged.

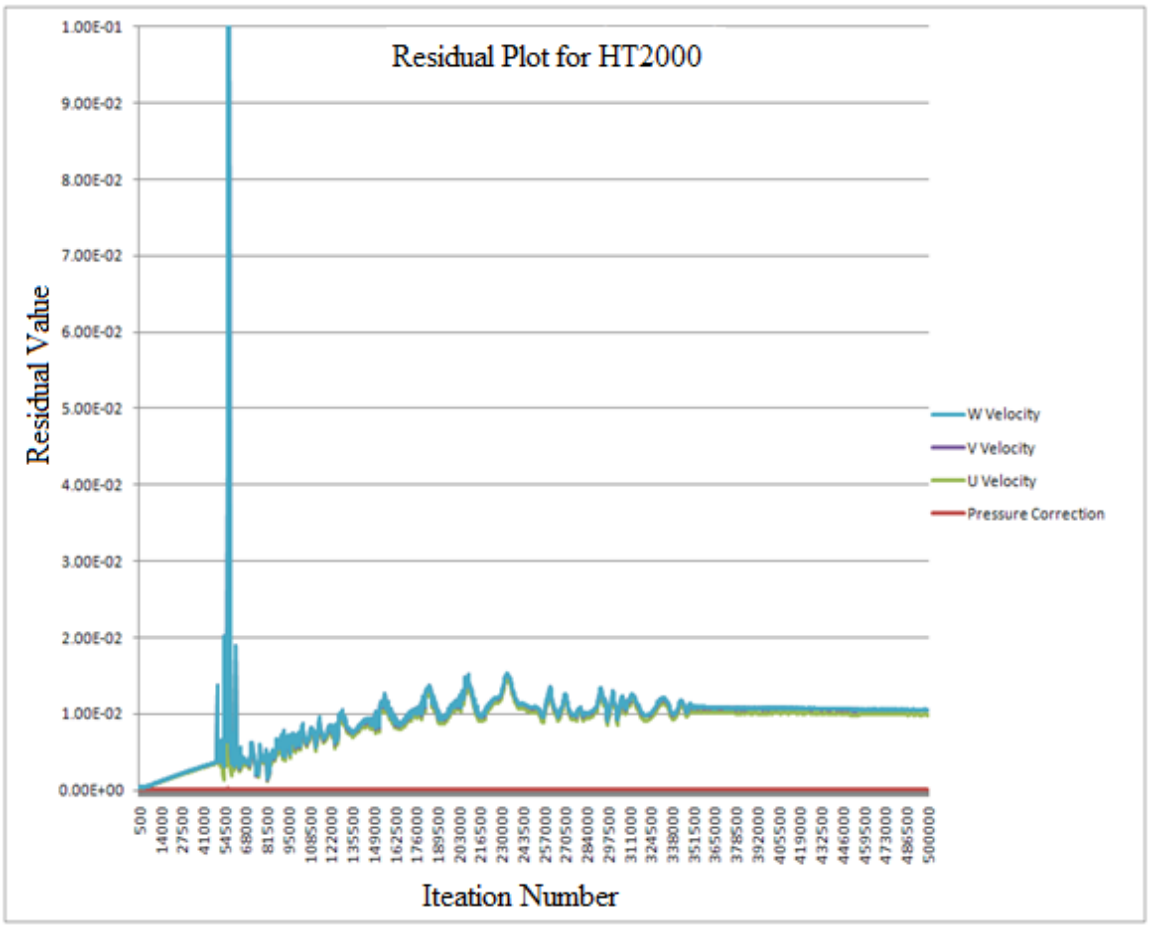

Figure 6.5: Residual plot for HT2000 torch

Figure 6.6 shows the electron and heavy-particle temperature distributions. The upper half of the plot represents the electron temperature distribution and the lower half is the heavy-particle temperature distribution. A wide difference in the distributions of electron and heavy-particle temperatures inside the torch is clearly visible from the plot. The fact that the heavy-particle temperature drops sharply near the wall prevents it from melting. On the other hand, though the electron temperature remains high near the nozzle walls, it is thermally isolated from the walls due to zero temperature gradient at the walls. Both the temperatures first show an increase near the cathode, followed by a decrease and then again an increase in the nozzle bore.

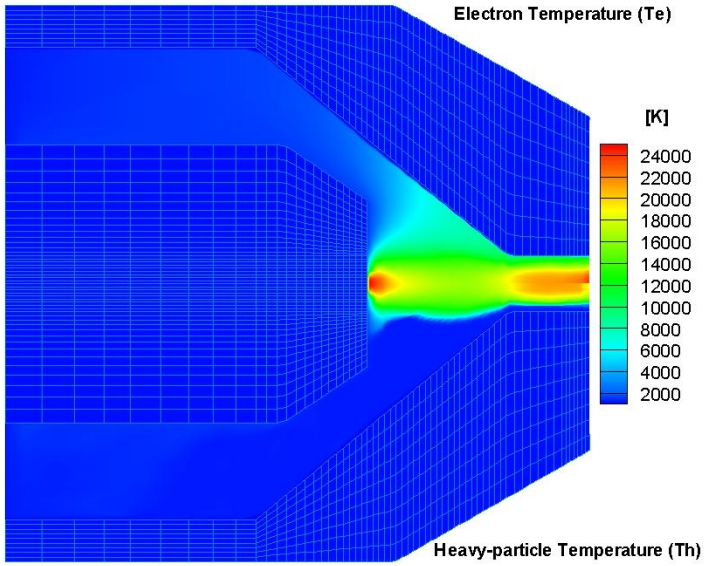

Figure 6.6: Results of simulation of HT2000 O_2/Air 200A plasma torch (*upper half*) electron temperature distribution and (*lower half*) heavy-particle temperature distribution

The maximum temperatures of ~ 24000 K inside the torch compare with the maximum temperatures of ~ 28000 K presented in the simulation results by Ghorui *et al*. The fact that the new radiation data is almost an order of magnitude greater than the data used in the earlier simulations seems to have a major effect on the predicted temperature surrounding the plasma column, which enhances the constriction of the plasma flow. The larger values of the new volumetric radiation losses predict a stronger radiative cooling of the arc than what was previously predicted. The stronger cooling of the arc causes the constriction of the arc observed above (Figure 6.6) and also limits the values of the temperatures inside the torch.

Figure 6.7 shows the temperature profile at the nozzle exit for the HT 2000 torch. As expected, the highest temperatures are obtained on the torch axis.

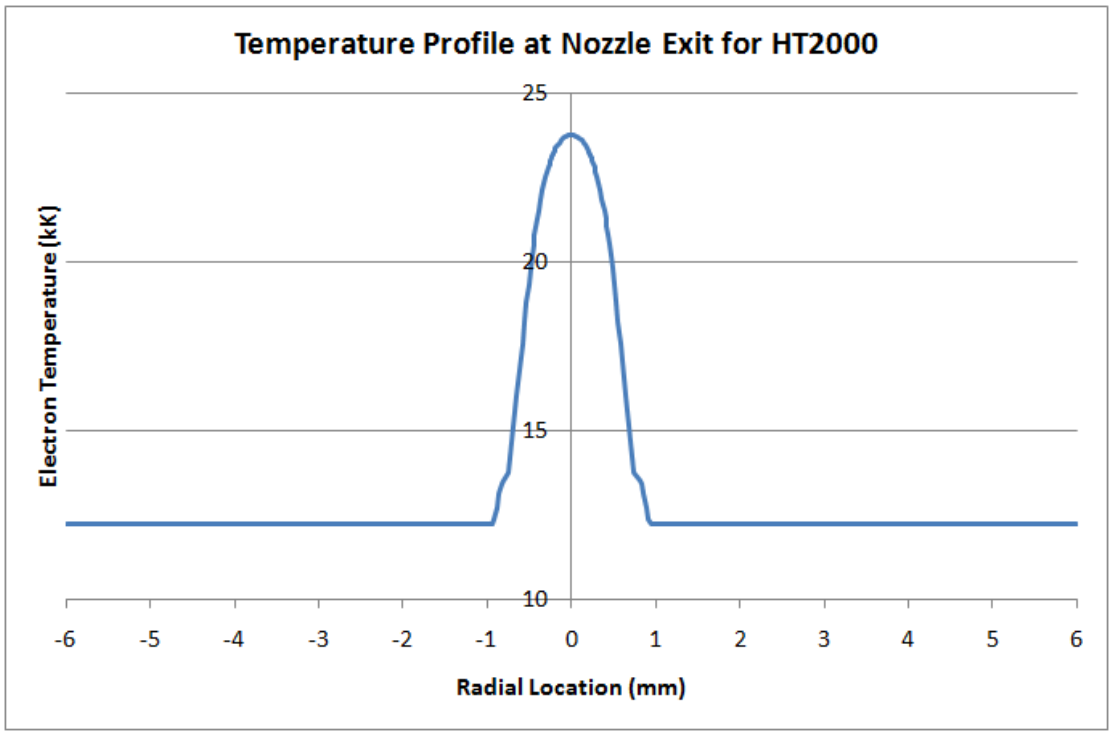

Figure 6.7: Temperature profile at the nozzle exit in HT2000 torch

The velocity distribution in the torch is shown in Figure 6.8. The streaks in the velocity plot are due to the uneven nature of the grid and could be eliminated with the refinement of the grid as demonstrated in the following sections of this chapter.

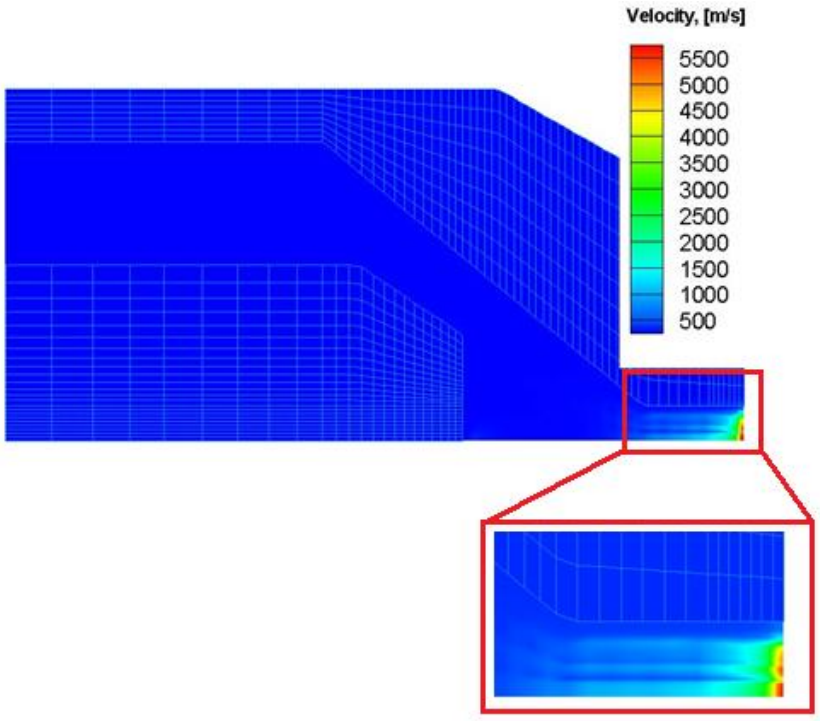

Figure 6.8: Velocity distributions in HT2000 torch

The axial velocity profile plot at the nozzle exit shown in Figure 6.9 gives emphasis on the unphysical off-axis peaks due to the uneven grid.

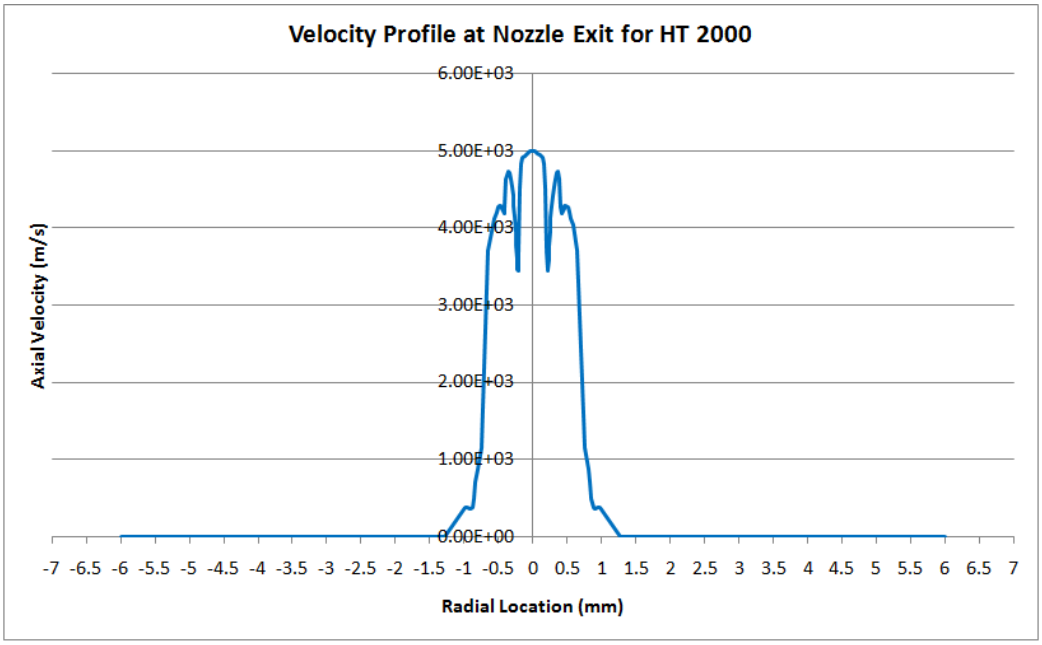

Figure 6.9: Axial velocity profile at nozzle exit in HT2000 torch showing off-axis peaks

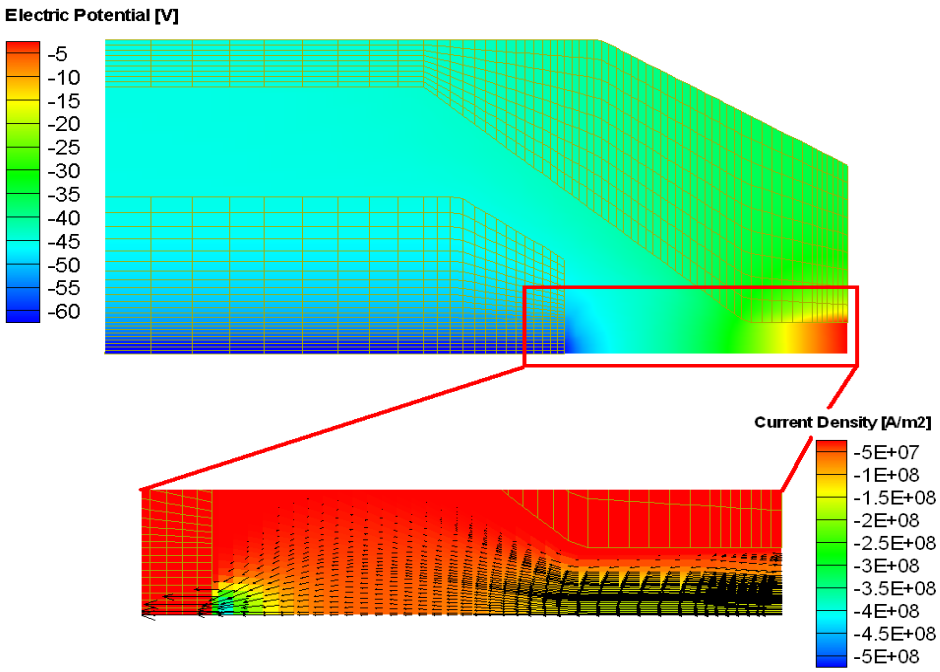

Figure 6.10: Electrical characteristics of HT2000: (*top*) electric potential distribution and (*bottom*) distribution of axial current density in the region in front of the cathode.

Figure 6.10 presents the distribution of electric potential and current density in the axial direction in the region in front of the cathode. The computational total voltage drop of ~ 65 V is comparable to the voltage drop obtained experimentally (equal to ~ 63 V).

In the vector plot of the current density as shown in Figure 6.10, the current distribution is constricted by the cold gas boundary layer along the wall, with the maximum constriction near the upstream end of the nozzle bore. As the current density obeys the conservation of current, the highest density is observed in this region as compared to the region near the cathode where the arc can find more space to expand. The heat generation mechanism of a plasma torch is by Joule heating. Hence, the temperature distribution follows the current density distribution.

6.2 Variations in simulation

6.2.1 Effect of radiation

It has been observed while running the plasma torch simulations that the radiation model has a significant effect on the distribution of the plasma field quantities and therefore it is required to select an adequate radiation model in order to produce reasonable results. As the experimental determination of the correct effective radius of radiation is very difficult, it is only fair to run the simulation with different radii of radiation to observe their effect. Identical simulation parameters were used to run the simulation with two different radiation models (with effective absorption radius R_{eff} = 0.5 mm and 0.0 mm) and the simulation was run for a maximum of 500000 iterations.

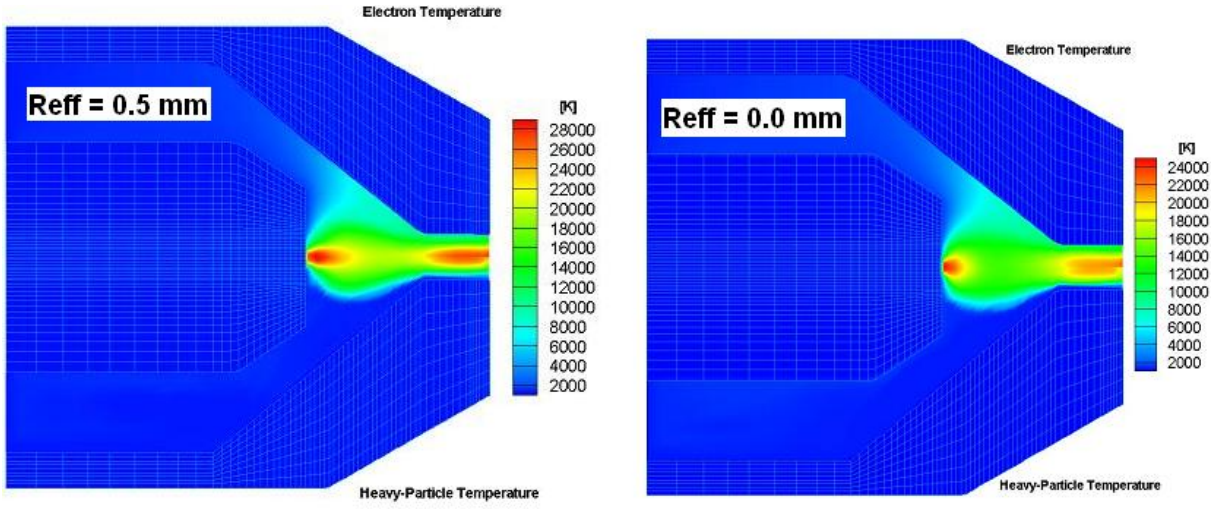

Figure 6.11: Electron and heavy-particle temperature distributions in HT2000 torch:

(*left*) R_{eff} = 0.5 mm (*right*) R_{eff} = 0.0 mm

Figure 6.11 shows the comparison of the converged results obtained with R_{eff} = 0.5 mm and R_{eff} = 0.0 mm, showing a difference of 4000 K in the peak temperatures.

Figure 6.12 compares the distributions of the axial velocities inside the HT2000 torch, where the difference between the peak velocities is about 2000 m/s. The electric potential and the current density distributions are not appreciably different for the two effective absorption radii.

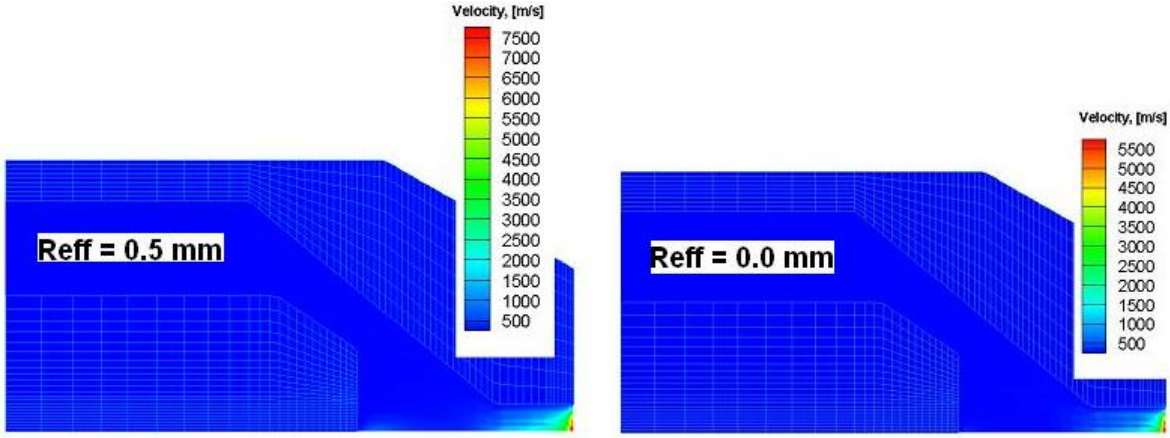

Figure 6.12: Velocity plots in HT2000 torch: (*left*) R_{eff} = 0.5 mm (*right*) R_{eff} = 0.0 mm

Figure 6.13 shows the temperature distribution in the radial direction at the nozzle exit section. The peak temperature for the simulation with the effective radius of 0.5 mm is 27325 K whereas that with the effective radius of 0.0 mm is 22940 K.

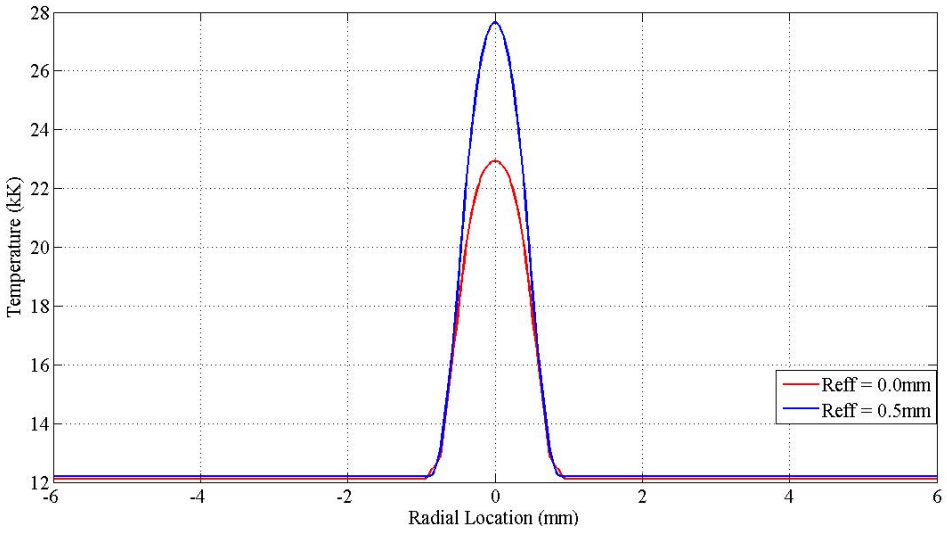

Figure 6.13: Radial temperature profiles at the nozzle exit in HT2000 torch

The studies performed indicate that the nozzle exit peak temperatures in case of R_{eff} = 0.0 mm are 2000 K lower than the experimentally measured ones, whereas those in case of the larger R_{eff} are 2000 K higher.

6.2.2 Solution for off-axis velocity peaks

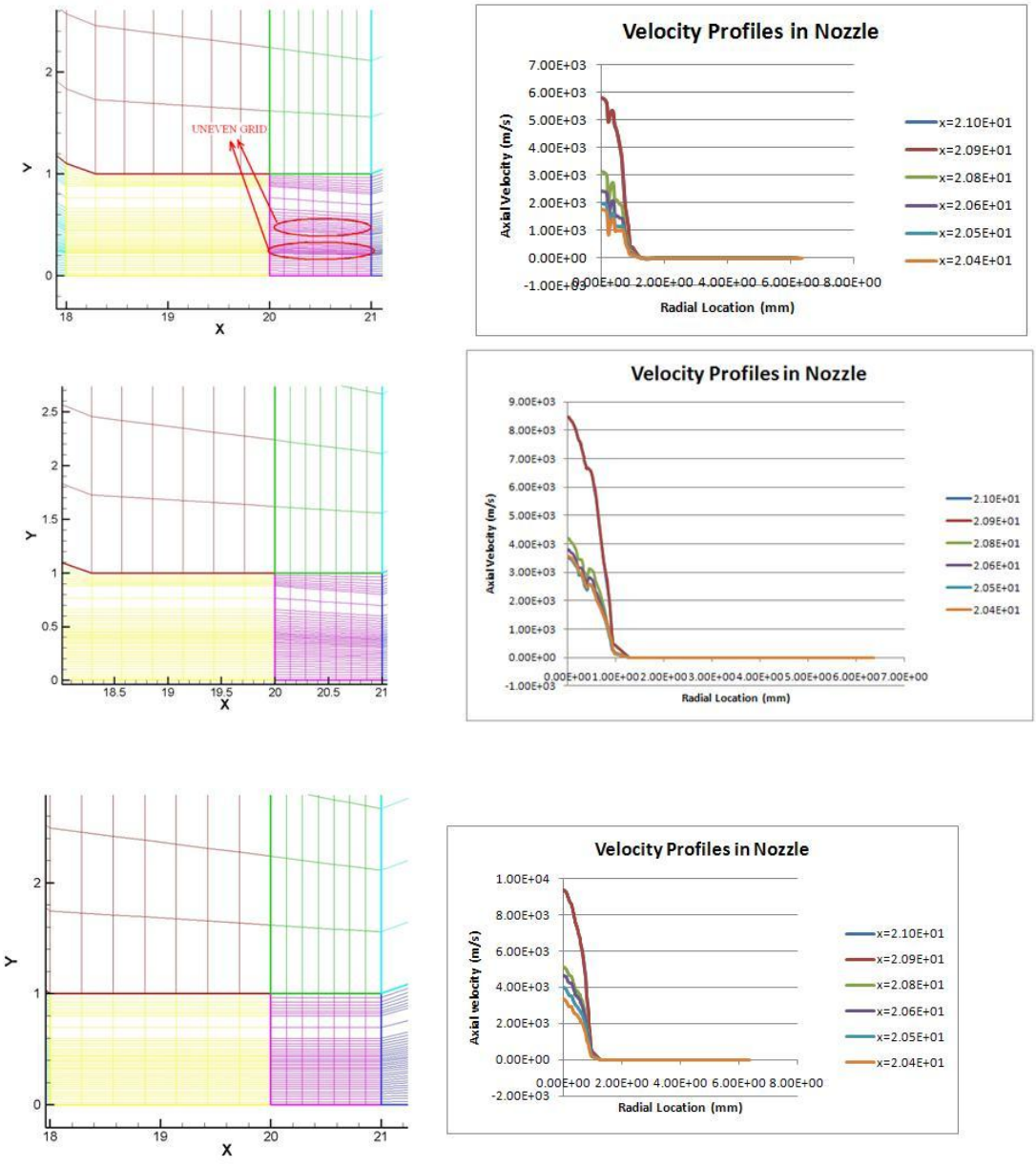

Figure 6.14: Elimination of off-axis peaks by grid refining

As discussed earlier in this chapter the off-axis peaks in the near-exit velocity profiles are coupled with smoothness of the grid and can be eliminated by adjusting the grid which is performed as above in Figure 6.14. The grid density distribution in the first part of the figure is considerably uneven. As the results of NEQ code are highly grid dependent, this unevenness causes the velocity profile show off-axis peaks at the locations of abrupt grid density changes. The second part of Figure 6.14 shows a grid with better density transition as compared to the grid shown in the first part. Therefore, it results into less prominent off-axis peaks. The third grid shown in Figure 6.14 gives the best results by almost eliminating the off-axis peaks. The results with this grid are the closest to the results obtained by Ghorui *et al*.

6.2.3 Swirl velocity boundary condition correction

The plot of swirl velocity for the HT2000 torch given in Figure 6.15 showed unrealistically high swirl velocities. The expected value of the swirl velocity at any location would be in a much lower range as compared to the highest of 900 m/s (magnitude wise) obtained in the distribution plot.

As evident from the plot, the highest values of swirl velocities are near the inlet zone which makes one suspect the correctness of the inlet boundary conditions for the swirl velocity. The following flaw was noticed in the boundary condition subroutine (BOUNDS.f).

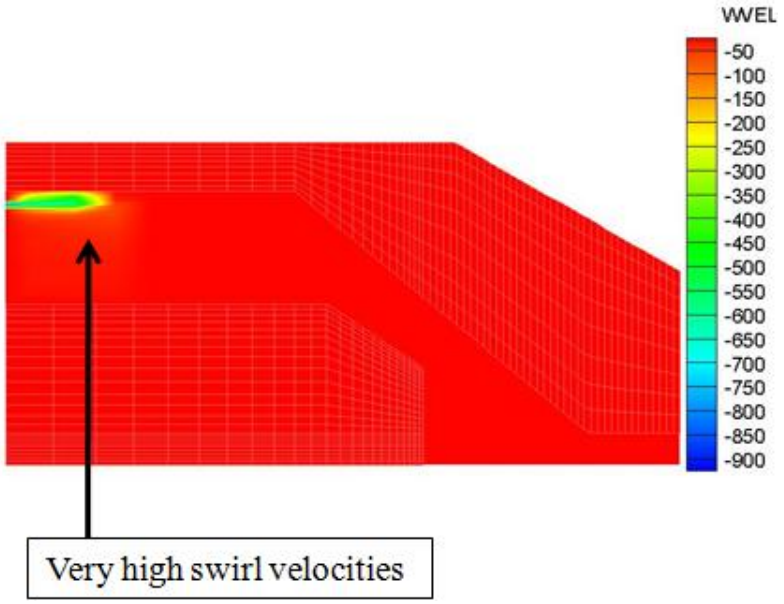

Figure 6.15: Swirl velocity w m/s in HT2000 torch

The code solves w.r momentum equation for the swirl velocity w. It was observed that the value of w_{in} (inlet swirl velocity) was given as a boundary condition at the inlet for w.r equation which is not correct. Figure 6.16 shows the part of BOUNDS.f subroutine where the above mentioned boundary condition is specified. The expression inside the highlighted box shows that the value of inlet swirl velocity is assigned as the boundary condition for the w.r momentum equation.

```
      DO J=1,NJ
C-----1. THE LEFT BOUNDARY
        I=1
        II=I+(J-1)*NI
        IF(J.EQ.NY1+NY2+NY3-5) THEN
          TEMP=TAN(20.*PAI/180.)*F(ISU+II)
           F(ISWR+II)=-TEMP
        ELSE
          F(ISWR+II)=0.
        END IF
```

Figure 6.16: Incorrect w.r inlet boundary condition

The correct version of the inlet boundary condition is as follows

```
      DO J=1,NJ
C-----1. THE LEFT BOUNDARY
        I=1
        II=I+(J-1)*NI
        IF(J.EQ.NY1+NY2+NY3-5) THEN
          TEMP=TAN(20.*PAI/180.)*F(ISU+II)
            F(ISWR+II)=-TEMP*F(ISR+II)
        ELSE
          F(ISWR+II)=0.
        END IF
```

Figure 6.17: Correct w.r inlet boundary condition

Other places in the code where the corrections are required are:

a) In the source term for v-momentum equation ($\rho \frac{v_\theta^2}{r}$)

b) In the total velocity calculation $\sqrt{v_z^2 + v_r^2 + v_\theta^2}$

Figure 6.18 shows the plot of swirl velocity after making desirable changes in the code.

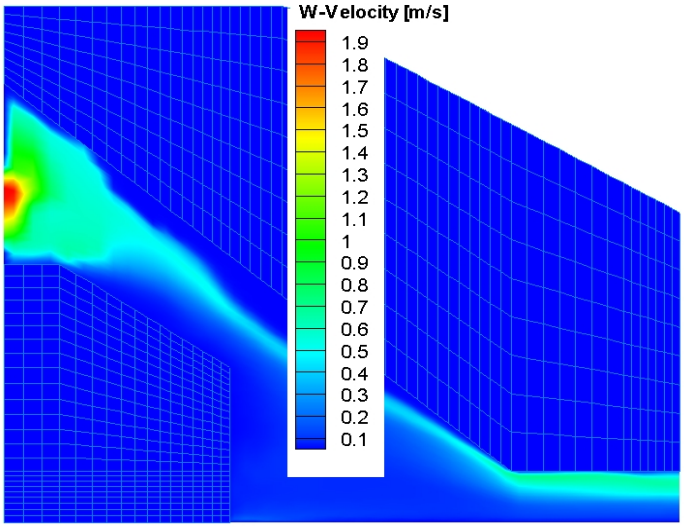

Figure 6.18: Swirl velocity (w m/s) plot with corrected boundary conditions

6.2.4 Simulation with input velocity profile

One of the concerns with the simulations is the ability to input the actual swirl injection. The three dimensional geometry of the swirl injection ring cannot be simulated in the present code because of its two dimensional nature. The swirl injection ring is approximated by an annulus with an area equal to the cross sectional areas of the swirl injection holes added together. As mentioned earlier in the grid generation section, there is an injection zone provided in the 2-D simulation domain which actually represents an annular region due to the axi-symmetric nature of the domain. This representation is considerably different from the actual swirl injection geometry.

Therefore commercial CFD software CFDesign was used to simulate the actual three dimensional torch geometry with a cold flow, and inlet velocity component profiles were extracted at some distance downstream of the swirl ring location. A sample section of the 3-D simulation domain is shown in Figure 6.19. The location at which the inlet velocity component profiles are extracted is marked with a black line. The domain for plasma simulation starts at this section. Hence another advantage of using a CFDesign simulation to determine the inlet velocity profile is a smaller working domain for the plasma simulation, enabling the use of a finer grid given the limitation on the total number of grid-points in each direction.

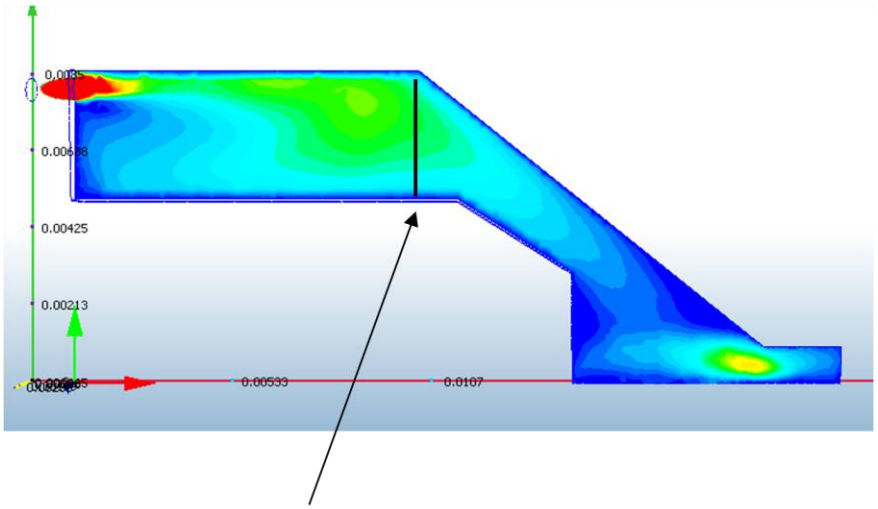

Figure 6.19: A sample section of torch from CFDesign simulation

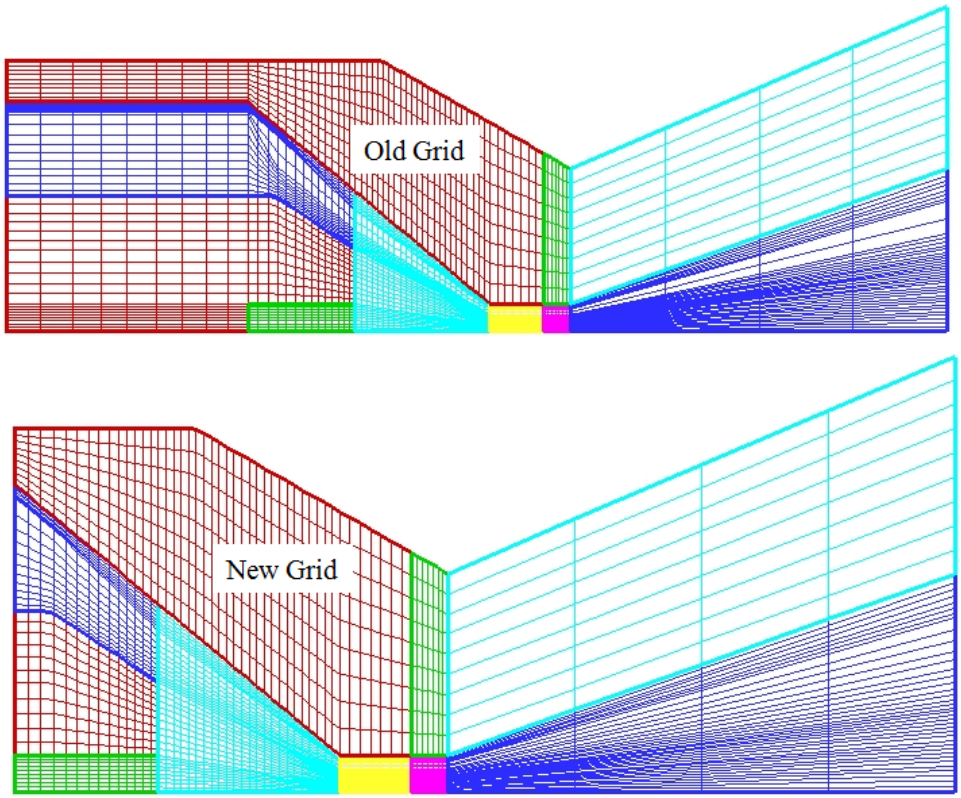

Figure 6.20:Comparison of grids for original simulation and simulation with inlet velocity profile

The modified domain for the plasma simulation is shown in Figure 6.20. As it is evident from the diagram, this domain is considerably smaller than the original working domain.

The input velocity components for the code, obtained as the output of the CFDesign simulation are plotted in Figure 6.21.

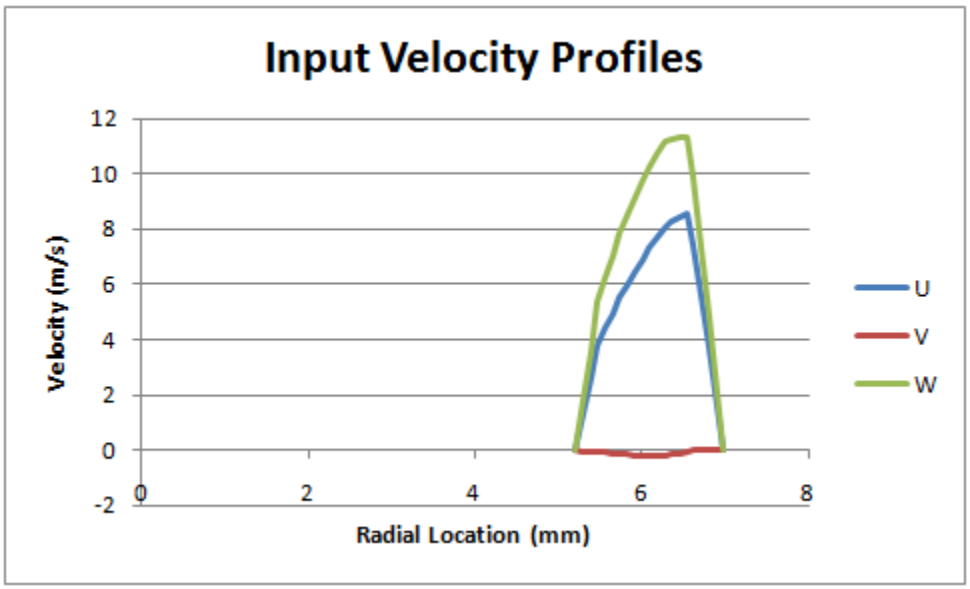

Figure 6.21: Input velocity profiles for the plasma simulation

The results obtained with the above mentioned set-up were comparable to earlier results as shown in Figures 6.22, 6.23, 6.24 and 6.25. Hence, using a cold-flow simulation derived velocity profile at the inlet is a valid improvement in the code. As this modification was implemented with the old radiation model, the results are comparable to the results obtained by Ghorui *et al*.

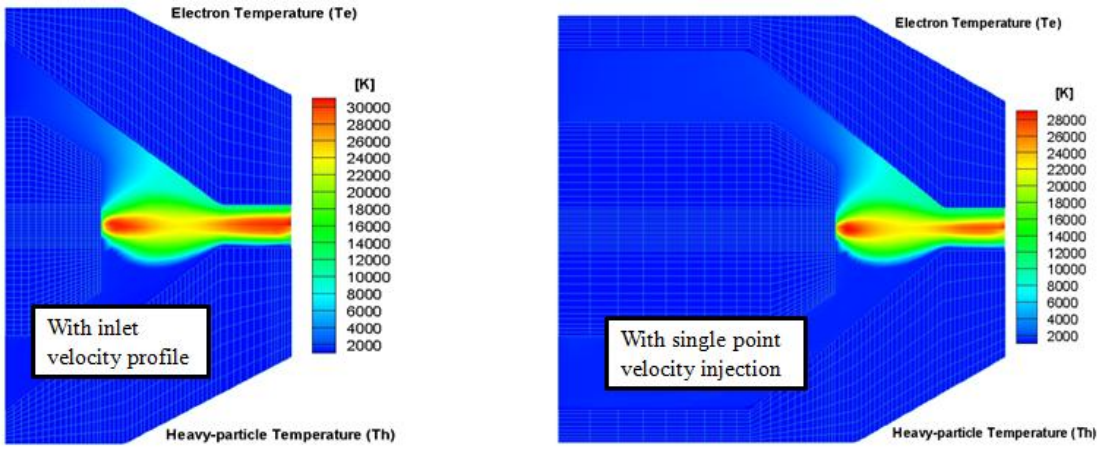

Figure 6.22: Comparison of temperature plots for simulation with inlet velocity profile and simulation with single point velocity injection

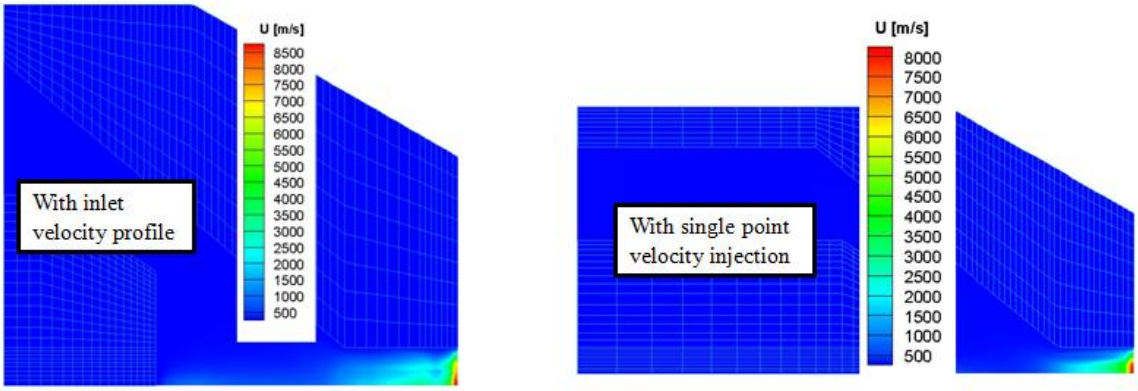

Figure 6.23: Comparison of velocity plots for simulation with inlet velocity profile and simulation with single point velocity injection

The various plasma field quantities' plots with inlet velocity profile input are very similar to corresponding plots with single point velocity injection as shown in Figures 6.22, 6.23, 6.24 and 6.25. The differences in maximum temperatures and velocities obtained by the simulations are not very significant and may be justified by the grid

sensitivity of the code. The grids for the two simulations are significantly different. The simulation domain for the input velocity profile case is much smaller as compared to the one for the other case in consideration. Also, the variation might have been introduced by the software CFDesign used for cold flow simulation.

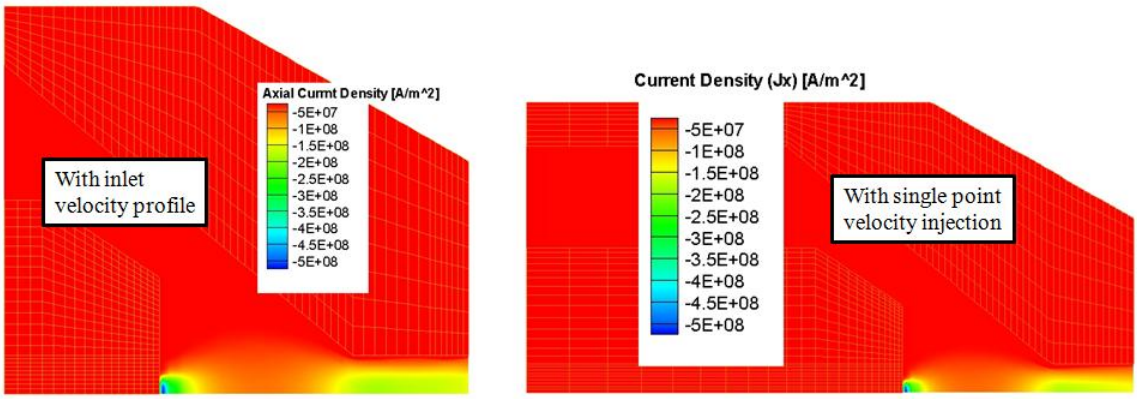

Figure 6.24: Comparison of axial current density plots for simulation with inlet velocity profile and simulation with single point velocity injection

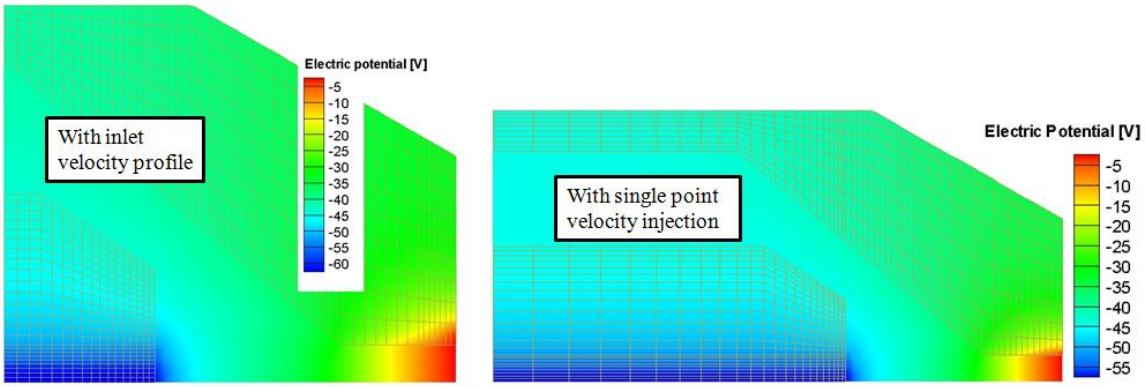

Figure 6.25: Comparison of electric potential plots for simulation with inlet velocity profile and simulation with single point velocity injection

6.2.5 T_e / T_h ratio issue

The degree of non-equilibrium in a plasma torch simulation is quantified by the ratio of the electron temperature to the heavy-particle temperature. This degree of non-equilibrium also plays an important role in determining the thermodynamic and transport properties of the plasma. The present version of the code has properties for the oxygen plasma with the degree of non-equilibrium up to $\frac{T_e}{T_h} = 20$ beyond which the properties get clipped as shown in Figure 6.26.

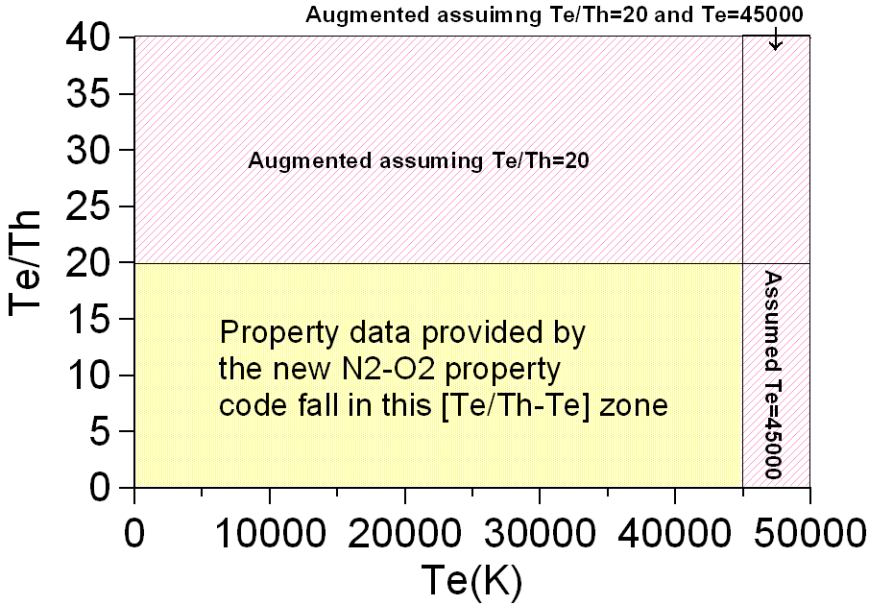

Figure 6.26: Augmentation of properties beyond T_e / T_h = 20 and T_e = 45000 (Ghorui, Heberlein, & Pfender, 2006)

The maximum T_e / T_h ratios as obtained from the simulation are much higher than 20. Near the nozzle walls, the degree of non-equilibrium is very high due to much colder heavy particles as compared to those in plasma plume. This is shown in Figure 6.27.

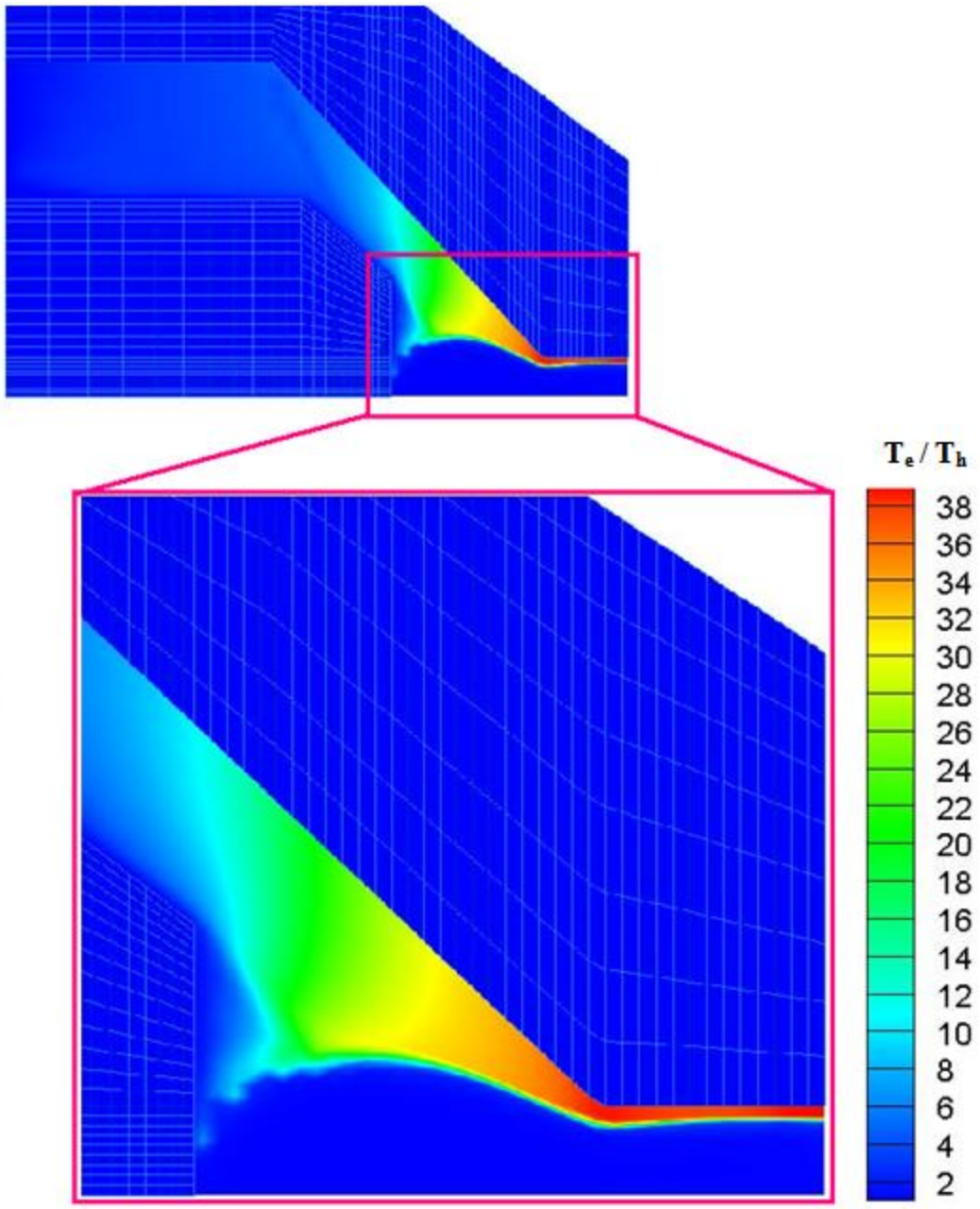

Figure 6.27: Plot of T_e / T_h for HT2000 torch

Excessively high values of T_e / T_h result in incorrect density values in the region in the proximity of the nozzle wall as shown in Figure 6.28. The majority of the mass flow is in this low temperature zone. Hence it is essential to obtain the correct density

values as opposed to the truncated density values as shown in Figure 6.28 in order to conserve mass flow at every section of the torch.

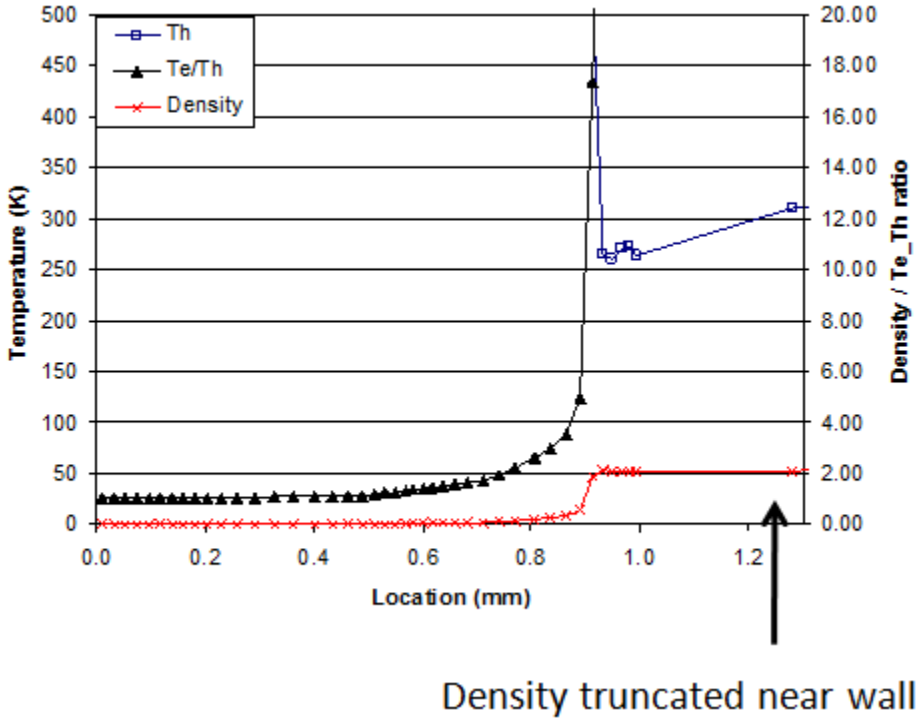

Figure 6.28: Density truncation due to excessively high T_e / T_h ratios

To reduce the ratio of the electron temperature to the heavy-particle temperature near the nozzle walls, the nozzle wall temperature was raised. As this temperature is one of the boundary conditions for the heavy-particle temperature energy equation, significant changes were observed in the plot of the electron temperature over the heavy-particle temperature as illustrated by Figure 6.29. This also improved mass conservation because the same flow velocity would now have a higher density.

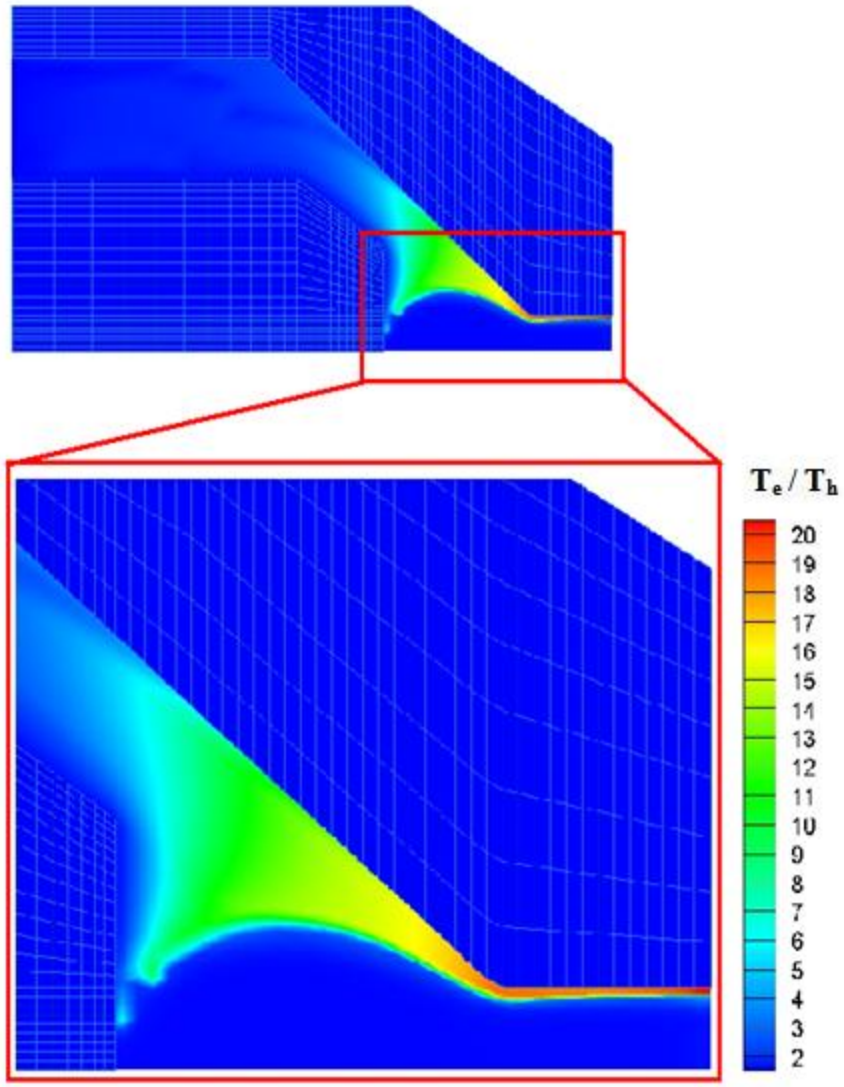

Figure 6.29: Corrected values of T_e / T_h ratios near nozzle wall

6.2.6 Second order exit boundary condition

The exit boundary conditions used for the simulation essentially assume a fully developed flow of plasma. This approach is valid only when the exit conditions are given at a sufficient distance away from the domain of interest. A better approach for any CFD simulation would be to use the second order boundary conditions at the exit, as the flow might not be fully developed in reality in order to use the first order boundary conditions.

The earlier set of exit boundary conditions used and the corresponding new boundary conditions are illustrated in Table 6.3.

Table 6.3: Earlier and current torch exit boundary conditions

Variable	1st order BC used in original simulation	Modified BC
U	$dU/dx = 0$	$d^2U/dx^2 = 0$
V	$dV/dx = 0$	$d^2V/dx^2 = 0$
W.r	$D(W.r)/dx = 0$	$D^2(W.r)/dx^2 = 0$
T_e	$dT_e/dx = 0$	$d^2T_e/dx^2 = 0$
T_h	$dT_h/dx = 0$	$d^2T_h/dx^2 = 0$
Φ (Potential)	$d\Phi/dx = 0$	$\Phi = 0$
κ	$d\kappa/dx = 0$	$d\kappa/dx = 0$
ε	$d\varepsilon/dx = 0$	$d\varepsilon/dx = 0$

The modified boundary conditions were converted into the discretized form with a finite difference approach for any variable ξ from Table 6.3 as described below.

$$\left.\frac{d^2\xi}{dx^2}\right|_k = \frac{\left.\frac{d\xi}{dx}\right|_k - \left.\frac{d\xi}{dx}\right|_{k-1}}{\Delta x}$$

$$= \frac{\frac{\xi_k - \xi_{k-1}}{\Delta x} - \frac{\xi_{k-1} - \xi_{k-2}}{\Delta x}}{\Delta x}$$

$$= \frac{\xi_k - 2\xi_{k-1} + \xi_{k-2}}{\Delta x^2}$$

$$\left.\frac{d^2\xi}{dx^2}\right|_k = 0 \rightarrow \xi_k - 2\xi_{k-1} + \xi_{k-2} = 0$$

It was observed that the results were not changed with the modified boundary conditions. Hence, it is valid to assume a fully developed flow at the exit.

6.2.7 Issue with torch exit condition

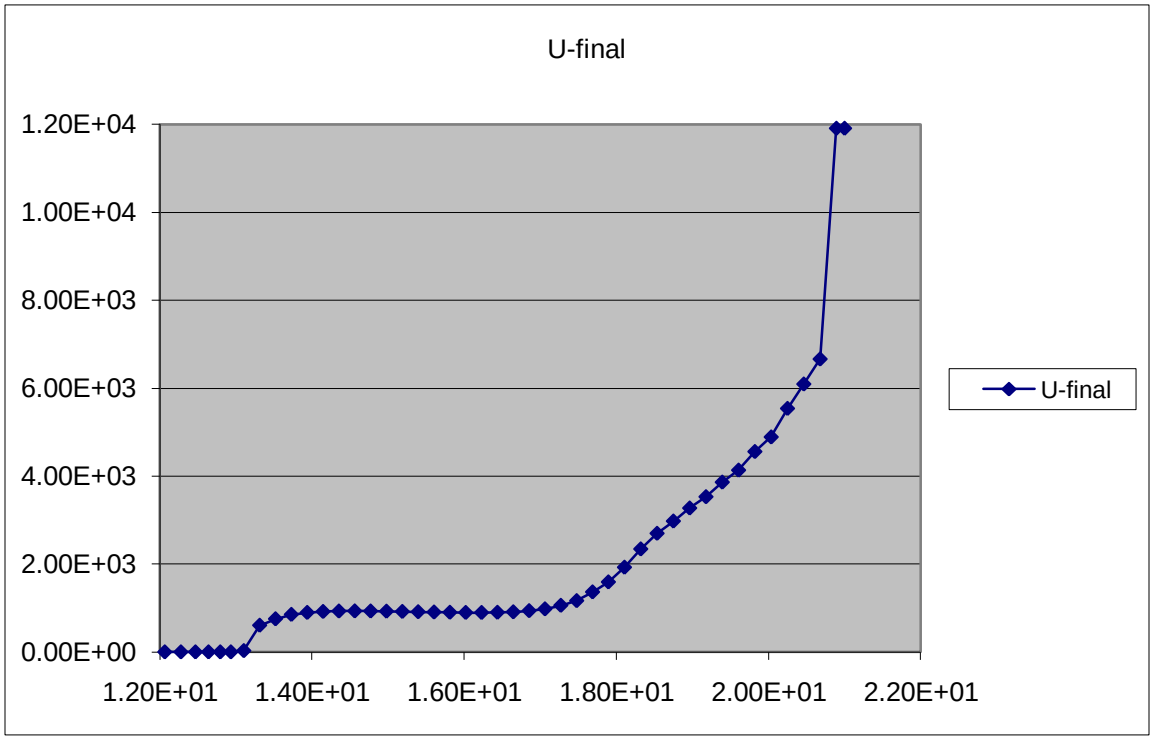

Figure 6.30: Axial velocity u (m/s) along the torch centerline

Figure 6.30 shows the plot of axial velocity u (m/s) along the torch centerline. As expected, the velocity increases rapidly in the nozzle portion of the torch but there is a sudden jump in the velocity near the torch exit, indicating the inaccuracy in representing the physical conditions at this location.

This problem could be solved with the simulation of the outside-nozzle-exit zone as this would allow the capturing of the shockwave as the plasma jet ejects out of the nozzle. This will be a part of the future developments in the code.

6.3 Simulation of HT4400 400A O_2/Air torch

6.3.1 About the torch (www.hypertherm.com, 2009)

The HySpeed HT4400 is a 400A dry oxygen plasma cutting system. Its single power supply delivers very high cut speeds – especially on thicker metals. At the same time, the HT4400 produces virtually no dross and delivers superior cut-face weldability over the widest range of material types and thicknesses.

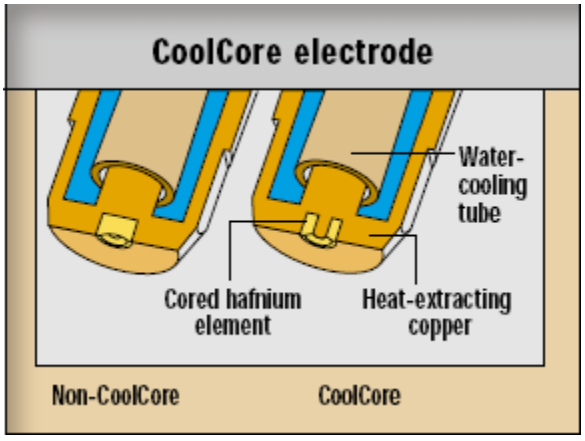

Figure 6.31: Cool-core electrode in HT4400

Two proprietary Hypertherm technologies allow high-speed cutting with maximum consumable life. The LongLife oxygen process involves precise control of key cutting parameters to gradually ramp up when starting the cut and ramp down when stopping. These are the times when consumable deterioration is most prevalent. As a result, the LongLife process significantly extends consumable life.

CoolCore electrodes are designed with the hafnium insert cored-out rather than utilizing a solid element. This permits heat-extracting copper to be in contact with both

the inside and outside surfaces of the hafnium. Transferring heat away from the hafnium results in a 2-fold increase in electrode life. Because of the cool-core electrode in HT4400 torch it would be most realistic to use a current density profile which is flat at the center. This is because of lower centerline temperatures on cathode surface resulting in lower current density values in accordance with the Richardson-Dushman equation.

A section of HT4400 torch along its axis is shown in Figures 6.32 and 6.33. The dimensions and other parameters for the grid generation are obtained on the basis of this drawing.

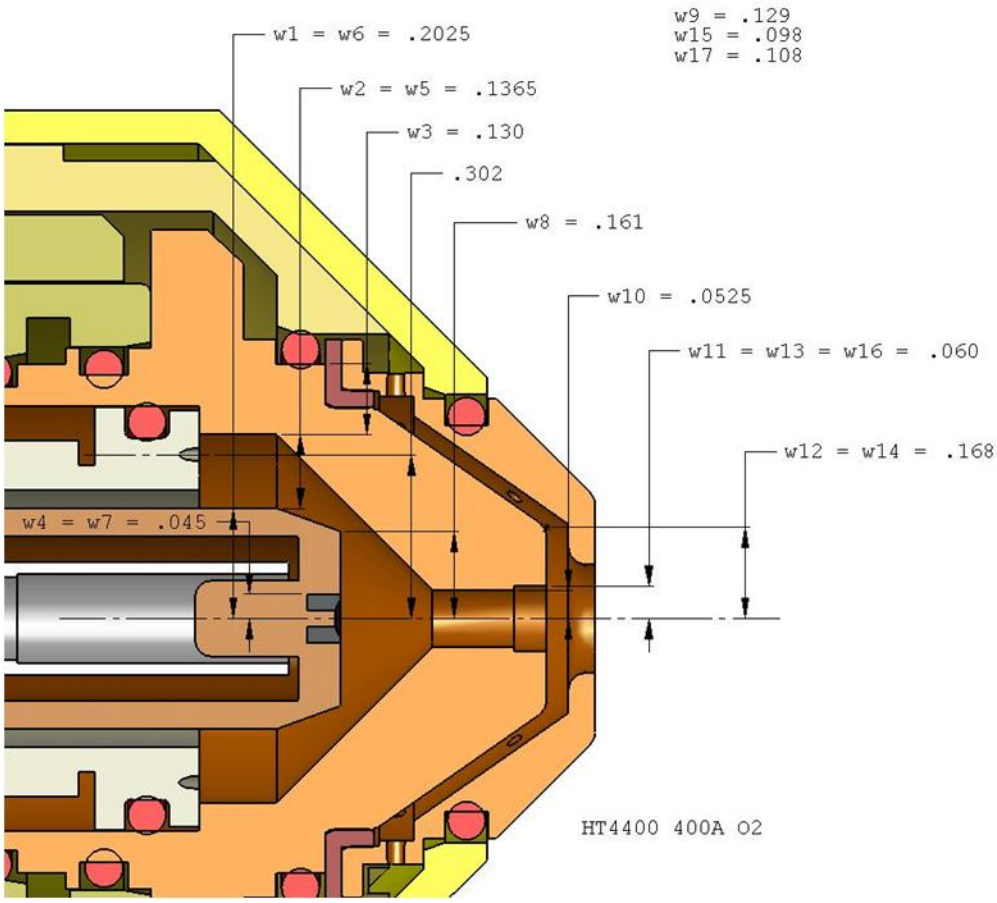

Figure 6.32: Section of HT4400 with radial dimensions (in mm)

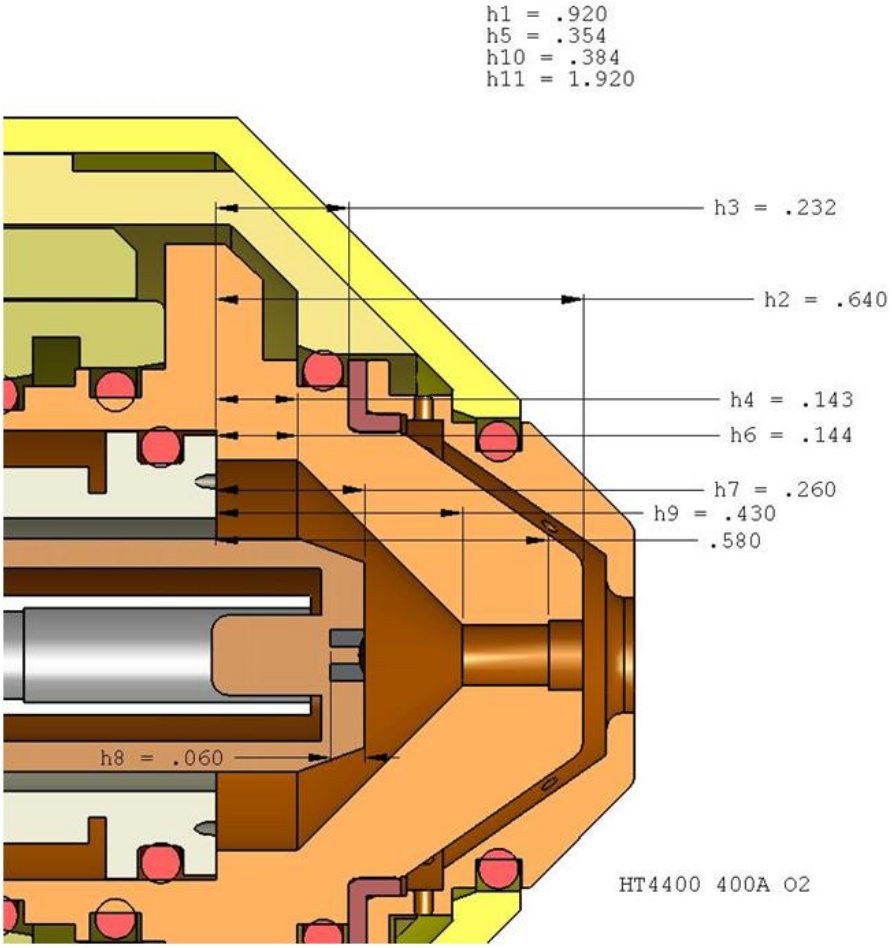

Figure 6.33: Section of HT4400 with axial dimensions (in mm)

6.3.2 Process parameters

The following two tables summarize the process parameters for HT4400 simulation.

Table 6.4: Steady state process parameters and torch specifications (400A torch)

Flow rate of O_2	$1.89908 \times 10^{-4}\ m^3/s$ (92.00 scfh)
Plasma plenum pressure	$418512\ Pa$ (46 psig)
Torch current	400A
Swirl injection type	Axial
Swirl angle	20°
Number of swirl injection holes	12
Diameter of swirl injection holes	$0.66\ mm$ (0.026")

Table 6.5: Steady state parameters converted to code parameters (400A torch)

TCRN	400 (A)
TAND	600 (K)
TIN	300 (K)
UIN	43.6 (m/s)
WIN	15.86 (m/s)
PRSIN	418512 (Pa)

6.3.3 Input velocity calculations from inlet flow rate

The calculations follow the steps described in section 6.1.3.

$$Flow\ rate = 92.0\ scfh$$

$$Inlet\ pressure = psig = 418512\ Pa$$

$$Inlet\ temperature = 300\ K$$

Converting standard flow rate for inlet conditions:

$$\frac{p_1 \dot{v}_1}{T_1} = \frac{p_2 \dot{v}_2}{T_2}$$

$$\frac{100000 \times 92.0}{273.15} = \frac{418512 \times \dot{v}_2}{300}$$

$$\dot{v}_2 = 24.14349\ ft^3/hr = 1.89908 \times 10^{-4}\ m^3/s$$

Area of inlet:

$$A = 12 \times \left(\pi/4\right) \times (0.026 \times 0.0254)^2 = 4.093 \times 10^{-6}\ m^2$$

$$Total\ velocity = \frac{1.89908 \times 10^{-4}}{4.093 \times 10^{-6}}$$

$$= 46.398\ m/s$$

$$UIN = 43.6\ m/s$$

$$WIN = 15.86\ m/s$$

Dimensions of inlet zone:

$$A_a = \frac{A_c}{\cos 20} = \frac{4.093 \times 10^{-6}}{0.9396926}$$

$$A_a = 4.352 \times 10^{-6} = 2\pi r d_A = 2\pi \times 0.302 \times 0.0254 \times d_A \times 0.0254$$

$$d_A = 0.00356"$$

6.3.4 Generated grid and simulation results:

The grid generated by the modified grid generator is shown in Figure 6.34.

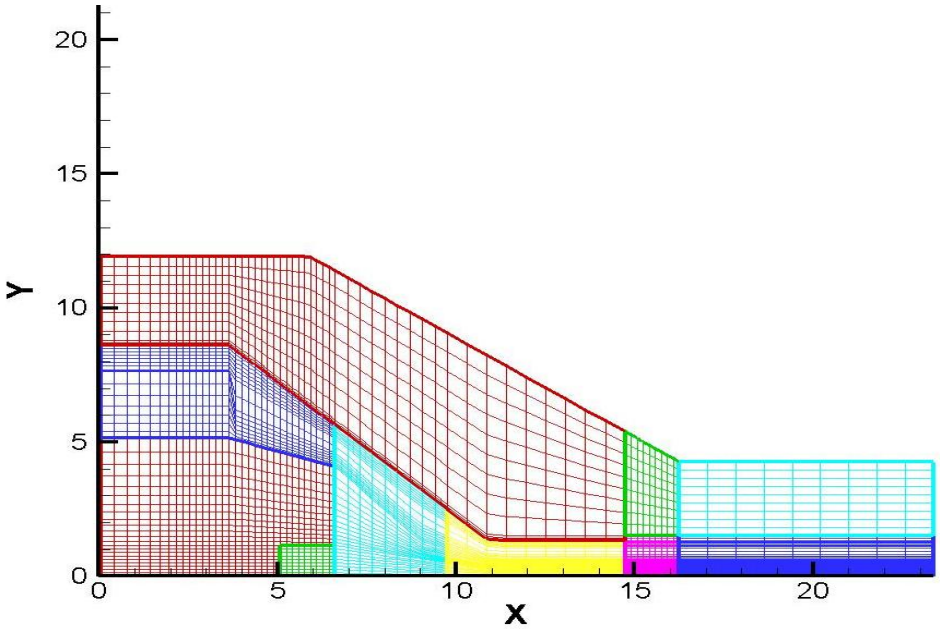

Figure 6.34: Mesh for HT4400 torch

Figure 6.35 shows the electron and the heavy-particle temperature distributions for the HT4400 torch for two effective radii of radiation (R_{eff} = 0.0 mm (optically thin plasma assumption) and R_{eff} = 0.5 mm). The upper half part of the plot represents the electron temperature distribution and the lower half part is the heavy-particle temperature distribution. As it is clear from the plots, the model with R_{eff} = 0.5 mm under-predicts the radiation losses and hence gives unreasonably high temperatures which do not occur in reality. The current density boundary condition at cathode, used for this simulation is given by $J = J_0 e^{-\left(\frac{2.8r}{R}\right)^3}$.

Figure 6.36 shows the velocity distributions for the two effective radii of radiation (R_{eff} = 0.0 mm (optically thin plasma assumption) and R_{eff} = 0.5 mm). The higher temperatures obtained with R_{eff} = 0.5 mm in turn lead to higher velocities as compared to the optically thin model, owing to the more energetic electrons in the former case.

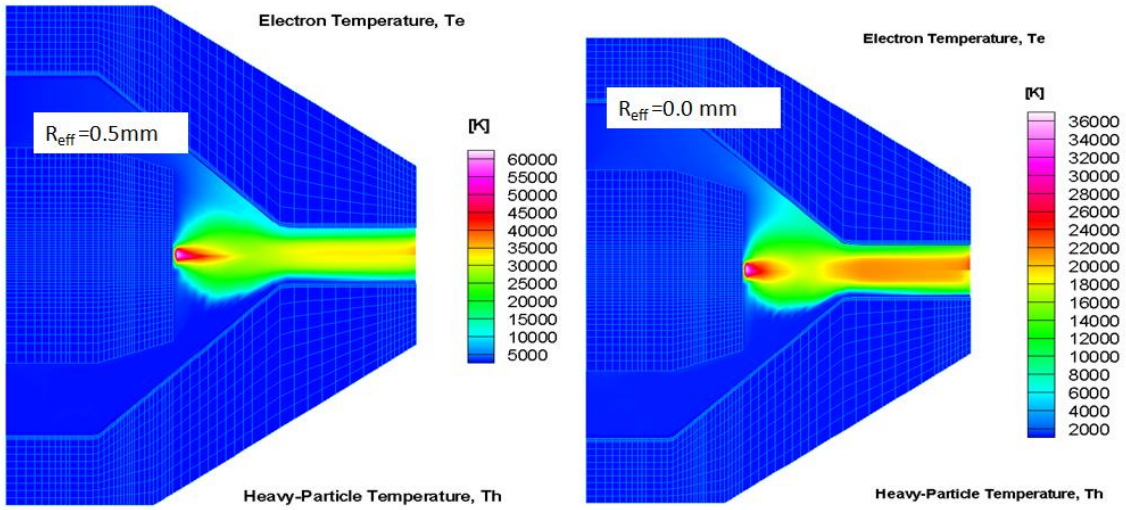

Figure 6.35: Electron and heavy-particle temperature distributions in HT4400 torch: (*left*) R_{eff} = 0.5 mm (*right*) R_{eff} = 0.0 mm

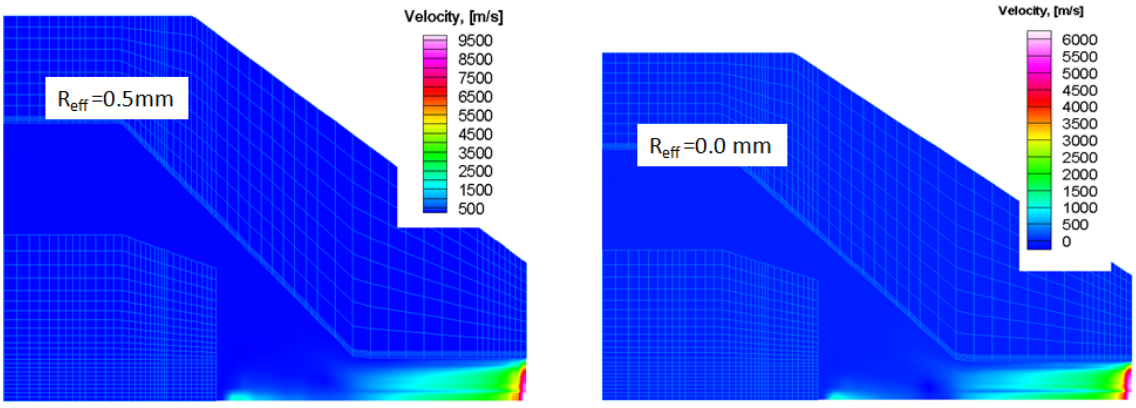

Figure 6.36: Velocity distributions in HT4400 torch: (*left*) R_{eff} = 0.5 mm (*right*) R_{eff} = 0.0 mm

The electric potential and current density plots are shown in Figures 6.37 and 6.38. The potential difference in case of the optically thin model is larger as compared to the model with R_{eff} = 0.5 mm by about 30 V. This is because of the conservation of the total energy in spite of the higher energy dissipation in case of the optically thin model. As the torch current remains 400A and the energy loss due to radiation assumes a higher value for R_{eff} = 0.0 mm, the potential difference increases in order to conserve the total energy.

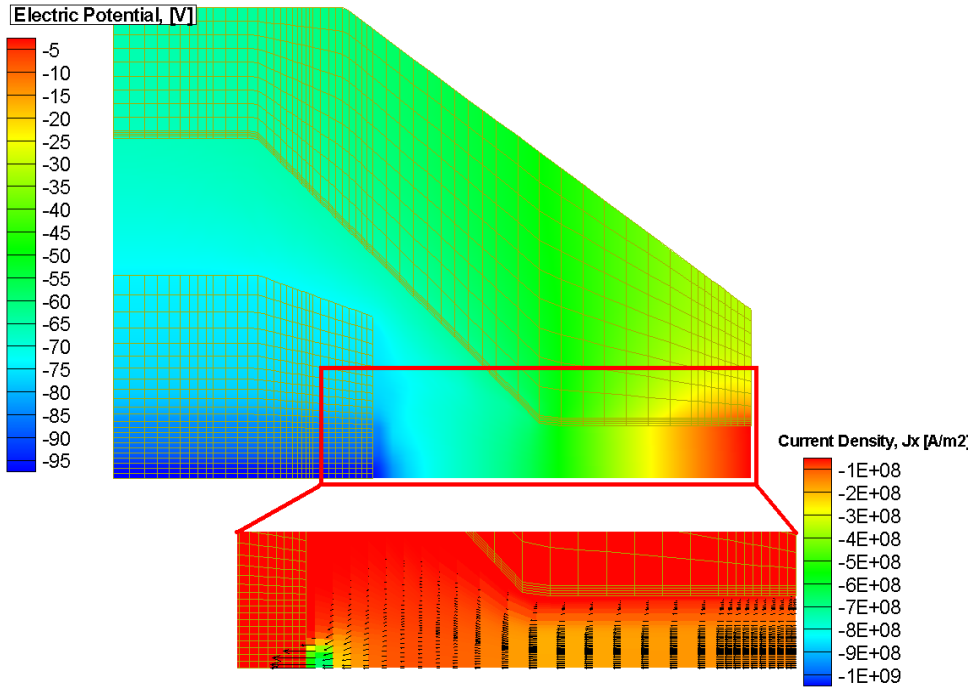

Figure 6.37: Electrical characteristics of HT4400 torch with R_{eff} = 0.5 mm: (*top*) electric potential distribution (*bottom*) axial current density distribution in front of cathode

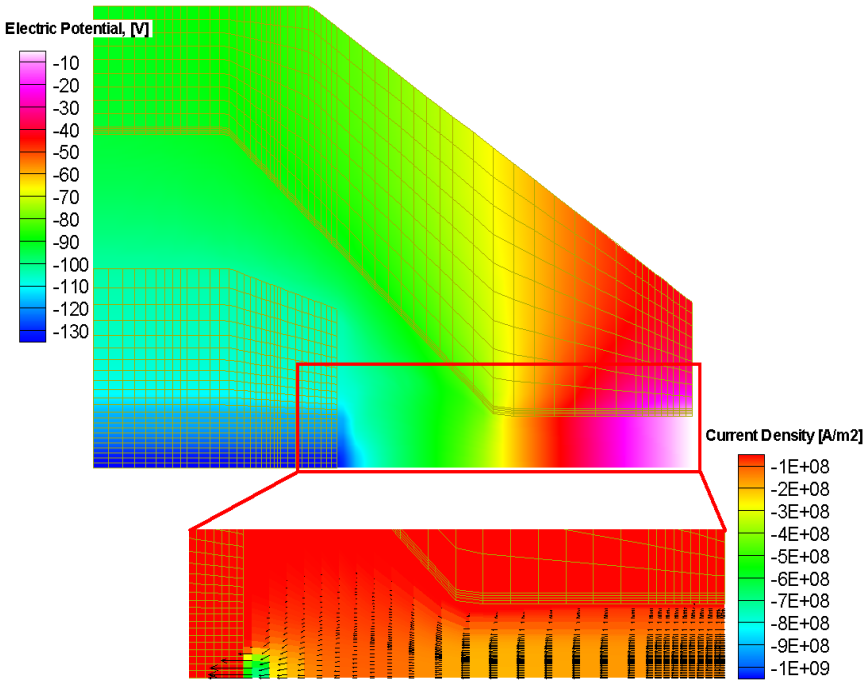

Figure 6.38: Electrical characteristics of HT4400 torch with R_{eff} = 0.0 mm: (*top*) electric potential distribution (*bottom*) axial current density distribution in front of cathode

6.4 Simulation of a 300A O_2/Air torch

6.4.1 Process parameters

The following two tables summarize the process parameters for the 300A torch simulation.

Table 6.6: Steady state process parameters and torch specifications (300A torch)

Flow rate of O_2	$8.6174 \times 10^{-5}\, m^3/s$ (50.00 scfh)
Plasma plenum pressure	$501248.8\, Pa$ (58 psig)
Torch current	300A
Swirl injection type	Axial
Swirl angle	20°
Number of swirl injection holes	12
Diameter of swirl injection holes	$0.57\, mm$ (0.0225")

Table 6.7: Steady state parameters converted to code parameters (300A torch)

TCRN	300 (A)
TAND	600 (K)
TIN	300 (K)
UIN	26.31 (m/s)
WIN	9.58 (m/s)
PRSIN	501248.8 (Pa)

6.4.2 Input velocity calculations from inlet flow rate

The calculations follow the steps described in section 6.1.3.

$$Flow\ rate = 50.0\ scfh$$

$$Inlet\ pressure = psig = 501248.8\ Pa$$

$$Inlet\ temperature = 300\ K$$

Converting standard flow rate for inlet conditions:

$$\frac{p_1 \dot{v}_1}{T_1} = \frac{p_2 \dot{v}_2}{T_2}$$

$$\frac{100000 \times 50.0}{273.15} = \frac{501248.8 \times \dot{v}_2}{300}$$

$$\dot{v}_2 = 10.9556\ ft^3/hr = 8.6174 \times 10^{-5}\ m^3/s$$

Area of inlet:

$$A = 16 \times \left({}^{\pi}/_{4}\right) \times (0.0225 \times 0.0254)^2 = 3.078 \times 10^{-6}\ m^2$$

$$Total\ velocity = \frac{8.6174 \times 10^{-5}}{3.078 \times 10^{-6}}$$

$$= 28.0\ m/s$$

$$UIN = 26.31\ m/s$$

$$WIN = 9.58\ m/s$$

Dimensions of inlet zone:

$$A_a = \frac{A_c}{\cos 20} = \frac{3.078 \times 10^{-6}}{0.9396926}$$

$$A_a = 2\pi r d_A = 2\pi \times 0.250 \times 0.0254 \times d_A \times 0.0254$$

$$d_A = 0.00323"$$

6.4.3 Generated grid and simulation results:

The grid generated by the modified grid generator is shown in Figure 6.39.

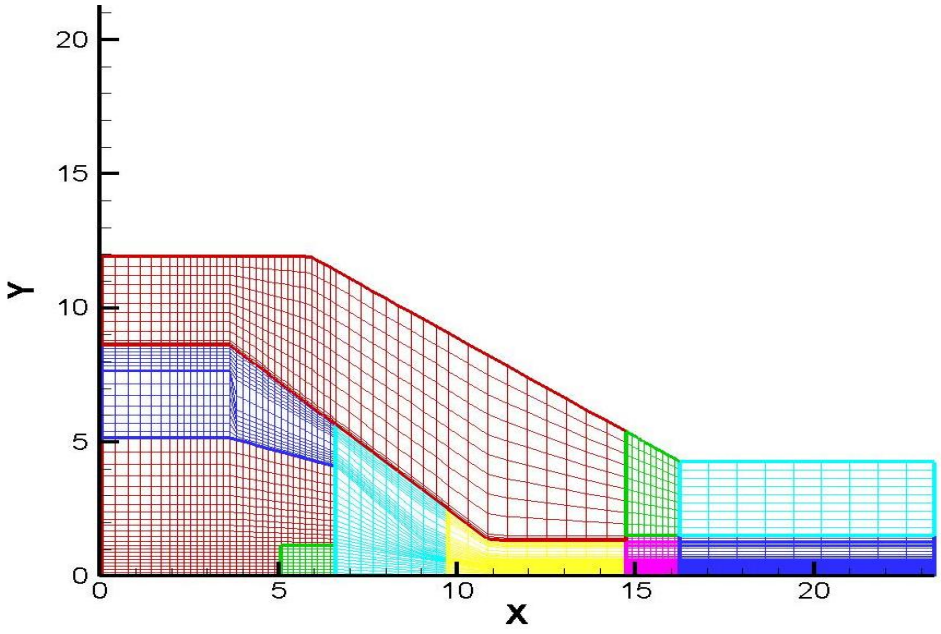

Figure 6.39: Mesh for 300A torch

Figure 6.40 shows the electron and the heavy-particle temperature distributions for the effective radius of radiation R_{eff} = *0.0 mm* (optically thin plasma assumption). The upper half part of the plot represents the electron temperature distribution and the lower half part is the heavy-particle temperature distribution. The current density boundary condition at cathode, used for this simulation is the same as the one used for HT2000 and HT4400 torches and is given by $J = J_0 e^{-\left(\frac{2.8r}{R}\right)^3}$.

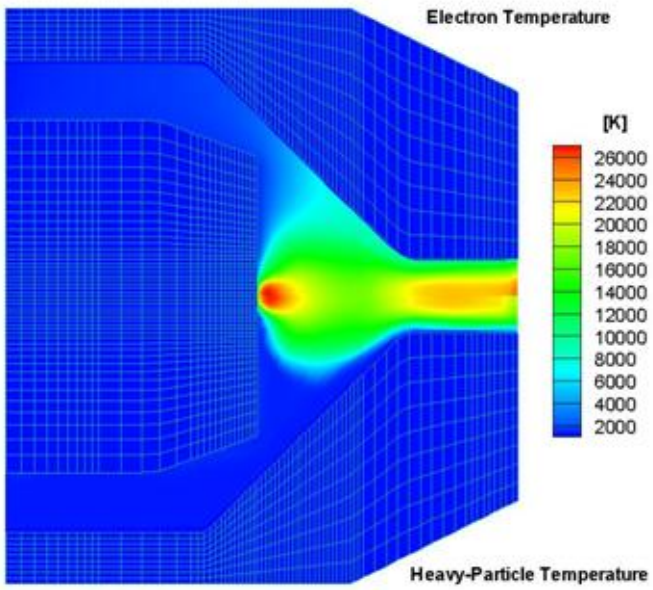

Figure 6.40: Electron and heavy-particle temperature distributions in 300A torch with optically thin radiation model

Figure 6.41 presenting the velocity distribution shows a maximum velocity of ~ 6000 m/s which is an intermediate value between the maximum values for the 200A (~ 5500 m/s) and 400A (~ 6500 m/s) torches.

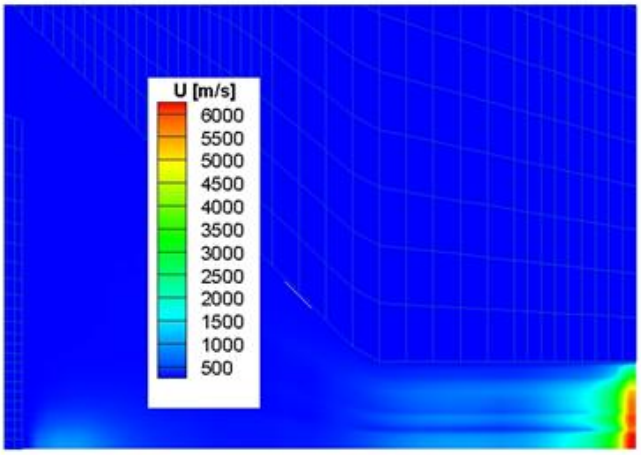

Figure 6.41: Velocity distributions in 300A torch with optically thin radiation model

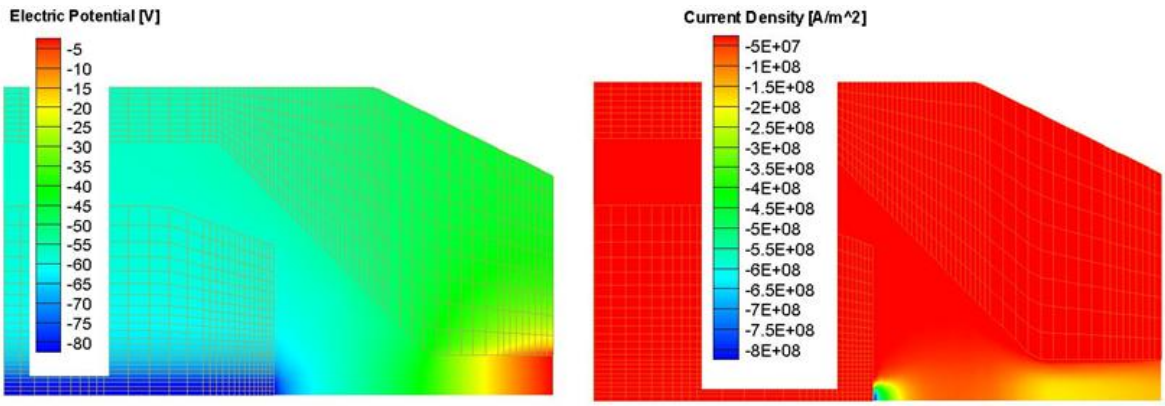

Figure 6.42: Electrical characteristics of 300A torch with optically thin model: (left) electric potential distribution (right) distribution of current density

Figure 6.42 presents the distribution of the electric potential as well as the current density in the axial direction. The obtained total voltage drop of ~ 75 V is comparable to the voltage drop of 72 V obtained experimentally.

Figure 6.43 presents a comparison of the nozzle exit temperature profiles for the three torches in consideration. As expected, the temperatures are in ascending order as we go from the lowest current value of 200A to the highest current value of 400A. However, the profiles for the 200A and 300A torches are closer together as compared to the profiles for the 300A and 400A torches. This is because the HT4400 400A torch has a longer nozzle bore as opposed to the shorter ones in the other two torches. It is also reflected in Figure 6.44 showing a comparison of the nozzle exit velocity profiles. As the plasma gas achieves higher temperatures in the HT4400 torch, we have lower densities for a high mass flow rate (92 scfh) which results in significantly higher velocity values. Hence we have higher velocity difference between the 400A and the 300A torch as compared to the difference between the velocities in the 300A and the 200A torch.

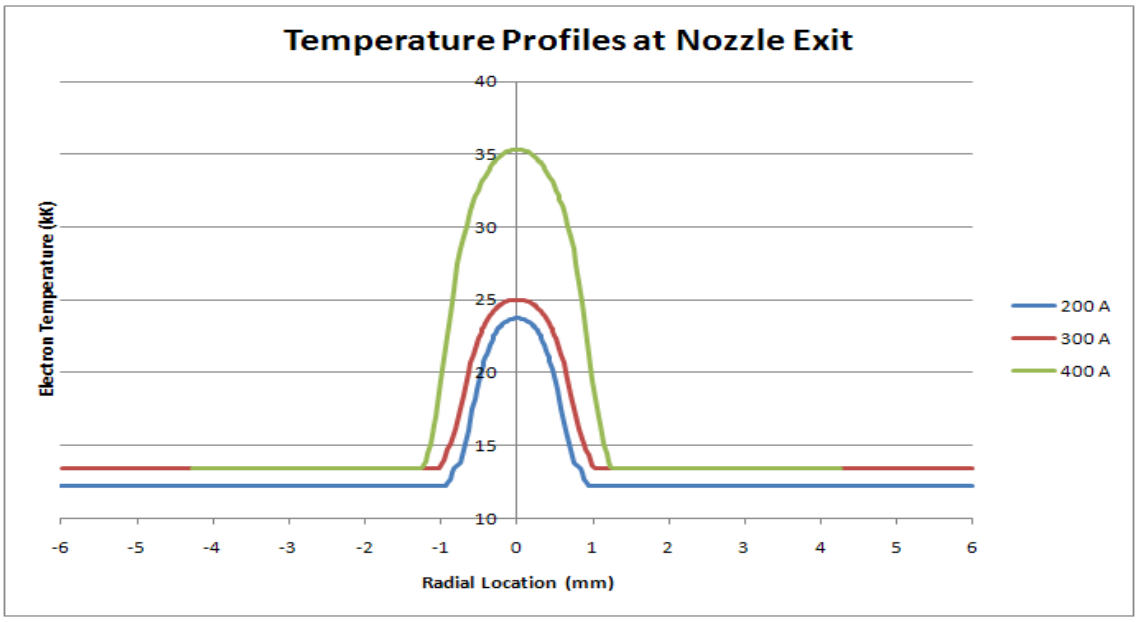

Figure 6.43: Comparison of nozzle exit temperature profiles for 200A (HT2000), 300A and 400A (HT4400) torches

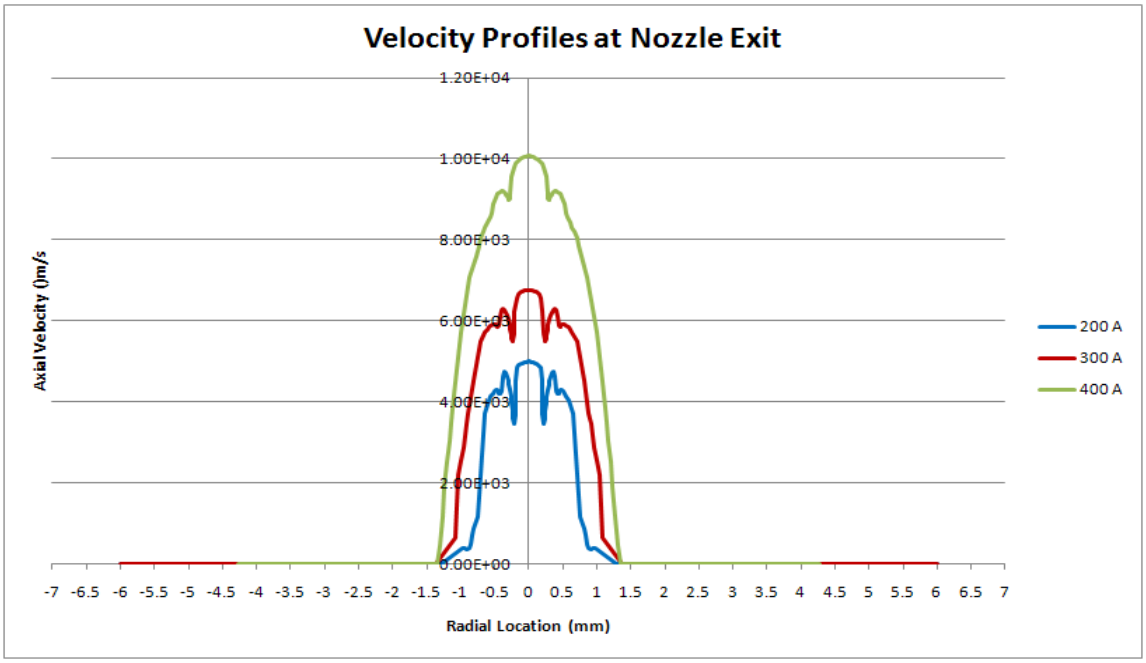

Figure 6.44: Comparison of nozzle exit velocity profiles for 200A (HT2000), 300A and 400A (HT4400) torches

7. CONCLUDING REMARKS AND RECOMMENDATIONS

7.1 Concluding remarks

1. A new geometry subroutine (MAKEGRIDX.f) was developed with the ability to input the nozzle exit cone/counter-bore, vent flow and the specific size and location of the swirl injection. This routine allowed the complete specification of the geometrical characteristics (possible in 2-D geometry) of the existing 200A, 300A and 400A cutting torches from Hypertherm, as well as the future torch designs. The new routine is recognized by its modularity and user-friendliness. This would make its further modification, in order to accommodate future design changes, straightforward.
2. The radiation data for oxygen used in the earlier version of the code underestimated the radiation losses for the temperatures above ~ 25000 K. New radiation data for oxygen plasmas, based on the net emission approximation and provided by Gleizes *et al*, was incorporated into the NEQ version of FAST-2D.
3. From the simulation of HT2000 with two different effective absorption radii, it was observed that the radiation loss term had a noticeable effect on the predicted maximum temperatures and velocities, and only a mild effect on the electrical characteristics of the flow inside cutting torches. Simulations of the HT2000 torch using two values of the net absorption radius in the net emission approximation highlighted the importance of the adequate modeling of the radiative energy transfer in thermal plasma flow simulations.

4. Simulation of HT4400 with different current density profiles at the cathode suggested that this boundary condition plays an important role in determining the plasma solution fields. This also emphasized the need for experimental data to validate the used current density boundary condition at the cathode for a 400A cutting torch.
5. The temperature distributions for the set (c = 2.8, R_{eff} = 0.0 mm) in Figure 6.39 and (c = 2.6, R_{eff} = 0.5 mm) in Figure C.7 are comparable and hence it is worth checking the simulation results with an intermediate effective absorption radius. That might give the most accurate radiation energy loss model to obtain physically sound results of the non-equilibrium modeling of thermal plasma flows in plasma cutting torches.
6. Simulation of the 300A torch showed various plasma field quantity distributions, with values between those for the 200A and 400A torches. This fact emphasizes the validity of results produced by the NEQ code.

7.2 Recommendations

1. Validate the results for the 300A and 400A torches with supporting experimental work (Electrode temperature measurement for current density boundary condition and/or spectroscopic measurement of plasma properties at the torch exit).
2. Modify the solver of the code to handle two directional flows (the current version of the code can handle mainly axial flows but not vent flows and radial swirl injection geometries).
3. Fix the property code to address very large values of T_e / T_h ratios - expand tables or use ideal gas law.
4. Expand model to include cathode boundary condition model by calculated heat flux to the hafnium from the plasma and heat flux away from hafnium trough conduction.

8. BIBLIOGRAPHY

(2009). Retrieved from www.hypertherm.com.

Boulos, M. I., Fauchais, P., & Pfender, E. (1994). *Thermal Plasmas: Fundamentals and Applications.* New York: Plenum Press.

Colombo, V., Concetti, A., Ghedini, E., Dallavalle, S., & Vancini, M. (2008). Understanding Plasma Fluid Dynamics Inside Plasma Torches Through Advanced Modeling. *Plasma Science, IEEE Transactions on 36* , 389-402.

Colombo, V., Ghedini, E., & Mostaghimi, J. (2008). Three-Dimensional Modeling of an Inductively Coupled Plasma Torch for Spectroscopic Analysis. *Plasma Science, IEEE Transactions on 36* , 1040-1041.

Couch Jr., R. W., Sanders, N. A., Luo, L., Sobr, J., & Backander, P. (1994). *Patent No. 5317126.* USA.

Freton, P., Gonzalez, J. J., Gleizes, A., Peyret, F. C., Caillibotte, G., & Delzenne, M. (2002). Numerical and experimental study of a plasma cutting torch. *J. Phys. D: Appl. Phys. 35* , 115-131.

Freton, P., Gonzalez, J. J., Peyret, F. C., & Gleizes, A. (2006). Complementary experimental and theoretical approaches to the determination of the plasma characteristics in a cutting plasma torch. *J. Phys. D: Appl. Phys. 36* , 1269-1283.

Ghorui, S., Heberlein, J. V., & Pfender, E. (2006). *Hypertherm Report No. 7: Non-Equilibrium Modeling of Oxygen Plasma - Determination of Non-equilibrium Thermodynamic and Transport Properties up to 50,000K.* University of Minnesota.

Ghorui, S., Heberlein, J. V., & Pfender, E. (2007). *Hypertherm Report No. 8: Non-Equilibrium Modeling of Oxygen Plasma - Determination of Temperature Distribution Using One Dimensional Arc Model and Development of a General Finite Volume 2-D Grid Generator For Arc Torches.* University of Minnesota.

Ghorui, S., Heberlein, J. V., & Pfender, E. (2006). *Hypertherm Report No. 9: Thermodynamic and transport properties of Two-Temperature Nitrogen-Oxygen plasma.* University of Minnesota.

Ghorui, S., Heberlein, J. V., & Pfender, E. (2007). Non-equilibrium modelling of an oxygen-plasma cutting torch. *J. Phys. D: Appl. Phys.40* , 1966-1976.

Ghorui, S., Heberlein, J. V., & Pfender, E. (2007). Thermodynamic and Transport Properties of Two-temperature Oxygen Plasmas. *Plasma Chemistry and Plasma Processing 27* , 267-291.

Gleizes, A., & Cressault, Y. (2007, November). Private Communication. LAPLACE - Université Paul Sabatier, France.

Hsu, K. C., & Pfender, E. (1983). Analysis of the cathode region of a free-burning high intensity argon arc. *J. Phys. D: Appl. Phys. 54* , 3818-3824.

Krey, R. U., & Morris, J. C. (1970). Experimental Total and Total Line Radiation of Nitrogen, Oxygen, and Argon Plasmas. *The Physics of Fluids 13* , 1483.

Li, H. P., & Chen, X. (2001). Diffusion in Two-Temperature Partially Ionized Gases. *Chinese Physics Letters, 18* , 547-549.

Li, H. P., Heberlein, J. V., & Pfender, E. (2004). *Hypertherm Report No. 1: Modeling of Hypertherm Plasma Cutting Torch (HT2000) – Phase 1: Calculation of the Composition and of Thermodynamic Properties of Two-Temperature Oxygen Plasmas.* University of Minnesota.

Li, H. P., Heberlein, J. V., & Pfender, E. (2004). *Hypertherm Report No. 2: Modeling of Hypertherm Plasma Cutting Torch (HT2000) – Phase 2: Basic Equations for the Calculation of Transport Properties of Two-Temperature Oxygen Plasmas.* University of Minnesota.

Li, H. P., Heberlein, J. V., & Pfender, E. (2004). *Hypertherm Report No. 3: Modeling of Hypertherm Plasma Cutting Torch (HT2000) –Phase 3: Composition, Thermodynamic, and Transport Properties of Two-Temperature Oxygen Plasmas.* University of Minnesota.

Li, H. P., Heberlein, J. V., & Pfender, E. (2004). *Hypertherm Report No. 4: Modeling of Hypertherm Plasma Cutting Torch (HT2000) – Phase 4: Physical/Mathematical Two-Temperature Model.* University of Minnesota.

Li, H. P., Heberlein, J. V., & Pfender, E. (2005). *Hypertherm report No. 5: Modeling of Hypertherm Plasma Cutting Torch (HT2000) – Phase 5: A Unified Method for Computing Incompressible and/or Compressible Flows with Arbitrary Boundaries.* University of Minnesota.

Li, H. P., Heberlein, J. V., & Pfender, E. (2005). *Hypertherm Report No. 6: Modeling of Hypertherm Plasma Cutting Torch (HT2000) – Phase 6: Physical/Mathematical Models and Modeling Results.* University of Minnesota.

Lowke, J. J. (1974). Predicitons of Temperature Profiles Using Approximate Emission Coefficients for Radiation Losses. *Journal of Quantitative Spectroscopy Radiative Transfer 14* , 111-122.

Mitchner, M., & Kruger, C. H. (1992). *Partially Ionized Gases.* USA: John Wiley & Sons, Inc.

Nemchinsky, V. A. (1998). Plasma flow in a nozzle during plasma arc cutting. *J. Phys. D: Appl. Phys. 31* , 3102-3107.

Patankar, S. V. (1980). *Numerical Heat Transfer and Fluid Flow.* New York: McGraw-Hill.

Peters, J. (2003). Cathode erosion in a plasma cutting torch. *MS Thesis* . University of Minnesota, MN.

Ramakrishnan, S., Gershenzon, M., Polivka, F., Kearney, T. N., & Rogozinsk, M. W. (1997). Plasma Generation for the Plasma Cutting Process. *IEEE TRANSACTIONS ON PLASMA SCIENCE 25* , 937-946.

Schnick, M., Füssel, U., & Zschetzsche, J. (2006). Simulation of plasma and shielding gas flows in welding and cutting arcs with Ansys CFX. *Modelling for Material Processing.* Riga: International Scientific Colloquium.

Trelles, J. P., Heberlein, J. V., & Pfender, E. (2007). *Hypertherm Report No. 1: Modeling of Hypertherm Plasma Cutting Torches (HT4400 and 9427 Rev1)*. University of Minnesota.

Trelles, J. P., Heberlein, J. V., & Pfender, E. (2007). *Hypertherm Report No. 2: Modeling of Hypertherm Plasma Cutting Torches (HT4400 and 9427 Rev1).* . University of Minnesota.

Vincenti, W. G., & Kruger, C. H. (1965). *Introduction to Physical Gas Dynamics.* New York: John Wiley and Sons.

www.castolin.com. (2009).

www.dgkk.de. (2009). Retrieved from http://www.dgkk.de/PDF/kinsim09/Spille_Kohoff.pdf.

Zhou, X., & Heberlein, J. V. (1998). An experimental investigation of factors affecting arc-cathode erosion. *Journal of Physics D: Applied Physics* , 2577-2590.

Zhu, J. (1991). *FAST-2D: A computer program for numerical simulation of two-dimensional incompressible flows with complex boundaries.* Institute for hydromechanics, University of Karlsruhe.

APPENDIX A: VARIABLES IN FAST-2D

Geometry Variables:

Variable	Description	Index[1]
ISCOX, ISCOY	x, y coordinates of control volume vertices (grid-corner points)	1,2
ISX, ISY	x, y coordinates of control volume center	3,4
ISR	Coordinate r of cylindrical coordinates	5
ISFX, ISFY[2]	Linear Interpolation factors f_x , f_y	6,7
ISVOLP	Volume of control volume	8
ISB11W	$y_{nw} - y_{sw}$	9
ISB12W	$x_{sw} - x_{nw}$	10
ISB21W	$y_W - y_P$	11
ISB22W	$x_P - x_W$	12
ISB11S	$y_P - y_S$	13
ISB12S	$x_S - x_P$	14
ISB21S	$y_{sw} - y_{se}$	15
ISB22S	$x_{se} - x_{sw}$	16
ISB11P	$y_n - y_s$	17
ISB12P	$x_s - x_n$	18
ISB21P	$y_w - y_e$	19
ISB22P	$x_e - x_w$	20

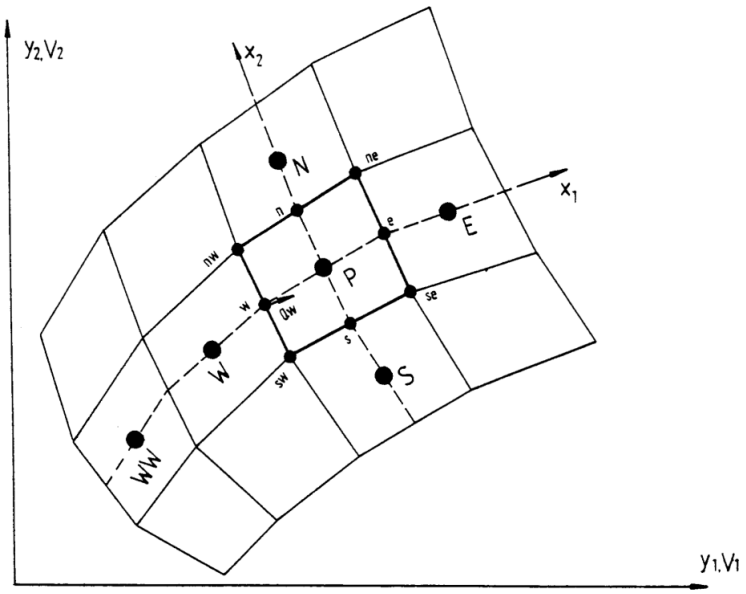

Figure A1 : A typical control volume centered at node P along with neighboring nodes (Zhu, 1991)

Other Variables:

Variable	Description	Index
ISPP[3]	Pressure correction	21
ISU	Axial velocity at time level n	22
ISV	Radial velocity at time level n	23
ISWR	(Azimuthal velocity)W.r	24
ISTE	Turbulent kinetic energy at time level n	25
ISED	Dissipation rate (ε) at time level n	26
ISAH	Enthalpy at time level n	27
ISTEM	Electron temperature at time level n	28
ISEP	Electric potential at time level n	29
ISZFE	Species Concentration- Electrons at time level n	30
ISZFI	Species Concentration- Heavy Particles at time level n	31
ISP	Pressure at time level n	32
ISDEN	Mass density at time level n	33
ISMUT	Turbulent viscosity	34
ISW	Azimuthal velocity at time level n	35
ISCW, ISCS	Convective coefficients C_w ,C_s	36,37
ISAW, ISAE, ISAS, ISAN, ISAP	Coefficients A_W , A_E , A_S , A_N , A_P	38,39,40,41,42
ISSU, ISSP	Source terms for difference equation	43,44
ISAPU, ISAPV	$1/A_p$ for U and V momentum equation	45,46
ISSUMU, ISSUMV	(A_E , A_W , A_N , A_S)/ A_P for U and V momentum equation	47,48
ISP1	Pressure at time level n-1	49
ISU1	Axial velocity at time level n-1	50
ISV1	Radial velocity at time level n-1	51
ISW1	Azimuthal velocity at time level n-1	52
ISK1	Turbulent kinetic energy at time level n-1	53
ISE1	Dissipation rate (ε) at time level n-1	54
ISAH1	Enthalpy at time level n-1	55
ISTEM1	Electron temperature at time level n-1	56
ISEP1	Electric potential at time level n-1	57
ISZFE1	Species Concentration- Electrons at time level n-1	58
ISZFI1	Species Concentration- Heavy Particles at time level n-1	59
ISP2	Pressure at time level n-2	60
ISU2	Axial velocity at time level n-2	61

ISV2	Radial velocity at time level n-2	62
ISW2	Azimuthal velocity at time level n-2	63
ISK2	Turbulent kinetic energy at time level n-2	64
ISE2	Dissipation rate (ε) at time level n-2	65
ISAH2	Enthalpy at time level n-2	66
ISTEM2	Electron temperature at time level n-2	67
ISEP2	Electric potential at time level n-2	68
ISZFE2	Species Concentration- Electrons at time level n-2	69
ISZFI2	Species Concentration- Heavy Particles at time level n-2	70
ISGAM, ISGAMW, ISGAMS	Effective diffusion coefficient	71, 72, 73
ISB	Azimuthal component of self induced magnetic field	74
ISJX	Axial current density component	75
ISJR	Radial current density component	76
ISDEN1, ISDEN2	Density at time level n-1, n-2	77, 78
ISUW, ISVW, ISUS, ISVS	Velocity interpolations on west and south faces	79, 80, 81, 82
ISTMH, ISTMH1,ISTMH2	Heavy particle temperature at time levels n, n-1, n-2	83, 84, 85

[1] Index number in represents the order of the corresponding variable in array F

[2] Interpolation factors are given by: $f_x = l_{wW} / (l_{Pw} + l_{wW})$ & $f_y = l_{sS} / (l_{Ps} + l_{sS})$ where l_{wW} , l_{wW} , l_{wW} , l_{wW} are lengths of linear segments wW, Pw, sS, Ps

[3] Variables in red are the ones for which the governing equations are solved

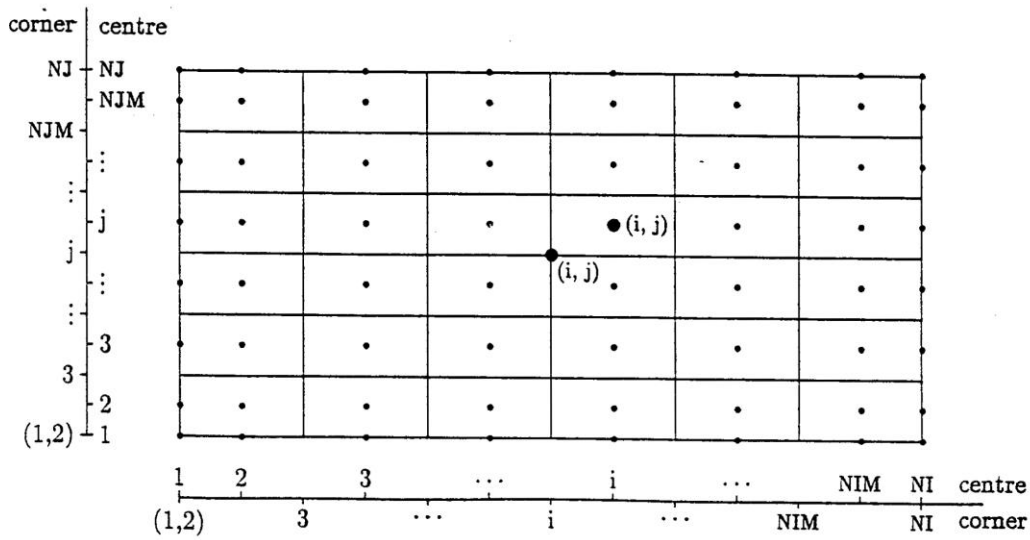

Figure A2 : Layout and indexing of cell center and corner points (Zhu, 1991)

APPENDIX B: SUBROUTINES AND OUTPUT FILES IN NEQ CODE

Code Subroutines:

1. BOUNDS: boundary conditions → geometry specific
2. COEFF: FAST2D, coefficients
3. FILES_SPEBND: FAST2D, boundary conditions; i.e. for solid domains, specify $\mu = \infty$
4. FLOSOL: FAST2D, solver
5. USER: Inputs from user
6. INTIA_CURRENT: inserts current density profile as a boundary condition
7. SETJ: calculates current density profile
8. MAIN: Calls other subroutines
9. MAKEGRIDX: mesh generation
10. OVACON: checks overall conservation (~ SIMPLEC algorithm)
11. SAVINGS_MAGNET: generation of TECPLOT files
12. SOURCE: specification source terms

Output Files:

Output files are generated each 500 iterations

MESH: complete mesh

TEMxxxx: electron temperature

TMHxxxx: heavy and electron temperature

VELxxxx: velocity

FAIxxxx: potential

CURxxxx: current density

MCHxxxx: Mach number

Here xxxx represents the file number.

APPENDIX C: SOLUTION FIELDS FOR A RANGE OF CURRENT DENSITY PROFILE BOUNDARY CONDITIONS AT THE CATHODE FOR R_{EFF} = 0.5 MM IN HT4400 TORCH

1) $c = 1.7 \rightarrow J = J_0 e^{-\left(\frac{1.7r}{R}\right)^3}$

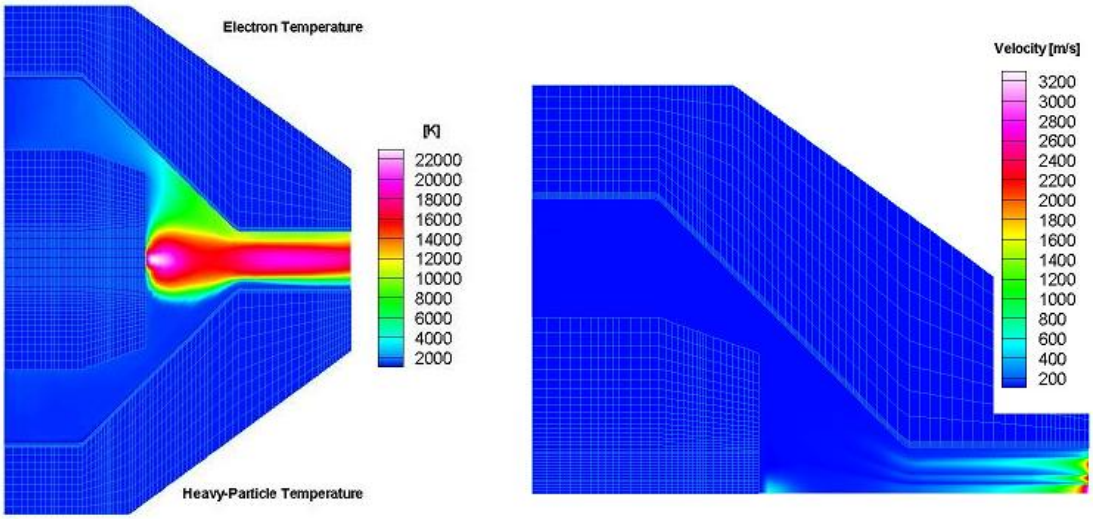

Figure C.1: Results with $c = 1.7$: (*left*) temperature distribution and (*right*) velocity distribution

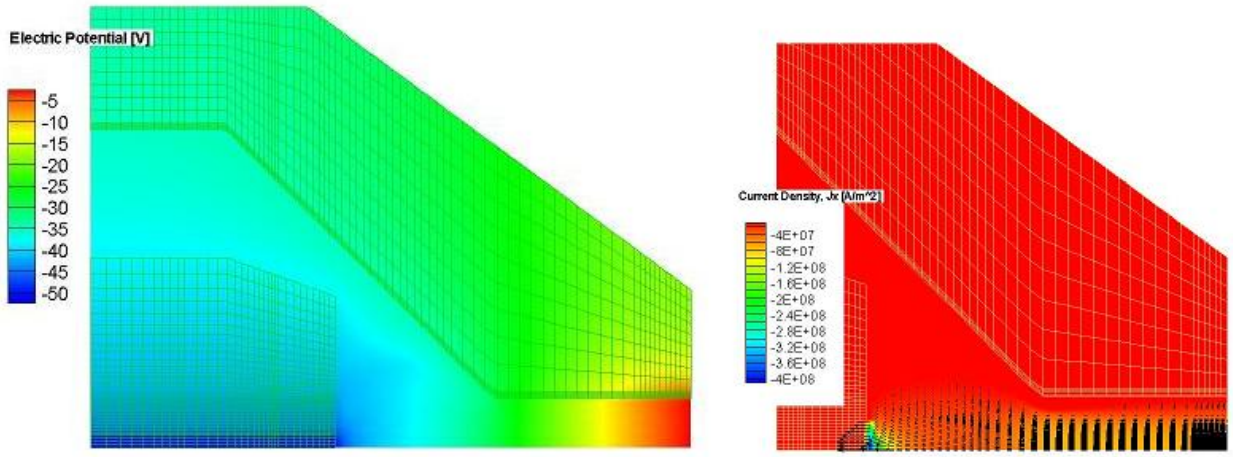

Figure C.2: Results with $c = 1.7$: (*left*) electric potential distribution and (*right*) current density distribution

2) $c = 2.0 \rightarrow J = J_0 e^{-\left(\frac{2.0r}{R}\right)^3}$

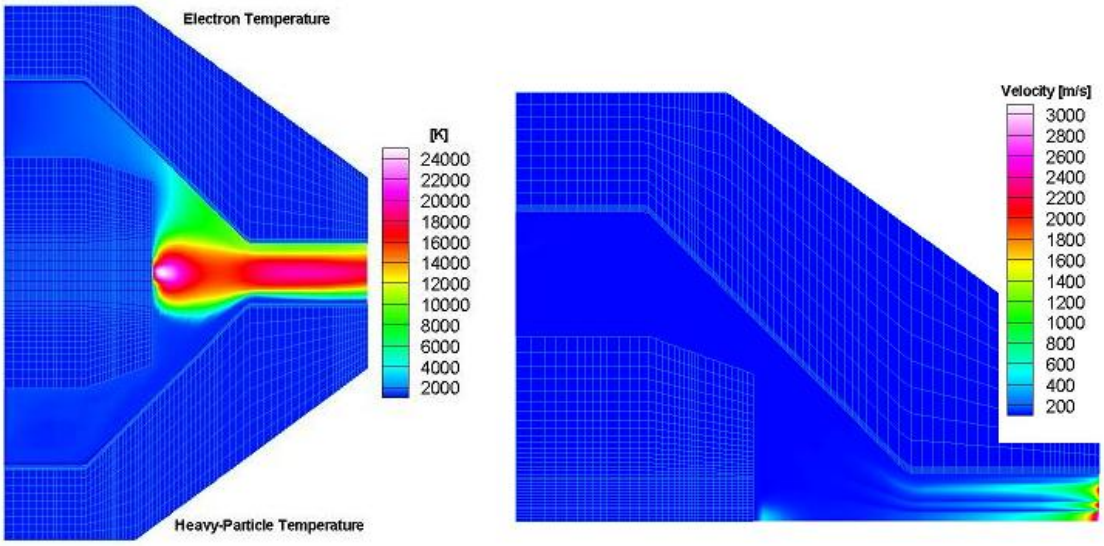

Figure C.3: Results with $c = 2.0$: (*left*) temperature distribution and (*right*) velocity distribution

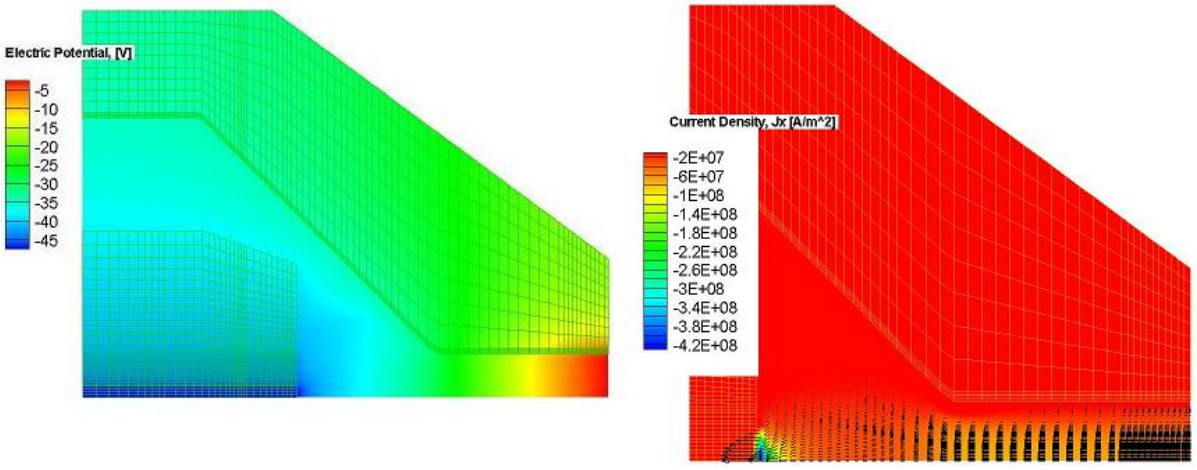

Figure C.4: Results with $c = 2.0$: (*left*) electric potential distribution and (*right*) current density distribution

3) $c = 2.3 \rightarrow J = J_0 e^{-\left(\frac{2.3r}{R}\right)^3}$

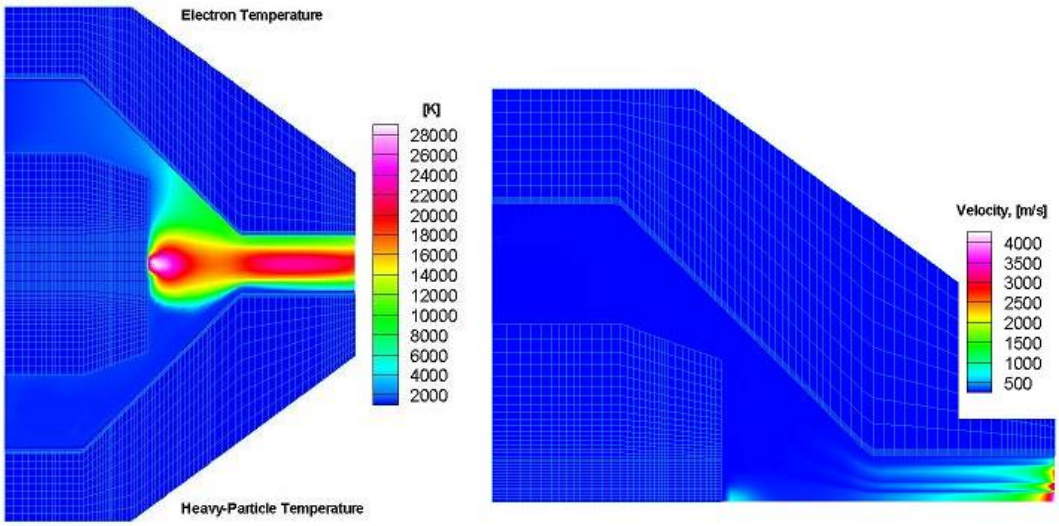

Figure C.5: Results with $c = 2.3$: (left) temperature distribution and (right) velocity distribution

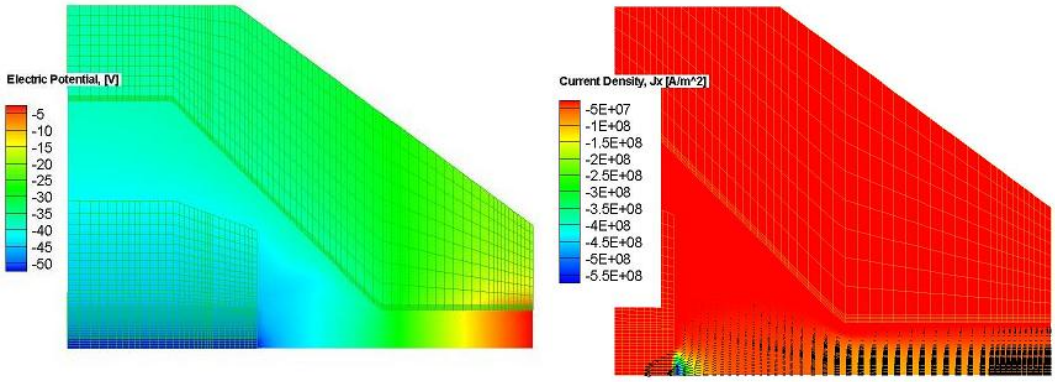

Figure C.6: Results with c = 2.3: (*left*) electric potential distribution and (*right*) current density distribution

4) $c = 2.6 \rightarrow J = J_0 e^{-\left(\frac{2.6r}{R}\right)^3}$

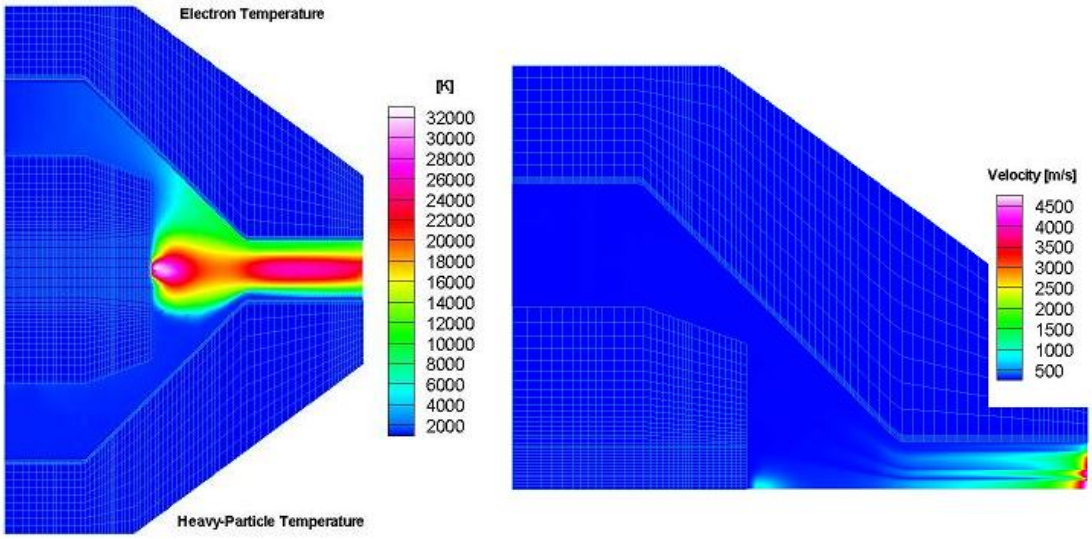

Figure C.7: Results with c = 2.6: (*left*) temperature distribution and (*right*) velocity distribution

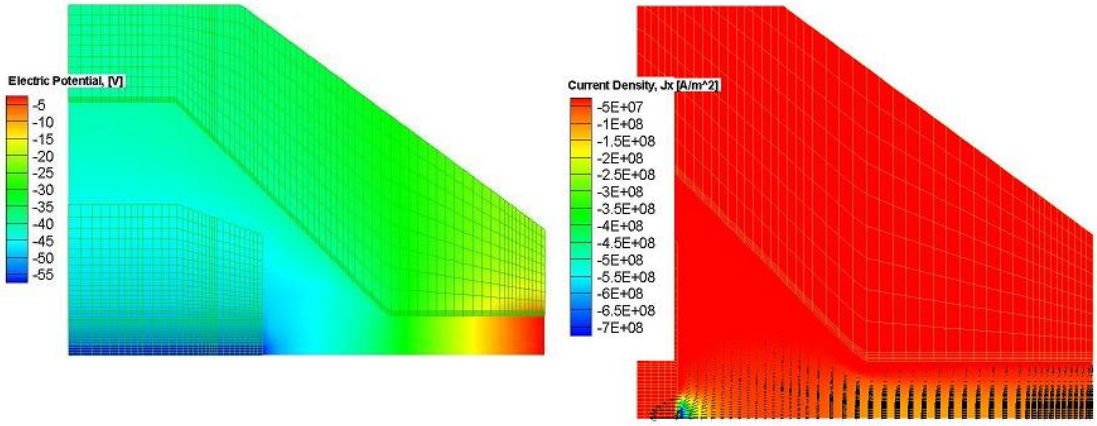

Figure C.8: Results with c = 2.6: (*left*) electric potential distribution and (*right*) current density distribution

5) $c = 2.7 \rightarrow J = J_0 e^{-\left(\frac{2.7r}{R}\right)^3}$

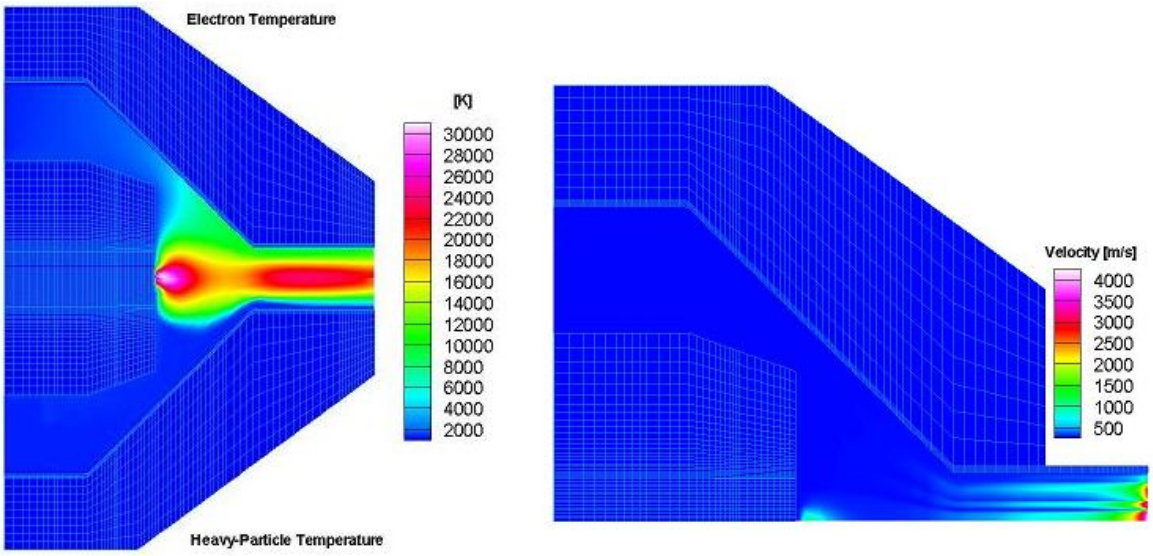

Figure C.9: Results with c = 2.7: (*left*) temperature distribution and (*right*) velocity distribution

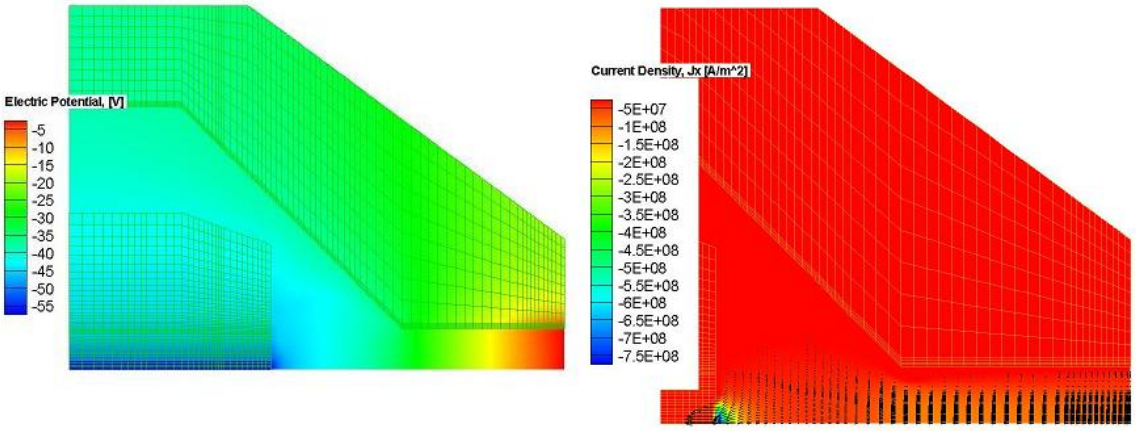

Figure C.10: Results with c = 2.7: (*left*) electric potential distribution and (*right*) current density distribution

6) $c = 2.8 \rightarrow J = J_0 e^{-\left(\frac{2.8r}{R}\right)^3}$

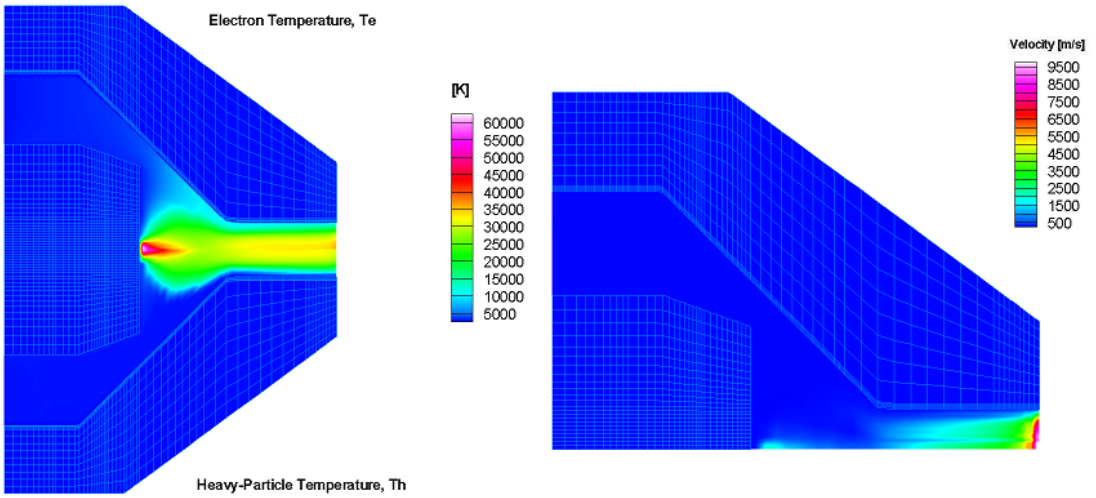

Figure C.11: Results with c = 2.8: (*left*) temperature distribution and (*right*) velocity distribution

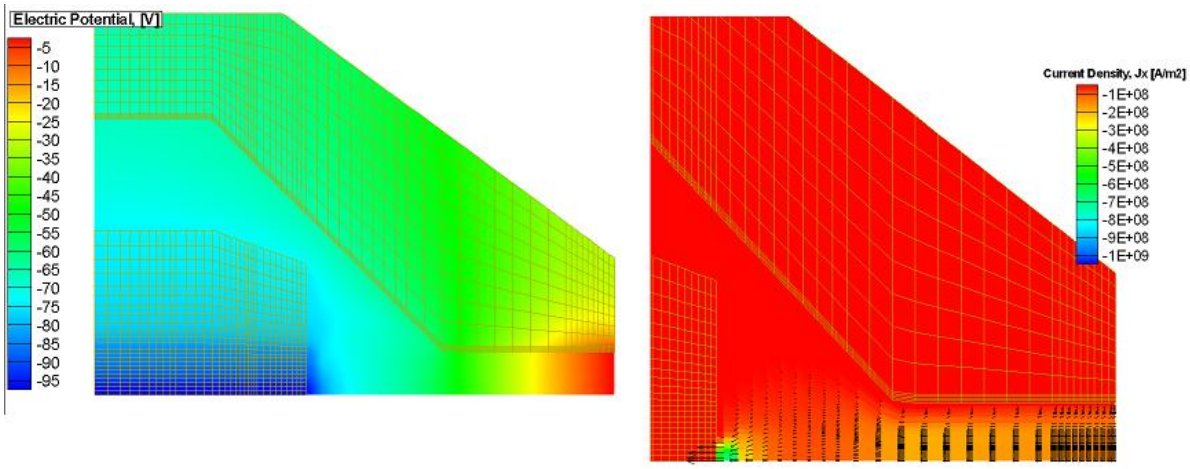

Figure C.12: Results with $c = 2.8$: (*left*) electric potential distribution and (*right*) current density distribution